COPPER-BASED DIAMOND-LIKE TERNARY SEMICONDUCTORS FOR THERMOELECTRIC APPLICATIONS

By

Eric John Skoug

A DISSERTATION

Submitted to
Michigan State University
in partial fulfillment of the requirements
for the degree of

DOCTOR OF PHILOSOPHY

Materials Science and Engineering

2011

ABSTRACT

COPPER-BASED DIAMOND-LIKE TERNARY SEMICONDUCTORS FOR THERMOELECTRIC APPLICATIONS

By

Eric John Skoug

Heightened global concern over greenhouse gas emissions has led to an increased demand for clean energy conversion technologies. Thermoelectric materials convert directly between thermal and electrical energy and can increase the efficiency of existing processes via waste heat recovery and solid-state climate control applications. The conversion efficiency of available thermoelectric materials and the devices comprised of them is unfortunately quite low, and thus new materials must be developed in order for thermoelectrics to keep pace with competing technologies. One approach to increasing the conversion efficiency of a given material is to decrease its lattice thermal conductivity, which has traditionally been accomplished by introducing phonon scattering centers into the material. These scattering centers also tend to degrade electronic transport in the material, thereby minimizing the overall effect on the thermoelectric performance. The purpose of this work is to develop materials with inherently low lattice thermal conductivity such that no extrinsic modifications are required. A novel approach in which complex ternary semiconductors are derived from well-known binary or elemental semiconductors is employed to identify candidate materials. Ternary diamond-like compounds, namely Cu_2SnSe_3 and Cu_3SbSe_4, are synthesized, characterized, and optimized for thermoelectric applications. It is found that sample-to-sample variations in hole concentration limits the plausibility of Cu_2SnSe_3 as a thermoelectric material. Cu_3SbSe_4 is found to be a promising material that can achieve thermoelectric performance comparable to state-of-the-art materials when optimized. This work uncovers anomalous thermal conductivity in several Cu-Sb-Se ternary compounds, which is used to develop a set of guidelines relating crystal structure to inherently low lattice thermal conductivity.

DEDICATION

To my loving wife Shannon, who believes in me when I need it most.
To Dad, my hero and role model who taught me that I can achieve anything I set my mind to.
To Connie, Jennica, Evan, and Kryn, who encourage and support me in all that I do.
To Mom, who is with me in memory every day.

ACKNOWLEDGEMENTS

I am extremely grateful to those who have contributed their time and effort to this project. I would like to thank my advisor and mentor Dr. Donald Morelli for giving me the opportunity to conduct this research, and my committee members Drs. Jeff Sakamoto, Tim Hogan, and K. Subramanian for their guidance. I am indebted to my coworkers and lab-mates Jeff Cain, Kevin Zhou, Chang Liu, Ponns, Hui Sun, Xu Lu, Hao Yang, Steve Boona, and Gloria Lehr for their hard work and helpful discussions throughout the course of my graduate study. I would also like to thank my collaborators Paul Majsztrik, Melanie Kirkham, Edgar Lara-Curzio, Chris Wolverton, Yongsheng Zhang, Bhanu Mahanti, and Dat Do for their valuable contributions.

Finally I would like to acknowledge the funding sources for this project. This work was supported by the National Science Foundation under Award No. NSF-CBET-0754029. In addition, sample synthesis efforts were partially supported as part of the Center for Revolutionary Materials for Solid State Energy Conversion, an Energy Frontier Research Center funded by the U.S. Department of Energy, Office of Science, Office of Basic Energy Sciences under Award Number DE-SC0001054. Research through the Oak Ridge National Laboratory's High Temperature Materials Laboratory User Program was sponsored by the U. S. Department of Energy, Office of Energy Efficiency and Renewable Energy, Vehicle Technologies Program.

TABLE OF CONTENTS

List of Tables viii

List of Figures ix

1 Introduction to Thermoelectrics 1
- 1.1 Thermoelectric Effects . . . 1
- 1.2 Applications For Thermoelectric Devices . . . 3
- 1.3 Thermoelectric Conversion Efficiency . . . 4

2 Approaches to Increasing the Thermoelectric Figure of Merit 8
- 2.1 Substitutional Solid Solutions . . . 8
- 2.2 Atomic Rattlers . . . 9
- 2.3 Low-Dimensional Materials . . . 10
- 2.4 Ternary Compounds Based on PbTe . . . 12
- 2.5 Motivation For The Present Work . . . 13

3 Synthesis and Characterization Methods 15
- 3.1 Materials Synthesis . . . 15
- 3.2 Crystal Structure, Phase Purity, and Microstructural Analysis . . . 16
- 3.3 Transport Property Measurements . . . 16

4 Rocksalt-Like Cu-Based Ternary Compounds 21
- 4.1 Background and Motivation . . . 21
- 4.2 Experimental . . . 22
- 4.3 Results and Discussion . . . 22
  - 4.3.1 $CuBiSe_2$ . . . 22
  - 4.3.2 Cu_3BiSe_3 . . . 26
  - 4.3.3 Other Cu-Bi-Se Ternary Compounds . . . 32
- 4.4 Summary . . . 34

5 Diamond-Like Cu-Based Ternary Compounds 36
- 5.1 Background and Motivation . . . 36
  - 5.1.1 Why Study Diamond-Like Cu-Based Ternary Compounds? . . . 36
  - 5.1.2 Third-Order Ternary Derivatives of II-VI: I_2-IV-VI_3 Compounds . . . 38
  - 5.1.3 Fourth-Order Ternary Derivatives of II-VI: I_3-V-VI_4 Compounds . . . 39
  - 5.1.4 Outline for the Present Work . . . 40
- 5.2 Cu_2SnSe_3 . . . 41
  - 5.2.1 Experimental . . . 41
  - 5.2.2 Results and Discussion . . . 41
  - 5.2.3 Summary . . . 48

5.3 The Cu_2SnSe_3-Cu_2GeSe_3 Solid Solution . . . 49
5.3.1 Experimental . . . 49
5.3.2 Results and Discussion . . . 49
5.3.3 Summary . . . 59
5.4 The Cu_2SnSe_3-Cu_2SnS_3 Solid Solution . . . 60
5.4.1 Experimental . . . 60
5.4.2 Results and Discussion . . . 60
5.4.3 Summary . . . 63
5.5 Off-Stoichiometric Cu_2GeSe_3 Compounds . . . 65
5.5.1 Experimental . . . 65
5.5.2 Results and Discussion . . . 65
5.5.3 Summary . . . 77
5.6 Cu_3SbSe_4 . . . 79
5.6.1 Experimental . . . 79
5.6.2 Results and Discussion . . . 80
5.6.3 Summary . . . 88
5.7 The Cu_3SbSe_4-Cu_3SbS_4 Solid Soluiton . . . 90
5.7.1 Experimental . . . 90
5.7.2 Results and Discussion . . . 91
5.7.3 Summary . . . 104
5.8 Cu-Based Diamond-Like Ternary Compounds: Conclusions and Future Work . . . 107

6 The Effect of Lone Electron Pairs on the Lattice Thermal Conductivity of Group VA Chalcogenides 111
6.1 Background and Motivation . . . 111
6.2 Experimental . . . 114
6.3 Results and Discussion . . . 115
6.3.1 Phase Purity of $CuSbSe_2$ and Cu_3SbSe_3 . . . 115
6.4 The Lattice Thermal Conductivity of $CuSbSe_2$, Cu_3SbSe_3, and Cu_3SbSe_4 . . . 119
6.5 The Effect of Lone-Pair Electrons on the Coordination Environment of Sb . . . 119
6.6 Generalization to Group VA Chalcogenides . . . 122
6.7 Summary . . . 126

7 Conclusions and Future Work 128

References 133

LIST OF TABLES

Table 4.1 Average compositions (determined by EDS) of the light and dark phase regions in the slow cooled Cu_3BiSe_3 sample shown above. 28

Table 4.2 Average compositions (determined by EDS) of the light and dark phase regions in the quenched Cu_3BiSe_3 sample shown above. 29

Table 4.3 Measured and reported room temperature thermoelectric properties of Cu_3BiSe_3 29

Table 5.1 Reported thermal conductivities and band gaps for a series of diamond-like semiconductors with increasing number of atoms per unit cell. 38

Table 5.2 EDS compositions of the majority phase for selected $Cu_2Ge_{1+x}Se_3$ compounds. 74

Table 5.3 Refined lattice constants for the $Cu_3SbSe_{4-x}S_x$ compounds, estimated standard deviation of the last digit is given in parentheses. 91

Table 5.4 Phonon-impurity scattering parameters along with calculated (κ_{calc}) and measured (κ_{exp}) thermal conductivities (in W/m*K) for the $Cu_3SbSe_{4-x}S_x$ compounds. 98

Table 5.5 Room temperature properties of the $Cu_3Sb_{1-y}Ge_ySe_{4-x}S_x$ compounds. . . . 101

Table 6.1 Relative amounts of phases present in Cu_3SbSe_3 samples quenched from 500°C and 900°C in room temperature water. 116

Table 6.2 Properties of group VA chalcogenides taken from the literature (continues on next page) 127

LIST OF FIGURES

Figure 1.1 Schematic representation of a simple thermocouple composed of metals m_1 and m_2. 1

Figure 1.2 Schematic representation of a thermoelectric unicouple demonstrating the Seebeck effect (left) and the Peltier effect (right). For interpretation of the references to color in this and all other figures, the reader is referred to the electronic version of this dissertation. 3

Figure 1.3 Conversion efficiency versus hot side temperature for thermoelectric power generation for several different values of ZT (reproduced from [6]). 6

Figure 2.1 Compositional dependence of the thermal resistivity of GaAs-AlAs alloys. Reproduced from [13]. 9

Figure 3.1 Sample preparation for direct fusion synthesis. From left to right: stoichiometric quantities of the pure elements, pure elements in quartz ampoule, evacuating quartz ampoule, sealing quartz ampoule, sealed quartz ampoule ready to be placed in furnace. 15

Figure 3.2 Schematic representation of experimental setup used for low temperature measurements of Seebeck coefficient, electrical resistivity, and thermal conductivity. 18

Figure 3.3 Schematic representation of experimental setup used for low temperature Hall measurements, pictured normal to the sample thickness. 20

Figure 4.1 Schematic representation of an as-synthesized $CuBiSe_2$ sample after slow-cooling and annealing at 400°C (left), XRD pattern of the top portion and powder diffraction file (PDF) for Cu_2Se (upper right), and XRD pattern of the lower portion and PDF for $Cu_{1.78}Bi_{4.73}Se_8$. 23

Figure 4.2 XRD pattern of a quenched $CuBiSe_2$ sample and PDF for $Cu_{1.78}Bi_{4.73}Se_8$. 25

Figure 4.3 XRD patterns from Cu_3BiSe_3 samples that were (a) slow cooled from 750°C to 400°C and annealed for 4 days and (b) quenched in water from 750°C, along with the reported pattern for rocksalt Cu_3BiSe_3 [47]. 27

Figure 4.4 EDS X-ray mapping of a slow cooled Cu_3BiSe_3 sample. Upper left BSE image shows the mapped region, remaining images show the distribution of Cu, Bi, and Se as indicated. 28

Figure 4.5 BSE image of a quenched Cu_3BiSe_3 sample, showing phase separation at the grain boundaries. Dashed line indicates region selected for X-ray mapping, shown in Figure 4.6 below. 30

Figure 4.6 EDS X-ray mapping of a quenched Cu_3BiSe_3 sample. Upper left BSE image shows the mapped region, remaining images show the distribution of Cu, Bi, and Se as indicated. 31

Figure 4.7 XRD patterns of $CuBi_3Se_5$ compounds prepared with different starting compositions as indicated. Lower plot shows the powder diffraction file (PDF) for $Cu_{1.78}Bi_{4.73}Se_8$, reported by Makovicky *et al* [52]. 33

Figure 4.8 Low temperature thermoelectric properties of $CuBi_3Se_5$ compounds. Compositions of the samples are: #1 - $Cu_{1.6}Bi_{4.8}Se_8$, #2 - $Cu_{1.7}Bi_{4.7}Se_8$, #3 - $Cu_{1.78}Bi_{4.73}Se_8$. 34

Figure 5.1 X-ray diffraction pattern for Cu_2SnSe_3 quenched in water from 900°C. All peaks correspond to the cubic phase, shown at right, where the larger spheres represent the random arrangement of Cu and Sn atoms on the cation sublattice. 42

Figure 5.2 X-ray diffraction pattern for Cu_2SnSe_3 slow cooled and annealed at 400°C. Inset shows low angle peaks corresponding to the monoclinic structure, shown at right. 43

Figure 5.3 Temperature dependence of the hole concentration of $Cu_2Sn_{1-x}Ga_xSe_3$ and $Cu_2Sn_{1-y}In_ySe_3$ compounds. 45

Figure 5.4 Low temperature thermoelectric properties of the $Cu_2Sn_{1-x}Ga_xSe_3$ compounds. 46

Figure 5.5 High temperature electronic properties of $Cu_2Sn_{0.975}Ga_{0.025}Se_3$. 47

Figure 5.6 X-ray diffraction patterns of quenched $Cu_2Sn_{1-x}Ge_xSe_3$ compounds, $0 \leq x \leq 1.0$. 50

Figure 5.7 X-ray diffraction patterns of slow cooled $Cu_2Sn_{1-x}Ge_xSe_3$ compounds, x $\leq$ 0.5. Lower plot shows close-up view of low angle peaks indicating monoclinic structure, vertical lines represent reported peak locations for monoclinic Cu_2SnSe_3 [65]. 51

Figure 5.8 X-ray diffraction patterns of slow cooled $Cu_2Sn_{1-x}Ge_xSe_3$ compounds, x $>$ 0.5. 52

Figure 5.9 Lattice spacing of the $Cu_2Sn_{1-x}Ge_xSe_3$ compounds with Cu_2SnSe_3-type structure: (a) lattice parameter of the cubic (quenched) samples, (b) interplanar spacing of the (200) planes of the monoclinic (slow cooled) samples. 53

Figure 5.10 Temperature dependence of the Seebeck coefficient and electrical resistivity of the $Cu_2Sn_{1-x}Ge_xSe_3$ compounds for x $<$ 0.5 54

Figure 5.11 Temperature dependence of the thermal conductivity of the $Cu_2Sn_{1-x}Ge_xSe_3$ compounds for x = 0 and 0.5. Dotted lines represent lattice thermal conductivity calculated from the Debye model (equation 5.2). 58

Figure 5.12 X-ray diffraction patterns of the $Cu_2SnSe_{3-x}S_x$ compounds. 61

Figure 5.13 Lattice thermal conductivity of the $Cu_2SnSe_{3-x}S_x$ compounds. 62

Figure 5.14 High temperature thermoelectric properties of $Cu_2Sn_{0.925}In_{0.075}Se_{2.1}S_{0.9}$ 63

Figure 5.15 XRD patterns for slow cooled $Cu_2Ge_{1+x}Se_3$ compounds with negative values of x. 66

Figure 5.16 Temperature dependence of the electrical resistivity, Seebeck coefficient, and thermal conductivity for slow cooled $Cu_2Ge_{1+x}Se_3$ compounds with negative values of x. 67

Figure 5.17 XRD patterns for the $Cu_2Ge_{1+x}Se_3$ compounds with $0 \leq x \leq 0.55$. 68

Figure 5.18 Temperature dependence of the thermoelectric properties of the $Cu_2Ge_{1+x}Se_3$ compounds with $0 \leq x \leq 0.55$. 69

Figure 5.19 XRD patterns for the $Cu_2Ge_{1+x}Se_3$ compounds with $0.55 \leq x \leq 1.0$, "SC" and "Q" labels indicate slow cooled and quenched samples respectively. . . 70

Figure 5.20 Temperature dependence of the thermoelectric properties of the $Cu_2Ge_{1+x}Se_3$ compounds with $0.55 \leq x \leq 1.0$, "SC" and "Q" labels indicate slow cooled and quenched samples respectively. 71

Figure 5.21 Measured thermal conductivity at 80K (a) and calculated lattice constant (b) versus Ge content for the $(Cu_2Ge_{1.55}Se_3)_{1-y}Ge_y$ solid solution. The dashed line in (b) represents the linear relation predicted by Vegard's law. The data for pure Ge are taken from [45] and [94]. 72

Figure 5.22 EDS X-ray mapping of a typical region of a $Cu_2Ge_{1+x}Se_3$ sample. Upper left BSE image shows the mapped region, remaining images show the distribution of Cu, Ge, and Se as indicated 73

Figure 5.23 EDS composition (at% Ge) versus starting Ge content (x) for $Cu_2Ge_{1+x}Se_3$ compounds. Error bars indicate $\pm 10\%$ error associated with EDS measurement. 75

Figure 5.24 EDS X-ray mapping of a typical region of a $Cu_2Ge_{2.2}Se_3$ sample. Upper left BSE image shows the mapped region, remaining images show the distribution of Cu, Ge, and Se as indicated 76

Figure 5.25 XRD pattern of a Cu_3SbSe_4 sample slow cooled from 900°C to room temperature, along with the PDF data for Sb_2Se_3 and Cu_3SbSe_4. 81

Figure 5.26 XRD pattern of a Cu_3SbSe_4 sample quenched from 500°C to room temperature, along with the PDF data for Cu_3SbSe_4. 82

Figure 5.27 EDS X-ray mapping of a typical region of Cu_3SbSe_4 (work completed at ORNL). Upper left image shows a backscattered electron image of a 600μm x 600μm region, and the distributions of Cu, Sb, and Se in the same region are shown as indicated (white pixel indicates presence of element). 83

Figure 5.28 Temperature dependence of the hole concentration and mobility for Cu_3SbSe_4, with and without the post-quench 300°C/48 hrs annealing step. Dashed line indicates the $T^{-3/2}$ temperature dependence characteristic of carrier scattering by acoustic phonons. 84

Figure 5.29 Temperature dependence of the hole concentration and mobility of $Cu_3Sb_{1-x}A_xSe_4$ compounds (A = Ge or Sn). 85

Figure 5.30 Temperature dependence of the electronic properties of the $Cu_3Sb_{1-x}A_xSe_4$ compounds (A = Ge, Sn). 86

Figure 5.31 Temperature dependence of the thermal conductivity and dimensionless thermoelectric figure of merit of the $Cu_3Sb_{1-x}A_xSe_4$ compounds (A = Ge, Sn). 87

Figure 5.32 XRD patterns of $Cu_3SbSe_{4-x}S_x$ samples. 92

Figure 5.33 Refined lattice constants of the $Cu_3SbSe_{4-x}S_x$ samples (from Figure 5.32) versus fractional occupation S (equal to x/4). Dashed lines indicate linear relationship predicted by Vegard's law. 93

Figure 5.34 Hole concentration and mobility of the $Cu_3SbSe_{4-x}S_x$ compounds. 94

Figure 5.35 Temperature dependence of the thermal conductivity of selected $Cu_3SbSe_{4-x}S_x$ compounds. Dashed lines are the calculated lattice thermal conductivities obtained from the Debye model. Error bars indicate $\pm$5% experimental error. 95

Figure 5.36 Compositional dependence of the lattice thermal conductivity (κ_L) of the $Cu_3SbSe_{4-x}S_x$ compounds at 80K and 300K. Dashed lines are the calculated lattice thermal conductivities obtained from the Debye model. Error bars indicate $\pm$5% experimental error. 97

Figure 5.37 Ratio of the weighted mobility (U) to lattice thermal conductivity (κ_L) versus composition in the $Cu_3SbSe_{4-x}S_x$ system for x$\leq$2. 100

Figure 5.38 Temperature dependence of the Seebeck coefficient and Electrical resistivity of the $Cu_3Sb_{1-y}Ge_ySe_{4-x}S_x$ compounds 102

Figure 5.39 Temperature dependence of the thermal conductivity and dimensionless thermoelectric figure of merit of the $Cu_3SbSe_{4-x}S_x$ compounds 103

Figure 5.40 High temperature lattice thermal conductivity of the $Cu_3SbSe_{4-x}S_x$ compounds. Dashed line indicates κ_L calculated from the Debye model for x=1.2 using γ=1.3. 105

Figure 6.1 Temperature dependence of the thermal conductivity of Cu_3SbSe_3 (open symbols) and Cu_3SbSe_4 (closed symbols). The electronic contribution is negligible for all samples. 115

Figure 6.2 Backscattered electron images of Cu_3SbSe_3 quenched from (a) 900°C and (b) 500°C into room temperature water with three phases labeled: A = $Cu_{2-x}Se$, B = Cu_3SbSe_3, C = $CuSbSe_2$. 116

Figure 6.3 X-ray mapping on a similar region of the sample shown in Figure 6.2(b). . . 117

Figure 6.4 X-ray diffraction pattern of a Cu_3SbSe_3 sample quenched from 900°C into icewater and annealed at 400°C for 5 days. 118

Figure 6.5 Temperature dependence of the lattice thermal conductivity of $CuSbSe_2$, Cu_3SbSe_3, and Cu_3SbSe_4. 120

Figure 6.6 Local coordination environment of Sb in $CuSbSe_2$, Cu_3SbSe_3 and Cu_3SbSe_4. Shaded lines represent bonds, dotted ovals represent the approximate morphology of the LEP orbital. 121

Figure 6.7 Lattice thermal conductivity versus average X-M-X bond angle of the group VA chalcogenides. 124

Figure 6.8 Lattice thermal conductivity versus average X-M-X bond angle of the group VA chalcogenides, separated according to the coordination number (CN) of the group V atom. 125

1 Introduction to Thermoelectrics

1.1 Thermoelectric Effects

The field of thermoelectricity has garnered considerable attention over the past two decades due to growing concern about carbon-based fuel consumption and greenhouse gas emissions. The principal thermoelectric effects, however, have been known for almost two centuries. In 1821 Thomas Seebeck discovered that heating a junction between two dissimilar metals produced a potential difference, and in 1834 Jean-Charles Peltier noted that heat was either absorbed or liberated at said junction when an electrical current was passed in different directions. These phenomena, known respectively as the Seebeck and Peltier effects, can be explained qualitatively using a simple thermocouple composed of metals m_1 and m_2 shown in Figure 1.1 [1].

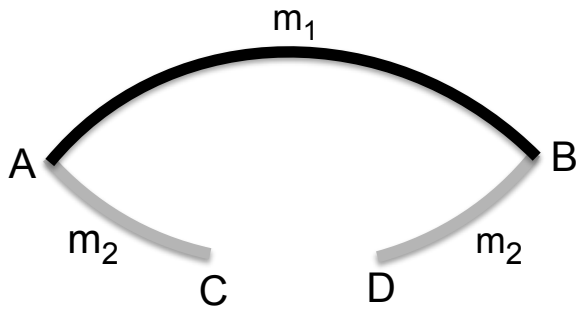

Figure 1.1: Schematic representation of a simple thermocouple composed of metals m_1 and m_2.

If junction A is maintained at a different temperature than junction B, a voltage will develop between points C and D. This effect is quantified by expressing the voltage drop per unit temperature change:

$$S = \frac{\Delta V}{\Delta T} \tag{1.1}$$

where S is referred to as the Seebeck coefficient. If the circuit is closed at points C and D and an

electrical current flows through the loop, heat will be either absorbed or liberated at junctions A and B depending on the direction of the current. The ratio of the exchanged heat (Q) to the current in the loop (I) is defined as:

$$\Pi = \frac{Q}{I} \tag{1.2}$$

where Π is the Peltier coefficient. The Seebeck and Peltier coefficients demonstrate the same basic physical process and are related through the simple expression:

$$S = \frac{\Pi}{T}. \tag{1.3}$$

This macroscopic view of the thermoelectric effects is instructive, but it does not provide insight into the fundamental mechanisms behind the effects. For this purpose it is useful to consider a thermoelectric unicouple composed of one n-type (charge carried by electrons) and one p-type (charge carried by holes) material, shown in Figure 1.2(a). If one side of the couple is exposed to a heat source as shown, the charge carriers in the materials become energized at the hot side and diffuse toward the cold side. This causes a thermally induced voltage to develop across the couple via the Seebeck effect, and an electrical current I will flow in the direction indicated when a resistive load is connected to the couple. Conversely, an applied clockwise current I will induce the flow of electrons and holes and generate a temperature difference across the couple via the Peltier effect, as shown in Figure 1.2(b). In this configuration, the thermoelectric couple acts as a solid-state heat pump. Connecting many thermoelectric couples electrically in series and thermally in parallel forms a thermoelectric module, which can then be used in one of many applications for thermoelectric devices.

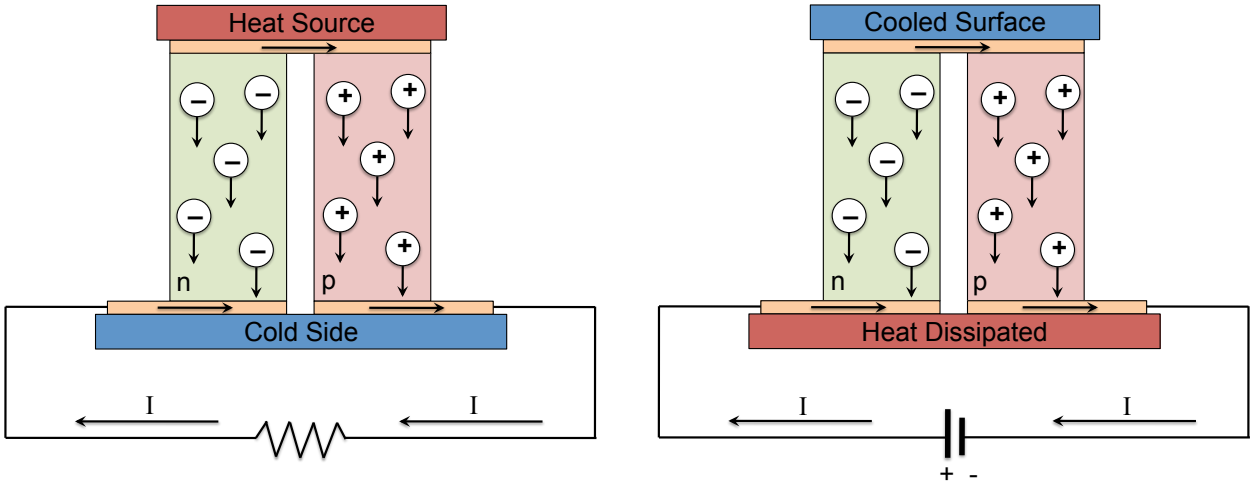

Figure 1.2: Schematic representation of a thermoelectric unicouple demonstrating the Seebeck effect (left) and the Peltier effect (right). For interpretation of the references to color in this and all other figures, the reader is referred to the electronic version of this dissertation.

1.2 Applications For Thermoelectric Devices

The Seebeck and Peltier effects suggest two distinct applications for thermoelectric devices: power generation and climate control. The earliest and perhaps most successful application has been the long-term use of radioisotope thermoelectric generators (RTGs) in NASA's deep space probes. RTGs utilize the heat produced by a decaying radioactive material (such as Plutonium-238) to generate electrical power by way of many thermoelectric modules. These generators demonstrate the stability and longevity of thermoelectric devices; several deep space probes still in operation by NASA today (most notably the Voyager probes) were launched over 30 years ago. RTGs are seldom used for remote power generation in terrestrial applications, mainly due to fears over radioactive contamination should the generator become damaged.

At present, thermoelectric climate control has been utilized only in small-scale applications. The completely solid-state, motion free cooling provided by a thermoelectric module allows for temperature regulation of electronic components that are sensitive to vibration. The module's small footprint has lead to small-scale refrigeration applications, such as portable picnic coolers that are

powered by the auxiliary port in a car. Most recently, thermoelectric devices are being used to provide localized heating and cooling in automotive seats and cup holders, primarily in high-end luxury models.

The driving force behind the renewed interest in thermoelectric research is not the specialized applications mentioned above. Thermoelectrics have the potential to impact the world's energy crisis, namely by improving the efficiency of existing processes. In the United States alone, over half of the energy produced every year is not utilized, but rather lost due to inefficient energy production [3]. In an automobile, for example, only 20-30% of the energy generated by the engine is used for vehicle operation while the majority of the energy is lost as heat. In this instance, a thermoelectric generator in contact with the exhaust stream or radiator could transform a portion of the wasted heat into useable electricity. Calculations have shown that a suitable thermoelectric generator used in this way could improve fuel economy by up to 4%, a substantial gain [4]. In addition, current automotive air conditioning systems are required to cool the entire cabin quite rapidly in order to achieve customer comfort, and therefore typically have enough cooling capacity to cool a small household. Thermoelectric modules strategically placed in the vehicle would provide targeted cooling rather than full cabin cooling, while simultaneously requiring less power to operate and eliminating the use of harmful refrigerants. Large-scale thermoelectric applications are not limited to the automotive sector; other proposed applications include solar thermoelectric generators (STEGs) which have recently been demonstrated as a promising new route towards solar power generation [5]. The use of thermoelectric technology on a large scale has been frustrated mainly by the low conversion efficiencies of currently available thermoelectric materials.

1.3 Thermoelectric Conversion Efficiency

The conversion efficiency η of a thermoelectric device is limited to a fraction of its Carnot efficiency ($\Delta T / T_h$):

$$\eta = \frac{\Delta T}{T_h} \cdot \frac{\sqrt{1+Z\bar{T}}-1}{\sqrt{1+Z\bar{T}+T_c/T_h}} \tag{1.4}$$

where Z is a material dependent parameter and $\bar{T}$, T_h, and T_c are the average operating temperature, hot side temperature, and cold side temperature, respectively. From equation 1.4 it is clear that the parameter Z, termed the thermoelectric figure of merit, is the foremost quantity for improving η. This quantity is commonly multiplied by the operating temperature T and expressed as the dimensionless thermoelectric figure of merit ZT, given by:

$$ZT = \frac{S^2\sigma}{\kappa} \cdot T \tag{1.5}$$

where S is the Seebeck coefficient, σ is the electrical conductivity, and κ is the thermal conductivity of the material. For most applications, a conversion efficiency of more than 20% is required in order for a thermoelectric device to be competitive with conventional technologies. Figure 1.3 shows that very large values of ZT are required for thermoelectrics to achieve greater than 20% conversion efficiency. At present, the best thermoelectric materials have ZT on the order of 1 - 1.5, but with continually increasing activity in thermoelectric materials research, materials with ZT = 2.0 are not out of the question. A material that has $ZT \geq 2$ in addition to low raw material and production costs would justify the large-scale use of thermoelectric power generation and cooling.

The problem with achieving very high values of ZT is that Z is comprised of contraindicated physical parameters. That is, the constituents of Z cannot be independently varied; changing one parameter will always affect another. For instance, the total thermal conductivity (κ_T) of any material is composed of contributions from the crystal lattice (κ_L) as well as the charge carriers (κ_e):

$$\kappa_T = \kappa_e + \kappa_L. \tag{1.6}$$

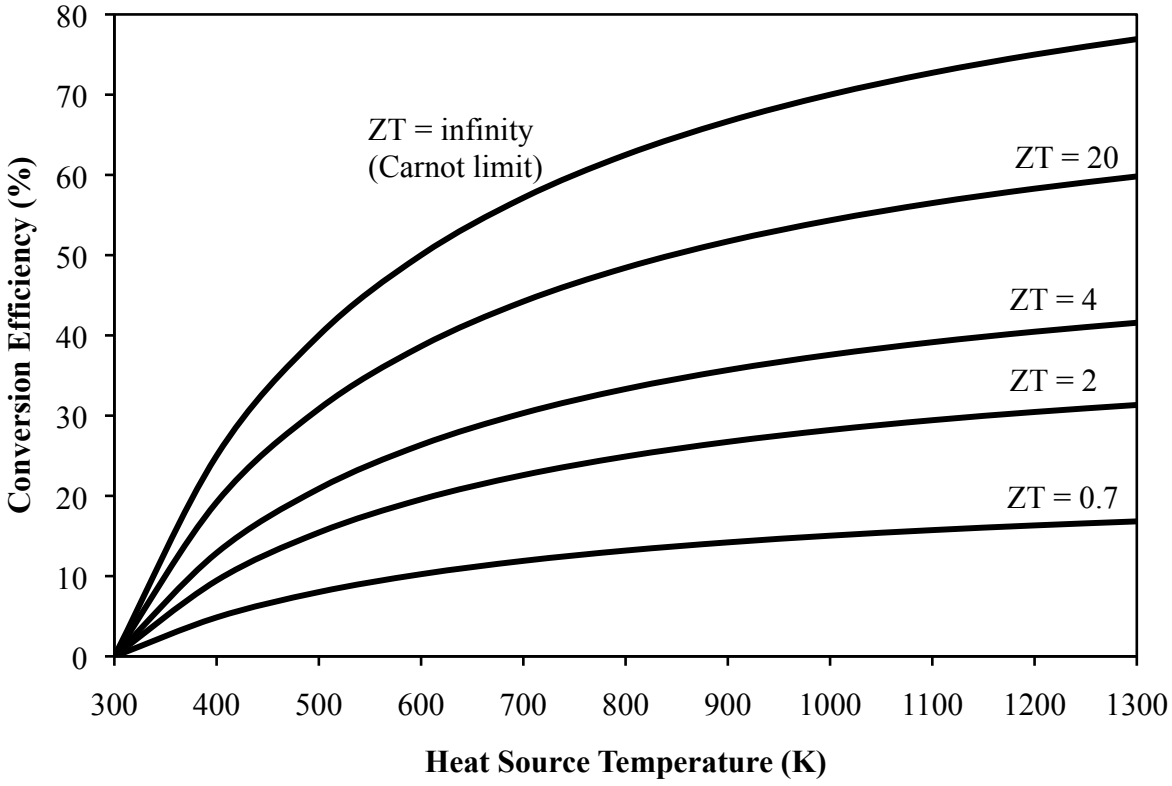

Figure 1.3: Conversion efficiency versus hot side temperature for thermoelectric power generation for several different values of ZT (reproduced from [6]).

If the electrical conductivity of the material is increased, the electronic component of the thermal conductivity will increase proportionally as defined by the Wiedemann-Franz law:

$$\kappa_e = L_0 \sigma T \tag{1.7}$$

where L_0 is the Lorenz number, normally taken to be $2.44 \times 10^{-8} W \Omega K^{-2}$. The lattice component can be reduced by introducing impurities or defects into the crystal lattice, but these will also scatter electronic charge carriers and negatively affect electronic transport in the material. Furthermore, there is a lower limit to the lattice thermal conductivity determined by the interatomic spacing.

If one choses to focus solely on the numerator of Z ($S^2\sigma$, termed the thermoelectric power fac-

tor), equally problematic contradictions are encountered. Assuming a single parabolic band model with one type of strongly degenerate carrier present, the Seebeck coefficient can be expressed as [7]:

$$S = \frac{8\pi^2 k_B^2}{3eh^2} m^* T \left(\frac{\pi}{3n}\right)^{2/3} \tag{1.8}$$

where k_B is Boltzmann's constant, e is the electronic charge, h is Planck's constant, m^* is the carrier effective mass, and n is the carrier concentration. Equation 1.8 is called the Pisarenko relation and illustrates the dependence of the Seebeck coefficient on carrier concentration. The n dependence of the electrical conductivity is given by:

$$\sigma = ne\mu \tag{1.9}$$

where μ is the carrier mobility. It is evident from equations 1.8 and 1.9 that increasing the carrier concentration of a material (doping) will cause S to decrease and σ to increase, thus minimizing the overall effect on Z. In addition, a large carrier effective mass will produce a large Seebeck coefficient but will degrade the carrier mobility according to $\mu = e\tau/m^*$, where τ is the carrier scattering time.

Despite these challenges, numerous approaches to increasing the thermoelectric figure of merit have been developed. The following review covers some of the most successful approaches and is not meant to offer exhaustive coverage of all possible techniques. Most importantly, this review will highlight a new approach to identifying materials with potentially large thermoelectric figure of merit and provide motivation for the present work.

2 Approaches to Increasing the Thermoelectric Figure of Merit

2.1 Substitutional Solid Solutions

One of the earliest approaches to increasing the thermoelectric figure of merit was to introduce electrically neutral impurity atoms into the crystal lattice of a given material. This practice is still widely used today as it provides a fairly simple route to incremental enhancements in ZT. The main principle behind this approach is that impurity atoms with atomic mass and radius different than the host atoms will disrupt the periodicity in the crystal lattice and cause increased phonon scattering, thus reducing the lattice thermal conductivity. The increase in ZT arises due to the fact that the impurity atoms typically scatter phonons to a larger extent than charge carriers, causing a larger disruption in thermal rather than electrical transport.

The thermal conductivity of solid solutions was studied extensively by Ioffe, who first applied the approach to thermoelectric materials [8], [9]. He noted that the presence of impurity atoms always decreased the thermal conductivity more than the carrier mobility due to the shorter wavelength of phonons as compared to electrons. Typically, two compounds with similar crystal structures are chosen such that the composition can be varied continuously without inducing structural transformations or impurity phase formation. The thermal conductivity of the zincblende $Ga_{1-x}Al_xAs$ alloys, shown as thermal resistivity (κ^{-1}) in Figure 2.1, illustrates this concept. For a mixture of GaAs and AlAs crystals, one would expect the thermal resistivity to follow a linear relation, indicated by the dashed line, as defined a simple rule of mixtures. The disordered arrangement of Ga and Al atoms on the metal sublattice causes increased phonon scattering, leading to the large increase in thermal resistivity for the intermediate compositions. Many of the best thermoelectric materials to date come from solid solutions of two compounds, including the PbTe-PbSe, Si-Ge, and Bi_2Te_3-Bi_2Se_3 systems [10] - [12].

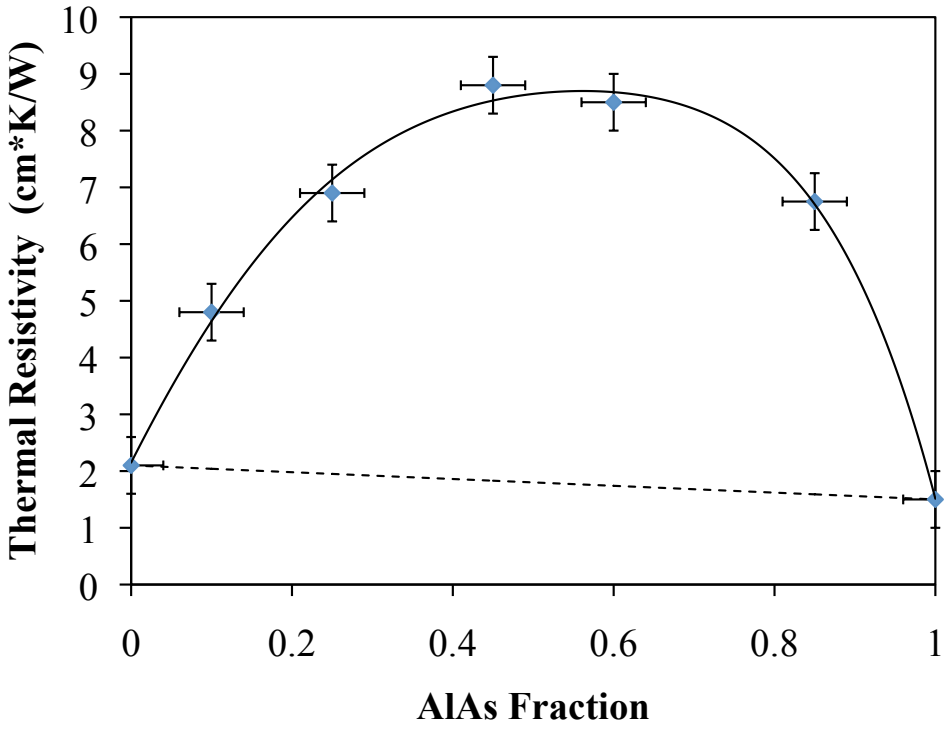

Figure 2.1: Compositional dependence of the thermal resistivity of GaAs-AlAs alloys. Reproduced from [13].

2.2 Atomic Rattlers

Materials with large voids in their crystal structures are ideal candidates for thermoelectric applications, particularly because of their ability to accommodate heavy "rattling" atoms. Here the lattice thermal conductivity is again reduced by the presence of impurity atoms, but in this case the impurity atoms reside in interstitial atomic sites rather than substituting for host atoms as in solid solutions. This approach was first proposed by Slack [14], who noted that void-filling atoms in the skutterudite crystal structure possessed large thermal vibration parameters [15] and postulated their ability to scatter phonons and reduce κ_L. This idea prompted a vast undertaking of research on the skutterudite material system, which has led to one of the most successful classes of thermoelectric materials to date.

Skutterudites, typified by the naturally occurring mineral $CoAs_3$, had been known for many years but were not seriously considered for thermoelectric applications until the mid-1990s when Morelli *et. al.* showed that their lattice thermal conductivity could be reduced by more than an order-of-magnitude by filling the atomic "cages" with rare earth atoms[16]. It was later shown that while the weakly-bound filling atoms effectively scatter phonons, the covalently-bound metal-antimony framework maintains the high carrier mobility of the binary skutterudite antimonides, leading to high ZT values at elevated temperatures [17]. Skutterudites can be doped both n and p-type and are currently some of the best available thermoelectric materials for power generation, with reported ZT values in excess of 1.7 [18].

Shortly after the discovery of filled-skutterudite thermoelectric materials, work began on another class of cage-structure compounds termed clathrates. These compounds are structurally similar to certain phases of ice where guest atoms reside in cages formed by the water molecules. Nolas *et. al.* first realized the potential of semiconducting Ge clathrates for thermoelectric applications, and reported very low thermal conductivity for compounds of the form Sr_8Ge_{46} [19]. The glass-like thermal conductivity in these compounds is attributed to strong phonon scattering from the "rattling" of the Sr^{2+} ion inside the Ge cage, much the same as the skutterudite compounds. ZT values as high as 1.35 have been reported for Ge clathrate compounds; current research is focused on clathrate compounds with Si or Sn as the group IV element to replace costly Ge [20], [21].

2.3 Low-Dimensional Materials

The effect of material dimensions on thermoelectric properties was first studied several decades ago after Goldsmid and Penn noted that phonon scattering at grain boundaries can become appreciable in solid solutions, where heat is carried primarily by low frequency phonons [22]. Early experimental studies focused on fine-grained Si-Ge alloys [23] and showed that ZT can be increased due to the reduction in κ_L. The problem is that both phonons and electrons are scattered at grain boundaries, so typically only small ZT improvements can be achieved. In addition, for

high temperature materials, grain growth will likely occur due to long-term exposure to high operating temperatures. Thus, recent work is focused primarily on fine-grained Bi_2Te_3 alloys for low temperature applications [24], [25].

The most significant justification for low-dimensional thermoelectric materials came in 1993 when Hicks and Dresselhaus showed that carrier confinement in quantum structures could lead to improved thermoelectric properties [26]. The basis of their theory relies on the fact that as the dimensionality of a system decreases, carrier confinement produces sharp features in the electronic density of states that can be exploited to effectively "decouple" S, σ and κ, resulting in extremely high ZT values. Positioning the Fermi level near one of these features leads to a high thermoelectric power factor since S is proportional to the energy dependence of the density of states and σ is proportional to the number of available states. The reduced dimensions and increased number of interfaces will alter the phonon characteristics of the material and cause low κ_L in addition to the high power factor.

This principle has been demonstrated on laboratory-scale quantum structures, most notably on PbTe quantum-dot superlattices that were reported to have ZT values exceeding 3 at elevated temperatures [28]. Although this result is quite amazing, these structures are complicated and expensive to produce and are not practical for large-scale applications. Thus over the past several years a major effort has been devoted to producing bulk thermoelectric materials with similar properties. The most common method is to introduce nanoscale inclusions into a bulk thermoelectric material thereby forming a nanocomposite that takes advantage of both the carrier confinement and phonon scattering properties of low-dimensional materials [29]. Another approach is to search for bulk materials that inherently have sharp features in their density of states. This has been demonstrated in the intermetallic compounds CoSi and Fe_2VAl, both of which have high thermoelectric power factors, although they are plagued by high thermal conductivity and thus low ZT values [30], [31].

2.4 Ternary Compounds Based on PbTe

To this point, the discussion on improving the thermoelectric figure of merit has focused on means of modifying well known materials. The approaches mentioned above aim to decouple the thermal and electrical transport properties of a given material in order to increase ZT. Most frequently, this is accomplished by introducing phonon scattering centers into the material to reduce the lattice thermal conductivity. Unfortunately, phonon and electron scattering centers are often one in the same and only incremental improvements to ZT can be achieved. An alternative approach is to search for materials with low *intrinsic* thermal conductivity; that is, they require no modification in order to achieve lattice thermal conductivity in the range appropriate for thermoelectric applications. The ternary compounds $AbSbTe_2$ and $AgSbSe_2$ have demonstrated this quality and thus received considerable attention for thermoelectric applications.

Schematically, these compounds are derived from PbTe by way of atomic substitution on the cation sublattice. Consider two unit cells of PbTe (Pb_2Te_2), now simply replace the Pb^{2+} ions with Ag^{1+} and Sb^{3+} ions in equal proportions thereby forming the ternary compound $AgSbTe_2$. Since charge balance is maintained, $AgSbTe_2$ retains that rocksalt crystal structure of PbTe but with two distinct atomic species Ag and Sb on the Pb sublattice. This method of deriving ternary compounds was pioneered by Goodman and Douglas, who found that compounds of the form I-III-VI_2 maintained a diamond-like crystal structure very similar to their binary II-VI and III-V counterparts (This notation will be used in the text to refer to families of compounds; roman numerals indicate the group of the periodic table and subscripts indicate stoichiometry) [32]. Subsequently, a host of ternary [33], [34] and quaternary [35] compounds derived in this fashion were reported.

Early studies on $AgSbTe_2$ and $AgSbSe_2$ reported very low thermal conductivity [36], [37] and ZT approaching 1.3 at 720K for the telluride [38], but these early samples were likely multiphase [39]. Recent studies have reported single phase samples [40] with ZT values approaching 1.2 at 400K [41]. In addition, compounds in the $AgSbTe_2$-PbTe solid solution have shown $ZT = 2.2$ at 800K, the largest figure of merit for any bulk thermoelectric material [42], although it has since

been shown that these compounds are essentially nanocomposites rather than true solid solutions [43].

Essential to the success of the thermoelectric $AgSbX_2$ compounds is their low intrinsic thermal conductivity. The low and temperature independent lattice thermal conductivity of $AgSbTe_2$ (0.7 W/m*K at 300K) is characteristic of an amorphous material and has been the subject of several investigations [37], [44]. The low thermal conductivity of $AgSbTe_2$ arises due to intrinsic anharmonicity in the lattice caused by its crystal structure and interatomic bonding. $AgSbTe_2$ has twice as many atoms per unit cell (n) as its parent compound PbTe which, from the empirical relationship $\kappa_L \propto n^{-2/3}$ derived by Slack [45], accounts for the difference in thermal conductivity between these isostructural compounds. Octahedral coordination in the rocksalt structure contributes to the anharmonicity in the lattice since each atom has 6 nearest neighbors, leaving little room for thermal vibration. Finally, the Sb ion is nominally in the trivalent state which means that the Sb $5s^2$ electrons are not involved in bonding. These "lone-pair" electrons around adjacent Sb ions can then interact with neighboring atoms, causing increased anharmonicity as compared to $AgInTe_2$ where all of the valence electrons of In^{3+} form bonds with neighboring atoms.

2.5 Motivation For The Present Work

The recent triumphs of $AgSbTe_2$ and its related compounds warrant further exploration in this area. One major drawback of $AgSbTe_2$ is a high raw material cost; both Ag and Te are very costly and replacements are needed in order for cost effective production. In the present work, only compounds that contain Cu as the group I element and Se or S as the group VI element are explored. In the following chapters, a comprehensive study of three approaches to producing new Cu-based ternary semiconductors for thermoelectric applications is presented. Chapter 4 covers Cu-based rocksalt structure ternary compounds, essentially following the same approach used for $AgSbTe_2$. Very few Cu-based rocksalt compounds have been reported, and none have been investigated for thermoelectric applications.

In Chapter 5 this approach is expanded to diamond structure compounds, where there exists a host of Cu-based diamond-like ternary semiconductors that have remained essentially unexplored for thermoelectric applications. Another advantage of these compounds is that higher-order substitutions are possible, which means that diamond-like compounds with larger number of atoms per unit cell can be formulated. This represents a potential for the discovery of ternary semiconductors with very low lattice thermal conductivity.

Finally in Chapter 6 the influence of lone-pair electrons on lattice thermal conductivity is investigated. The wealth of Cu-based ternary compounds presents a unique opportunity to study this effect, for which there is essentially no definitive evidence. A direct correlation between lone-pair electrons and low lattice thermal conductivity could provide a new design criteria for high efficiency thermoelectric materials.

3 Synthesis and Characterization Methods

The synthesis and characterization methods employed in this work were similar for all materials studied. Characterization techniques are held constant for all materials systems in order to facilitate comparison, while small variations in the synthesis procedure will be described separately in subsequent chapters.

3.1 Materials Synthesis

All materials were synthesized using direct fusion in evacuated quartz ampoules. Stoichiometric quantities of the pure elements (typically >99.999%, Alfa Aesar Puratronic©) were placed in quartz ampoules (8mm inner diameter) and evacuated to $<10^{-5}$ Torr. A methane-oxygen torch was then used to seal the elements under vacuum, as shown in Figure 3.1.

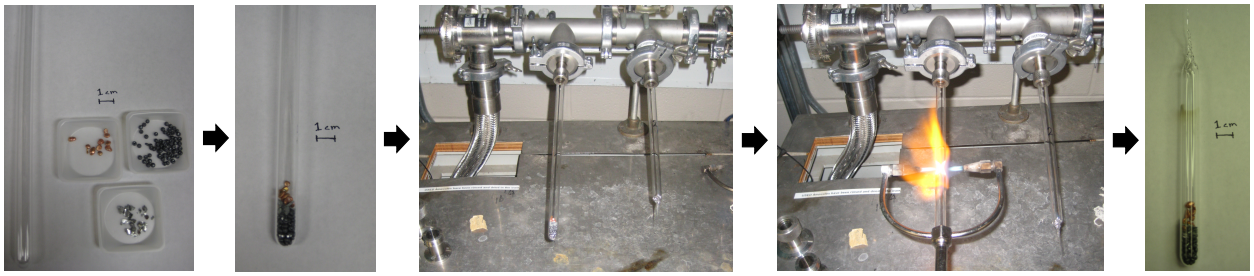

Figure 3.1: Sample preparation for direct fusion synthesis. From left to right: stoichiometric quantities of the pure elements, pure elements in quartz ampoule, evacuating quartz ampoule, sealing quartz ampoule, sealed quartz ampoule ready to be placed in furnace.

The sealed ampoules were then hung vertically in a digitally-controlled furnace and subjected to a precise temperature profile determined from phase diagrams (if available) or literature data. All of the materials studied here were heated slowly (0.4°C/min, to accommodate the high vapor pressure of Se and S) to 750 - 900°C, held for 12 hours, and cooled to room temperature. Cooling was achieved by either maintaining a constant cooling rate in the furnace or quenching the ampoule in water, the details of which will be discussed later. In some cases, powder processing was

used to produce high-quality samples for transport property measurements, as will be described in subsequent chapters.

3.2 Crystal Structure, Phase Purity, and Microstructural Analysis

The first step in characterizing the samples was to determine the phase purity and the crystal structures of the phases present. A portion of each sample was pulverized using a mortar and pestle and deposited onto a glass slide for X-ray diffraction (XRD) analysis. A Rigaku Miniflex II X-ray diffractometer (Cu K_α radiation, λ=0.154 nm) was used to evaluate the crystal structures of the majority phases. XRD patterns were analyzed using the Jade 9.0 sofware package, equipped with the JCPDS XRD pattern database. Differential scanning calorimetry (DSC 200 F3 Maia© from Netzsch) was employed to detect impurity phases below the detection limit of XRD, and also to measure the melting temperature and heat capacity of the samples.

Scanning electron microscopy (SEM) was used to investigate samples with complicated microstructures that could not be reliably evaluated by XRD or DSC. For certain samples, microscopy was performed at Oak Ridge National Laboratory using a Hitachi S3400 environmental SEM equipped with backscattered electron (BSE) and secondary electron (SE) detectors, as well as energy dispersive x-ray spectroscopy (EDS) instrumentation and software for elemental analysis. The majority of the SEM analysis was completed at the Michigan State University Center for Advanced Microscopy (MSU CAM) using a JEOL 6400V SEM with BSE, SE, and EDS capabilities. The microscope used for each sample will be indicated in the text. Samples for microscopy were polished flat and mounted using carbon tape.

3.3 Transport Property Measurements

Samples for thermal and electrical transport measurements were cut to the appropriate dimensions using a diamond saw. Low temperature (80-300K) Seebeck coefficient, electrical resistivity, and

thermal conductivity measurements were conducted simultaneously on rectangular parallelepiped samples (approximately 3×3×6 mm) in a Janis model ST-100 cryostat cooled with flowing liquid nitrogen. A silver-filled epoxy was used to fix one end of the sample to a copper block, the other end to a 800-1000 Ω metal-film resistor, and two thin copper strips along the length of the sample (see Figure 3.2). Two thermocouples made from copper and constantan wires (<0.1mm diameter) were soldered directly to the copper strips. Electrical resistivity (ρ) was measured using a standard 4-point probe DC technique (I_S represents current supplied to the sample), utilizing the two copper leads of the thermocouples as the voltage probes. The Seebeck coefficient (S) and thermal conductivity (κ) were measured simultaneously by passing a current through the metal-film resistor (I_H), thereby generating a temperature gradient (ΔT) through the sample, and waiting for the system to reach steady-state (ΔT constant). The Seebeck coefficient was then calculated as follows:

$$S = \frac{\Delta V}{\Delta T} \tag{3.1}$$

where ΔV is the thermally induced voltage (Seebeck voltage) measured using the copper leads of the thermocouples. The measured thermoelectric voltage includes a contribution due to the leads, but because of the large Seebeck coefficients of the samples, this contribution is generally less than 1% of the total. The thermal conductivity was calculated according to:

$$\kappa = \frac{I_H V_H}{\Delta T} \frac{l}{s} \tag{3.2}$$

where V_H, l, and s are the measured voltage across the resistor, distance between the thermocouples, and sample cross sectional area, respectively. All measurements were conducted under vacuum ($< 10^{-5}$ torr) to minimize radiation losses. A standard fused quartz sample was used as a calibration standard for thermal conductivity, and the thermal conductivity data reported here have been corrected for parasitic and radiation heat losses. Labview© software was used for automated

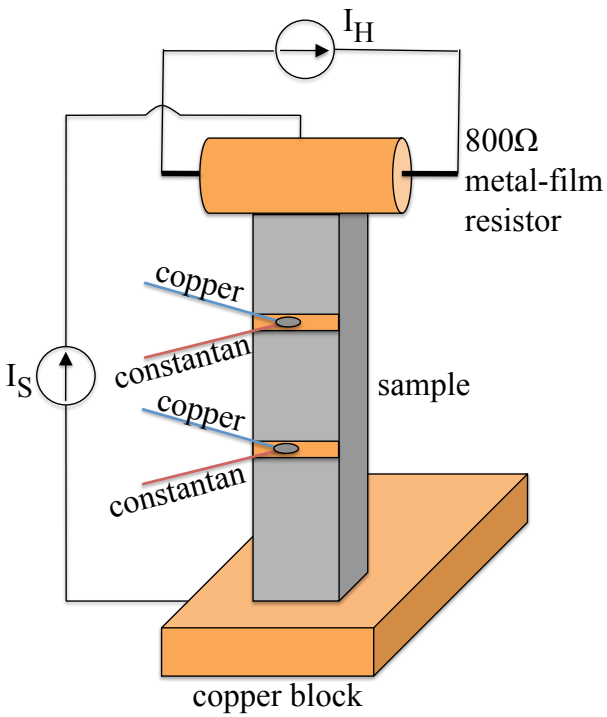

Figure 3.2: Schematic representation of experimental setup used for low temperature measurements of Seebeck coefficient, electrical resistivity, and thermal conductivity.

data collection.

High temperature (300-1073K) electrical resistivity and Seebeck coefficient measurements were performed using the ULVAC ZEM-3 measurement system. Parallelepiped samples (approximately 3×3×6 mm) were used for the measurements. The ends of the sample were clamped between nickel electrodes, and two spring-loaded type R thermocouples were placed along the length of the sample (approximately 3 mm apart). Resistivity was measured using a standard 4-point probe DC technique, utilizing the thermocouples as voltage probes. The Seebeck coefficient was measured by generating a localized temperature gradient through the sample and measuring both the voltage drop and the temperature difference between the thermocouples. All measurements were performed under vacuum (backfilled with high purity He) to minimize conduction

and convection losses, and the instrumentation was calibrated using a standard constantan sample. High temperature thermal conductivity data were calculated from thermal diffusivity (α, measured using LFA-457 from Netzsch), specific heat capacity (c_p, measured using DSC 200 F3 Maia from Netzsch, ASTM E1269-05 method), and density (ρ_o, measured using Archimedes method) measurements according to:

$$\kappa = \alpha \cdot c_p \cdot \rho. \tag{3.3}$$

Thermal diffusivity measurements were conducted on thin plate samples ($\sim$ 1mm thickness) and density and specific heat measurements were conducted on small ($<$100 mg) sections of material.

Low temperature (50-300K) Hall effect measurements were carried out using one of two similar systems. In both cases thin plate samples (approximately $3\times8\times1$ mm) were used, and all connections were made using thin (0.127 mm diameter) silver wire and a silver-filled adhesive. A constant magnetic field was applied in the direction normal to the sample plane while an AC current was passed along the length of the sample, and the transverse voltage (Hall voltage, V_H in Figure 3.3) was measured across the width of the sample. The Hall coefficient (R_H) was calculated from the slope of the Hall voltage versus field curve. The electrical resistivity was measured simultaneously by monitoring the sample voltage (V_S) in the absence of a magnetic field. The carrier concentration (n) and mobility (μ) were then calculated from:

$$R_H = \frac{1}{ne} \tag{3.4}$$

and

$$\rho = \frac{1}{ne\mu} \tag{3.5}$$

where e is the electronic charge 1.602×10^{-19} C.

The Versalab measurement system (Quantum Design) utilized a superconducting magnet (-3

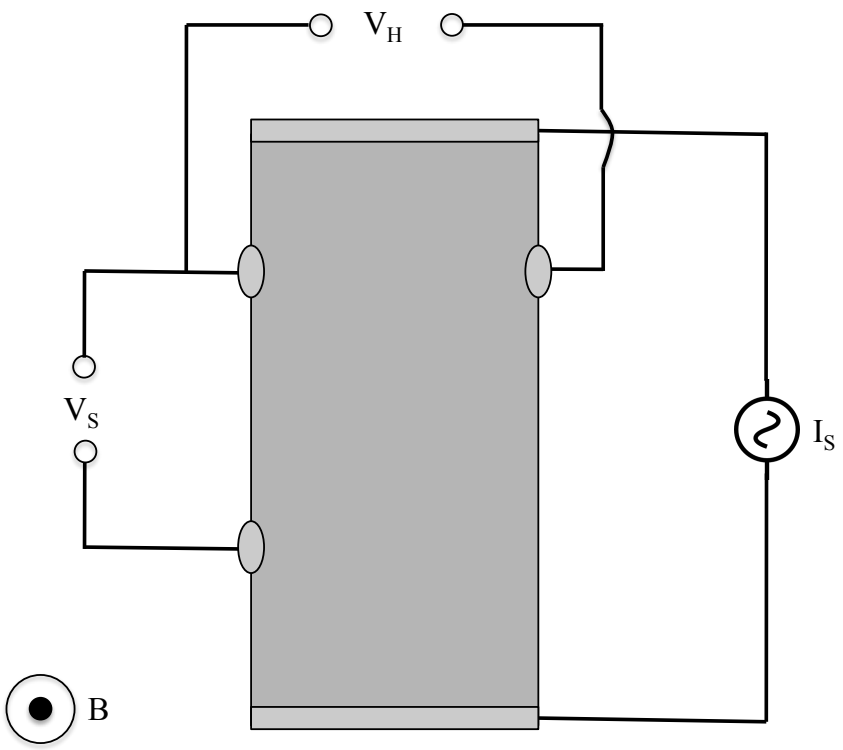

Figure 3.3: Schematic representation of experimental setup used for low temperature Hall measurements, pictured normal to the sample thickness.

to 3 Tesla) and a closed-loop He compressor to achieve the proper measurement environment. The MultiView© software package was used for data collection. The other system utilized a liquid nitrogen cooled Janis model ST-300 cryostat and a water-cooled electromagnet (-2.5-2.5 Tesla) to achieve the measurement environment. A LakeShore model 370 AC resistance bridge and the LabView© software package were used for data collection.

4 Rocksalt-Like Cu-Based Ternary Compounds

4.1 Background and Motivation

With the success of $AgSbTe_2$ and its related compounds, the logical first step is to investigate Cu-based ternary compounds with rocksalt-like crystal structures as a low cost alternatives to Ag-based thermoelectrics. Although no Cu-based rocksalt-like ternary compounds have been reported for thermoelectric applications, several have been mentioned in the literature. Zhuze *et. al.* [34] reported that the compound $CuBiSe_2$ had a rocksalt-like structure (similar to $AgSbTe_2$) with a = 0.569 nm and later Spitzer [46] reported a low room temperature lattice thermal conductivity (1.1 W/mK) for the same compound. Subsequently, three separate investigations into the Cu-Bi-Se ternary system have found no evidence of a $CuBiSe_2$ phase [47]-[49].

Two of the three reports on the Cu-Bi-Se ternary system identified a different composition, Cu_3BiSe_3, as having a rocksalt-like crystal structure with a = 0.587 nm [47], [48]. Spitzer [46] and Pollak *et. al.* [50] reported a low room temperature lattice thermal conductivity (1.1 W/mK) for this compound. In contrast, Karup-Moller found no evidence of a phase corresponding to Cu_3BiSe_3. Karup-Moller and Garcia agree on the existence of the ternary compound with nominal composition $CuBi_3Se_5$ (Garcia uses $Cu_{1.6}Bi_{4.8}Se_8$), which was identified by Karup-Moller as $Cu_{1.7}Bi_{4.7}Se_8$. Makovicky *et. al.* later refined the composition and crystal structure of this compound as $Cu_{1.78}Bi_{4.73}Se_8$ (monoclinic, space group C2/*m* [52]). Although this compound does not have the rocksalt crystal structure, it is investigated here for completeness. The contradicting reports in the literature regarding rocksalt-like $CuBiSe_2$ and Cu_3BiSe_3 along with their apparently low lattice thermal conductivities prompted the present investigation into the Cu-Bi-Se ternary system.

4.2 Experimental

All samples studied here were synthesized by direct fusion at 750°C as described in section 3.1. Since no synthesis information or phase diagrams are available for $CuBiSe_2$, samples were cooled either by quenching in water from 750°C or by slow cooling from 750°C to 400°C at 0.3°C/min, annealing for 48-96 hours, and cooling to room temperature at 0.3°C/min. The phase diagram produced by Garcia *et. al.* indicates that Cu_3BiSe_3 forms via a peritectic reaction at 588°C [48], and thus samples were prepared by quenching in water to avoid the formation of secondary phases. Samples were also prepared by slow cooling and annealing (as described for $CuBiSe_2$) for comparison. Samples with composition $CuBi_3Se_5$ (or $Cu_{1.6}Bi_{4.8}Se_8$), $Cu_{1.7}Bi_{4.7}Se_8$, and $Cu_{1.78}Bi_{4.73}Se_8$ were prepared by slow cooling from 750°C to room temperature at 0.3°C/min. All samples for SEM analysis were cut from the ingots, polished flat, and studied using the JEOL 6400V microscope (MSU CAM). Samples for transport property measurements were cut directly from the ingots.

4.3 Results and Discussion

4.3.1 $CuBiSe_2$

Samples prepared with the starting composition $CuBiSe_2$ formed different phases depending on the synthesis method. Upon slow cooling to 400°C and annealing, the samples solidified in two separate regions of the ampoule as shown in Figure 4.1. XRD revealed the top portion to be single-phase α-Cu_2Se, which has the rocksalt structure with a = 5.84 Å (upper right, Figure 4.1) [53], while the bottom portion was composed of $Cu_{1.78}Bi_{4.73}Se_8$, which has a monoclinic structure with a = 1.3759 nm, b = 0.41684 nm, c = 1.4683 nm, and β = 115.61°(lower right, Figure 4.1) [52].

The separation of Cu_2Se and $Cu_{1.78}Bi_{4.73}Se_8$ indicates that these phases are completely immiscible, which likely caused the crystallization in separate portions of the ampoule during slow

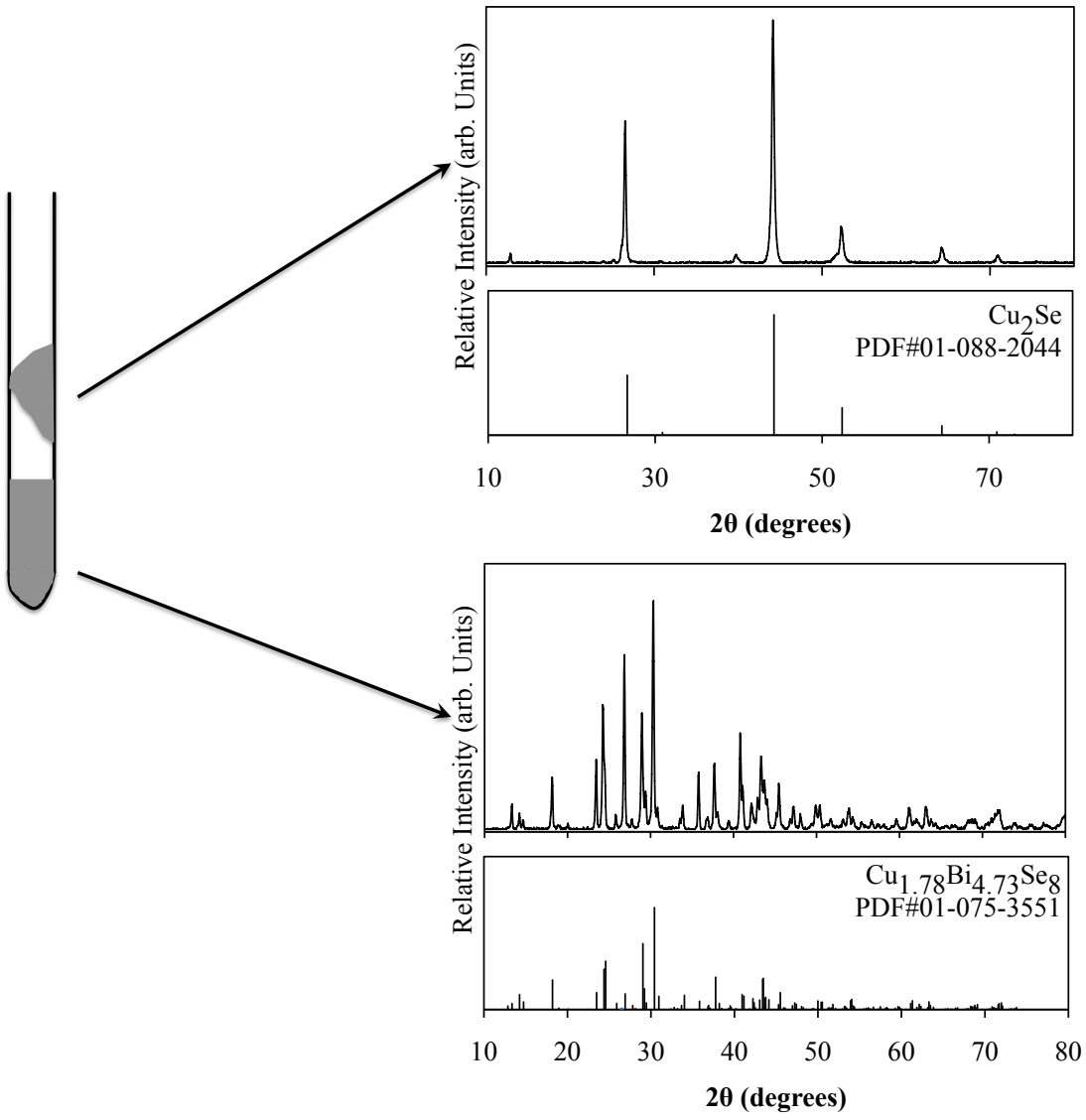

Figure 4.1: Schematic representation of an as-synthesized $CuBiSe_2$ sample after slow-cooling and annealing at 400°C (left), XRD pattern of the top portion and powder diffraction file (PDF) for Cu_2Se (upper right), and XRD pattern of the lower portion and PDF for $Cu_{1.78}Bi_{4.73}Se_8$.

cooling from 750°C. It is interesting to note that the lattice parameter of the Cu_2Se phase is similar to that reported for $CuBiSe_2$ by Zhuze *et. al.* [34]. Although they do not give specific synthesis details, it is mentioned that their samples were synthesized in evacuated quartz ampules that were drawn slowly out of a furnace to obtain large crystals. Based on the results above, the slow removal of a $CuBiSe_2$ sample from the furnace would more than likely result in formation of Cu_2Se and $Cu_{1.78}Bi_{4.73}Se_8$ crystals in different portions of the ampoule. If a Cu_2Se crystal was selected by Zhuze for XRD analysis, it is possible that this binary compound was mistakenly identified as $CuBiSe_2$.

In an attempt to avoid phase separation, several samples were prepared by quenching from 750°C into water. These samples solidified in one piece as expected, but XRD revealed them to be multiphase (see Figure 4.2). Quenched samples were composed primarily of $Cu_{1.78}Bi_{4.73}Se_8$, along with a smaller portion of the high temperature phase of Cu_2Se (β-Cu_2Se, monoclinic, $a = c$ = 1.230 nm, b = 4.074 nm, β = 120°[53]). Annealing the quenched samples for periods of up to 2 weeks at moderate temperatures (250 - 400°C) had no effect on the multiphase microstructure. From these results it is concluded that a $CuBiSe_2$ rocksalt structure phase is not a thermodynamically stable compound.

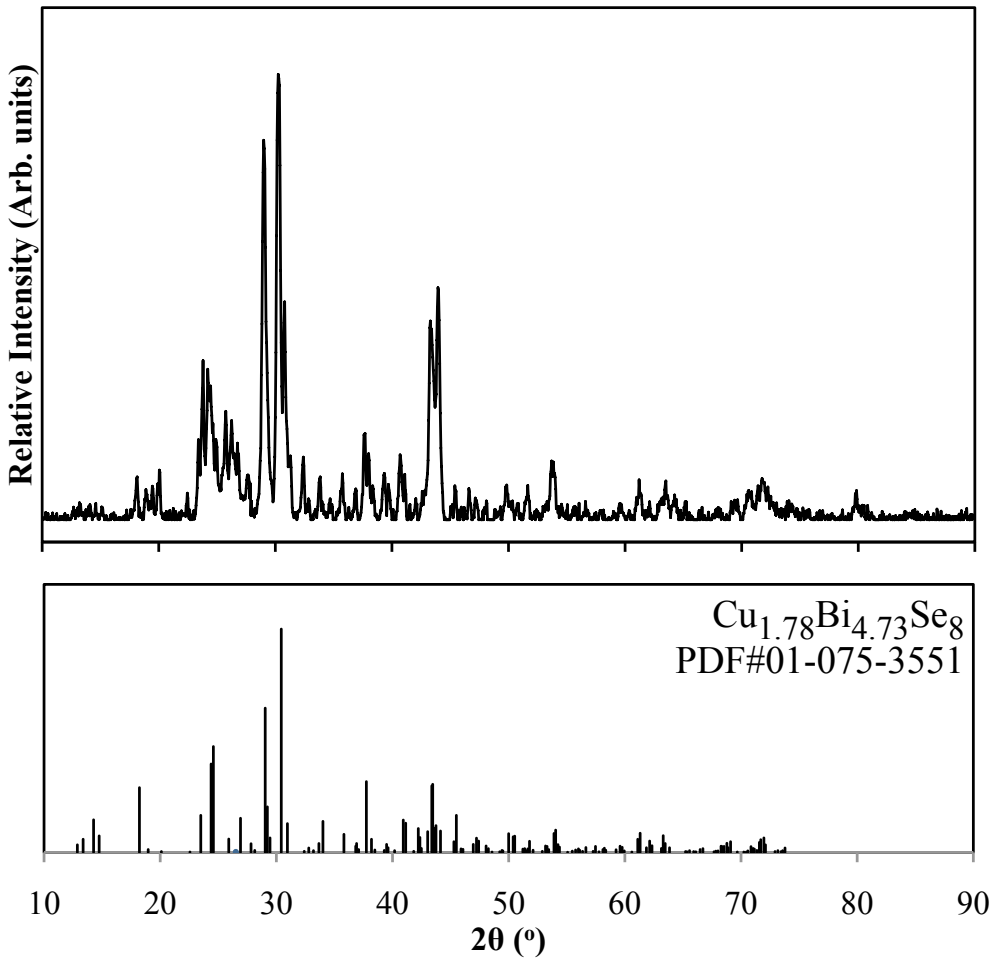

Figure 4.2: XRD pattern of a quenched $CuBiSe_2$ sample and PDF for $Cu_{1.78}Bi_{4.73}Se_8$.

4.3.2 Cu_3BiSe_3

Samples prepared with the starting composition Cu_3BiSe_3 formed multiple phases regardless of the synthesis method. Samples slow cooled from 750°C to 400°C at 0.1°C/min, annealed for 4 days, and cooled to room temperature at 0.1°C/min had a distinctly different XRD pattern than those quenched in water from 750°C to room temperature, as shown in Figure 4.3(a) and (b). Clearly neither of these samples have the single-phase rocksalt structure reported by Golovei (Figure 4.3(c) [47]), but in both patterns (a) and (b) the reported peaks all appear to be present. The remaining peaks in both patterns could not be indexed using the computer software, therefore these samples were examined using scanning electron microscopy (backscattered electron (BSE) imaging) and energy dispersive X-ray sepctroscopy (EDS).

The EDS X-ray map of slow-cooled Cu_3BiSe_3 sample shown in Figure 4.4 clearly indicates the presence of two phases. The BSE image (upper left, Figure 4.4) shows light and dark regions, indicating differences in average atomic mass. The X-ray maps indicate that the light regions are Bi-rich whereas the dark regions are Bi-poor (white pixel indicates that the element was detected, black pixel indicates that the element was absent). The average compositions of the light and dark regions are given in Table 4.1, neither of which correspond to Cu_3BiSe_3. The compositions indicate that Cu, Bi, and Se are present in both of the regions, but neither correlate to any known ternary phase in the Cu-Bi-Se system. This could mean that this sample contains a finer distribution of binary Cu-Se and Bi-Se phases than detected here, but since this multiphase microstructure is stable even after extended annealing it was not investigated further.

The BSE image of a quenched Cu_3BiSe_3 sample (Figure 4.5) appears to be nearly single phase, with only a small amount of a light phase which is concentrated primarily at the grain boundaries. EDS analysis of the grain boundary region (Figure 4.6) shows that the light region is slightly Bi-rich and Cu-poor while the surrounding dark region appears to contain an even distribution of Cu, Bi, and Se. The compositions of the light and dark regions given in Table 4.2 confirm that the grain boundary region does contain a second phase with Cu, Bi, and Se present. The majority phase,

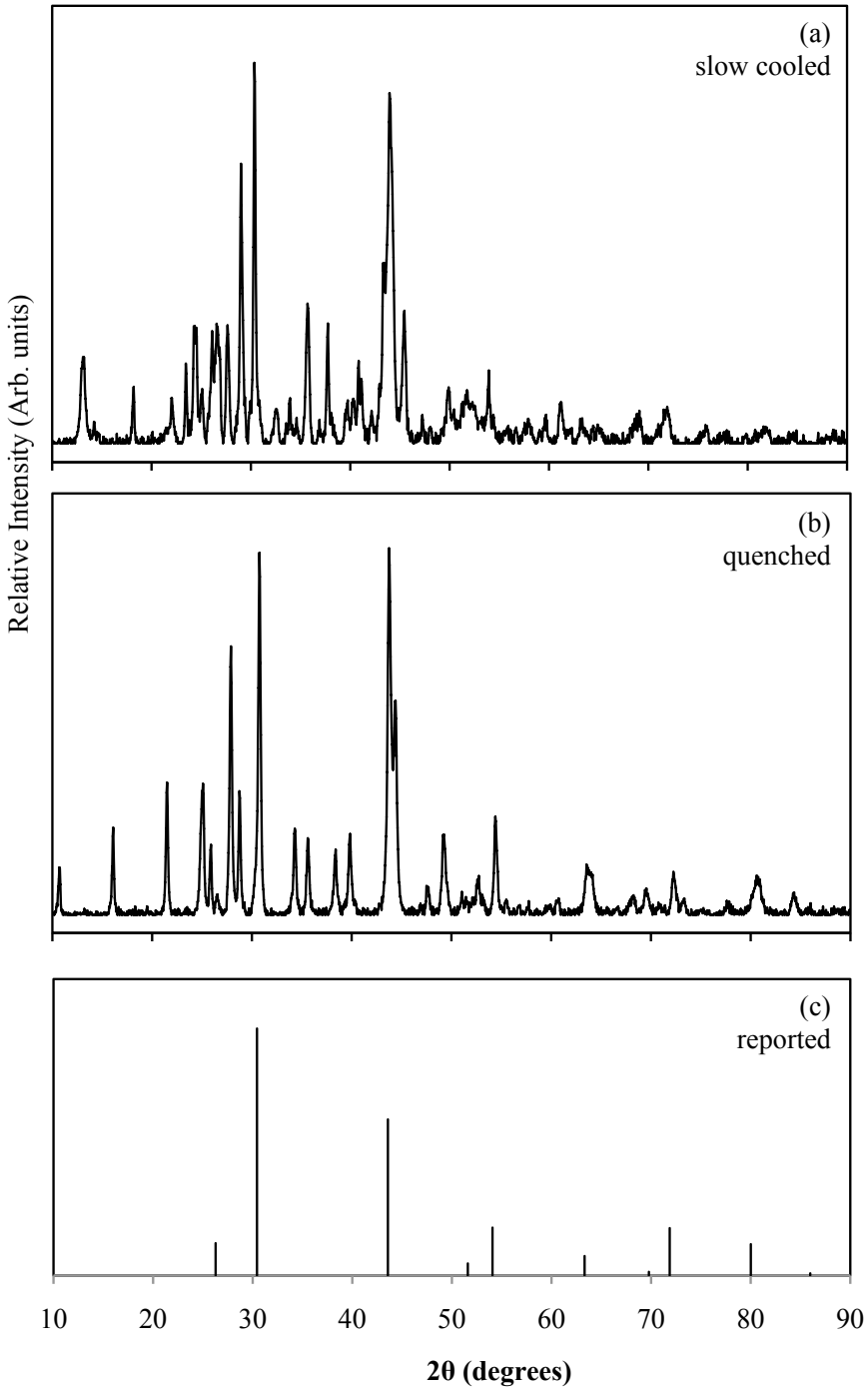

Figure 4.3: XRD patterns from Cu_3BiSe_3 samples that were (a) slow cooled from 750°C to 400°C and annealed for 4 days and (b) quenched in water from 750°C, along with the reported pattern for rocksalt Cu_3BiSe_3 [47].

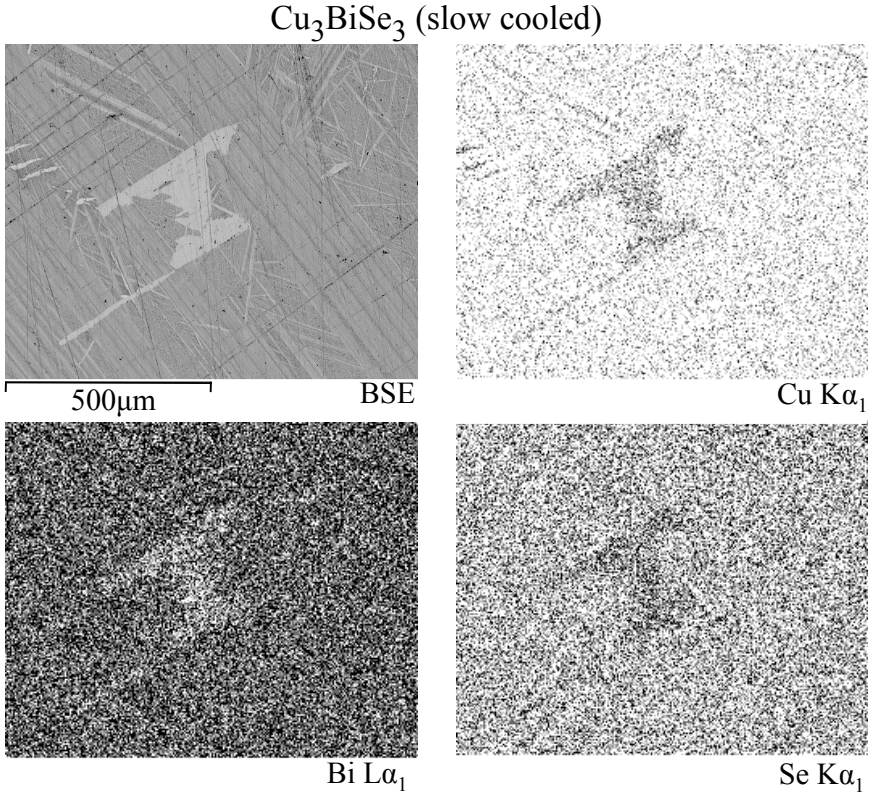

Figure 4.4: EDS X-ray mapping of a slow cooled Cu_3BiSe_3 sample. Upper left BSE image shows the mapped region, remaining images show the distribution of Cu, Bi, and Se as indicated.

Table 4.1: Average compositions (determined by EDS) of the light and dark phase regions in the slow cooled Cu_3BiSe_3 sample shown above.

	Average Composition (at%)	
Element	Light Region	Dark Region
Cu	28.0%	38.3%
Bi	35.8%	15.9%
Se	36.2%	45.8%

Table 4.2: Average compositions (determined by EDS) of the light and dark phase regions in the quenched Cu_3BiSe_3 sample shown above.

	Average Composition (at%)	
Element	Light Region	Dark Region
Cu	41.4%	24.2%
Bi	15.6%	31.8%
Se	43.0%	44.0%

Table 4.3: Measured and reported room temperature thermoelectric properties of Cu_3BiSe_3

Property	This Work	Pollak *et. al.* [50]
Seebeck Coefficient (μV/K)	41.7	40.0
Electrical Resistivity (mΩ*cm)	5.2	3.0
Thermal Conductivity (W/m*K)	0.8	1.1

however, has a composition very near stoichiometric Cu_3BiSe_3. This indicates that, in contrast to Karup-Moller [49], the ternary compound Cu_3BiSe_3 does exist although based on the XRD pattern in Figure 4.3(b) it likely has a more complex crystal structure than rocksalt. The room temperature thermoelectric properties of the quenched Cu_3BiSe_3 sample, given in Table 4.3, are in reasonable agreement with those reported by Pollak *et. al.* [50]. The compound possesses a very low thermal conductivity but poor electronic properties and thus ZT values not exceeding 0.013 at room temperature. The microstructure remained the same after extended periods of annealing at intermediate temperatures, and the thermoelectric properties were not improved. In particular, the very low Seebeck coefficient in this compound could not be increased by extended annealing or small compositional variations, which eliminates the possibility of optimizing the thermoelectric properties through doping.

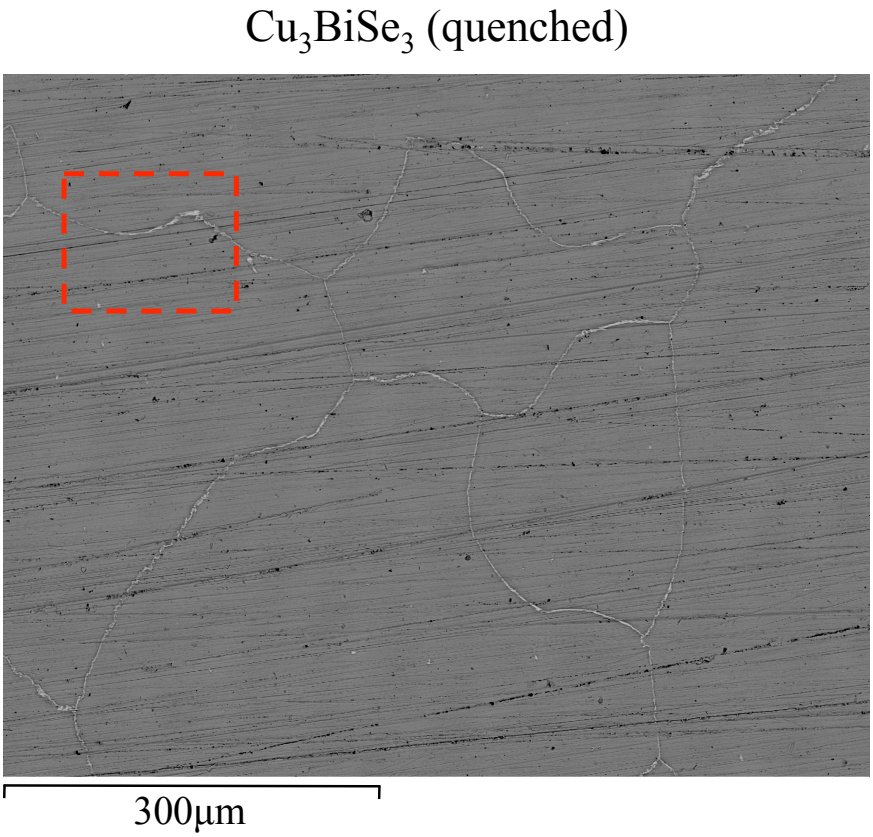

Figure 4.5: BSE image of a quenched Cu_3BiSe_3 sample, showing phase separation at the grain boundaries. Dashed line indicates region selected for X-ray mapping, shown in Figure 4.6 below.

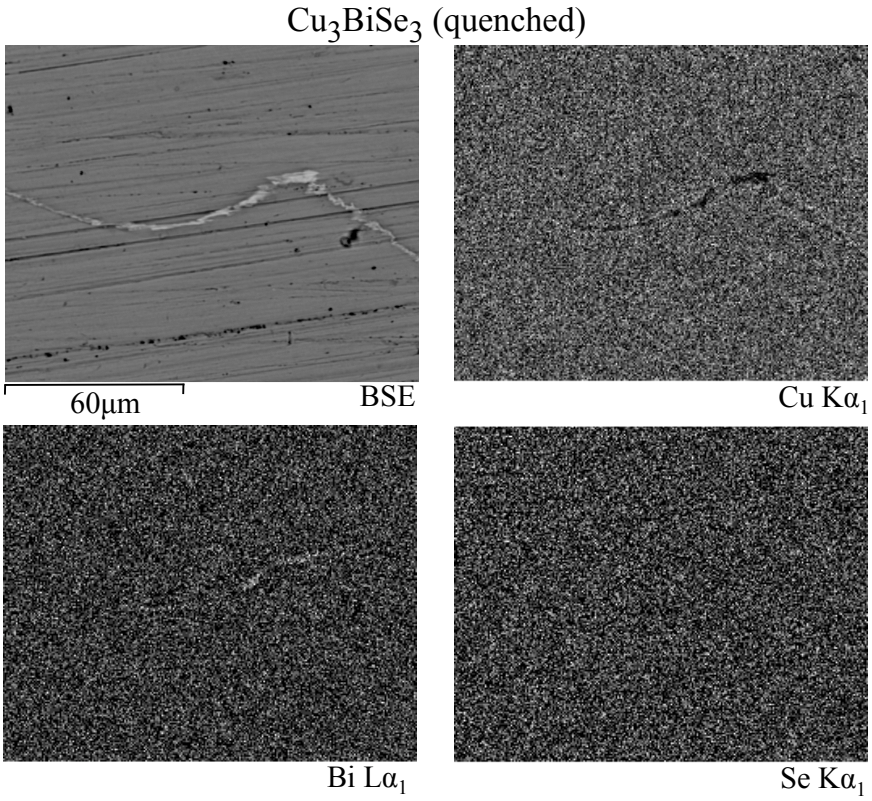

Figure 4.6: EDS X-ray mapping of a quenched Cu_3BiSe_3 sample. Upper left BSE image shows the mapped region, remaining images show the distribution of Cu, Bi, and Se as indicated.

4.3.3 Other Cu-Bi-Se Ternary Compounds

The exact composition and crystal structure of the $CuBi_3Se_5$ phase has been the subject of some debate in the literature. Garcia *et. al.* first identified the phase as $Cu_{1.6}Bi_{4.8}Se_8$ (triclinic, *P1*, a = 4.168 Å, b = 7.182 Å, c = 13.39 Å, $\alpha = 85.27^\circ$, $\beta = 81.15^\circ$, $\gamma = 73.16^\circ$[48]), Karup-Moller reported $Cu_{1.7}Bi_{4.7}Se_8$ without giving crystallographic data [49], and most recently Makovicky *et. al.* found evidence of $Cu_{1.78}Bi_{4.73}Se_8$ (monoclinic, *C2/m*, a = 13.759 Å, b = 4.168 Å, c = 14.683 Å, and $\gamma = 115.61^\circ$[52]). Samples with each of the above compositions were synthesized by cooling slowly from 750°C, and in all cases their crystal structure corresponded to that of $Cu_{1.78}Bi_{4.73}Se_8$, as shown in Figure 4.7. This result suggests that the $CuBi_3Se_5$ compound has a relatively large phase region and thus can tolerate minor changes in composition.

The thermoelectric properties of these compounds are shown in Figure 4.8. All samples exhibited p-type conduction as evidenced by their positive Seebeck coefficients. The temperature dependence of the resistivity is characteristic of a heavily doped semiconductor, in agreement with the relatively modest room temperature Seebeck coefficients. More interestingly, the temperature dependence of the lattice thermal conductivity (the electronic contribution is negligible as calculated from the Weidemann-Franz law) is characteristic of an amorphous material, and is well below 1 W/m*K for all samples over the entire temperature range. For a typical crystalline material, the lattice thermal conductivity will increase rapidly with decreasing temperature as T^{-1} due to vanishing phonon-phonon scattering processes. For these compounds, there is clearly an inherent anharmonicity in the lattice that strongly scatters phonons and limits their mean free path even at low temperatures. Considering the nominal composition $CuBi_3Se_5$, a simple valence assessment reveals that the Bi atoms should be in the 3+ valence state. Thus, as in the case of $AgSbTe_2$, it is possible that the nonbonding lone-pair electrons around Bi contribute to increased anharmonicity in the lattice, which will be revisited in Chapter 6.

Despite very low thermal conductivity, the $CuBi_3Se_5$ compounds have low ZT values at room temperature, mainly because of their large electrical resistivity. Rigorous doping studies were not

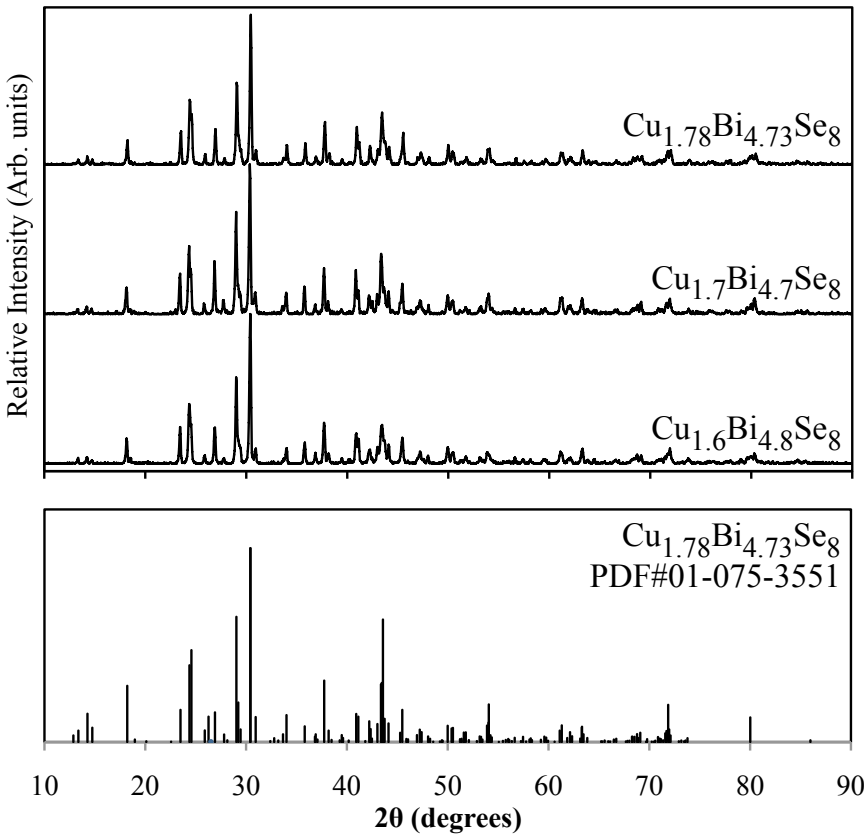

Figure 4.7: XRD patterns of $CuBi_3Se_5$ compounds prepared with different starting compositions as indicated. Lower plot shows the powder diffraction file (PDF) for $Cu_{1.78}Bi_{4.73}Se_8$, reported by Makovicky *et al* [52].

performed on these compounds since their Seebeck coefficients were already low ($\sim$70 μV/K at 300K) without any doping.

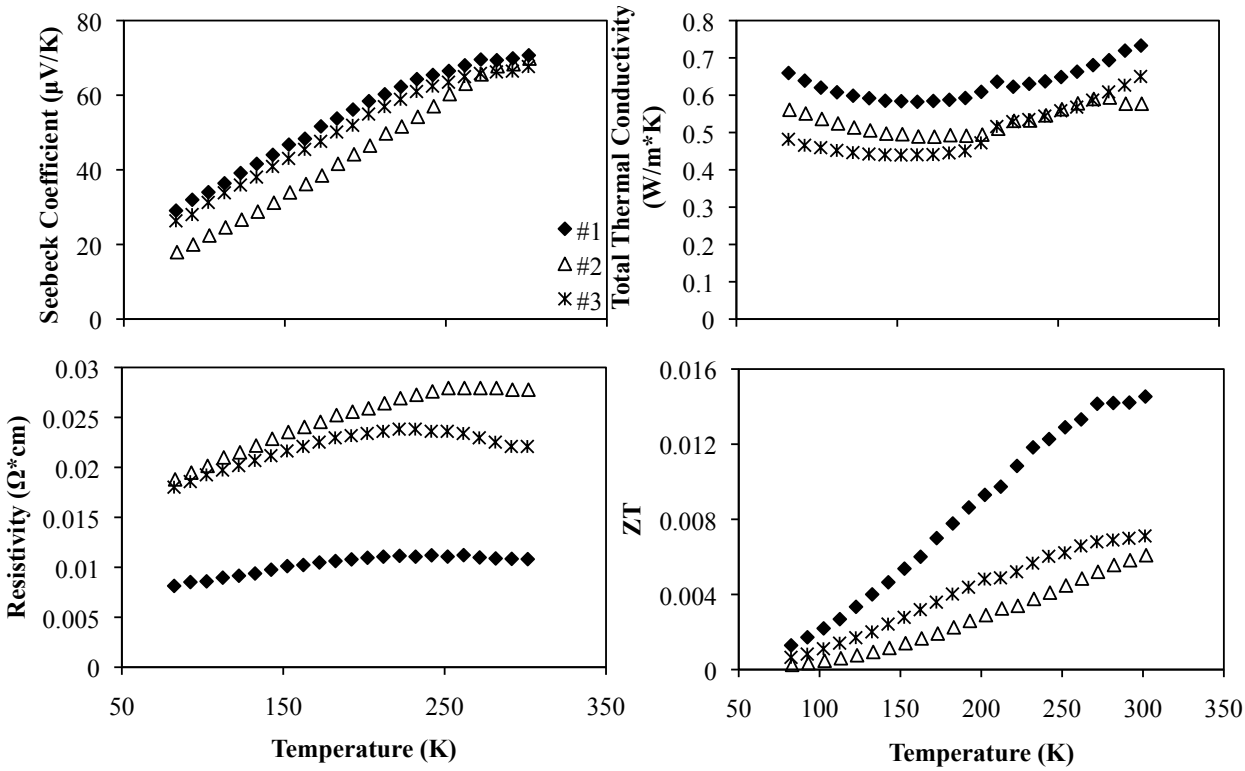

Figure 4.8: Low temperature thermoelectric properties of $CuBi_3Se_5$ compounds. Compositions of the samples are: #1 - $Cu_{1.6}Bi_{4.8}Se_8$, #2 - $Cu_{1.7}Bi_{4.7}Se_8$, #3 - $Cu_{1.78}Bi_{4.73}Se_8$.

4.4 Summary

From this portion of the work it is concluded that the previously reported ternary Cu-based rocksalt-like compounds do not exist. Following the procedure of $AgSbTe_2$, the Cu-V-VI_2 family of compounds were investigated focusing on $CuBiSe_2$, which was reported as having the rocksalt-like structure. Samples of $CuBiSe_2$ prepared by slow cooling crystallized in two separate regions of the ampoule, the upper portion corresponding to rocksalt α-Cu_2Se and the lower portion corresponding to monoclinic $Cu_{1.78}Bi_{4.73}Se_8$. The authors that reported rocksalt-like $CuBiSe_2$ used a slow-cooling synthesis procedure and likely selected an α-Cu_2Se crystal for XRD analysis, leading them to believe that their $CuBiSe_2$ sample had the rocksalt structure. Quenched samples of $CuBiSe_2$ contained primarily $Cu_{1.78}Bi_{4.73}Se_8$ along with smaller amounts of β-Cu_2Se. The presence of $Cu_{1.78}Bi_{4.73}Se_8$ provides an explanation for the reported low thermal conductivity of

$CuBiSe_2$, since $Cu_{1.78}Bi_{4.73}Se_8$ has a very low thermal conductivity.

The other ternary Cu-based rocksalt-like compound reported in the literature, Cu_3BiSe_3, was investigated in a similar fashion. Samples prepared by slow cooling and quenching had distinctly different XRD patterns, neither of which were readily indexed using the JCPDS database. SEM and EDS analysis revealed that in both cases a multiphase microstructure was present. Large regions of a Bi-rich phase were detected in slow cooled samples, while in quenched samples the Bi-rich phase was concentrated at the grain boundaries. The majority phase in the quenched samples corresponded to stoichiometric Cu_3BiSe_3, although a purely single phase microstructure could not be obtained even after extended annealing treatments. The measured thermoelectric properties of quenched Cu_3BiSe_3 were in reasonable agreement with those previously reported. The thermal conductivity is quite low, but the extremely low thermoelectric power factor resulted in low ZT values. The thermoelectric properties were not improved after extended annealing treatments.

The ternary compound having nominal composition $CuBi_3Se_5$ was studied for completeness. Samples with starting compositions $Cu_{1.6}Bi_{4.8}Se_8$, $Cu_{1.7}Bi_{4.7}Se_8$, and $Cu_{1.78}Bi_{4.73}Se_8$ were prepared in accordance with three separate literature studies on the $CuBi_3Se_5$ compound. All samples consisted of a single phase corresponding to $Cu_{1.78}Bi_{4.73}Se_8$, which has a monoclinic structure. This compound was found to have an extremely low thermal conductivity but poor electronic properties, leading to modest ZT values. The temperature dependence of the thermal conductivity resembles that of an amorphous material, which indicates a strong intrinsic phonon scattering mechanism that limits the phonon mean free path to near its minimum value even at low temperatures. Gaining a better understanding of this mechanism could help to identify other materials with intrinsically minimal thermal conductivity, which is of significant interest for the development of new thermoelectric materials as will be discussed in Chapter 6.

5 Diamond-Like Cu-Based Ternary Compounds

5.1 Background and Motivation

5.1.1 Why Study Diamond-Like Cu-Based Ternary Compounds?

The absence of rocksalt-like Cu-based ternary compounds eliminates the possibility of extending the $AgSbTe_2$ approach beyond the Ag-based systems. The methodology used to derive $AgSbTe_2$, however, can be applied to compounds with different crystal structures. Consider the well-known group IV semiconductors Si and Ge with the diamond cubic crystal structure. It is known that by replacing the Si or Ge atoms in equal proportions with group III and V or group II and VI atoms, the valence electron to atom ratio is constant (4 valence electrons per atom, allowing for sp^3 hybridization of the valence electron orbitals and therefore tetrahedral coordination) and a diamond-like structure is maintained, which is called the zincblende structure since two distinct atomic species are present. Group III-V and II-VI semiconductors such as GaAs and CdTe are well established technological materials with a wide array of applications. Now consider two unit cells of a II-VI semiconductor (say Zn_2Se_2, for convenience) and replace the Zn atoms with Cu and In atoms in equal proportions, thereby formulating the compound $CuInSe_2$. In the same way as $AgSbTe_2$ is derived from PbTe, $CuInSe_2$ is derived from ZnSe and maintains a diamond-like structure known as the chalcopyrite structure. Here the valence electron to atom ratio is still equal to 4, allowing for tetrahedral coordination among the constituent atoms.

The I-III-VI_2 family of compounds (sometimes referred to as chalcopyrite compounds) are well characterized and have found various applications, most notably as photovoltaic materials due to their favorable band gaps. Solid solutions of $CuInSe_2$ and $CuGaSe_2$ (dubbed CIGS compounds) are some of the best known materials for thin film solar cells, with efficiencies approaching 20% [54]. The chalcopyrite compounds are not well suited for thermoelectric applications due to their relatively high thermal conductivities, in the range of 5 to 9 W/m*K at room temperature [55], and

large bandgaps in the range of 1 to 2 eV.

This approach can be expanded further by considering higher-order ternary derivatives of the II-VI semiconductors. Starting with three II-VI unit cells and replacing the group II atoms with group I (Cu) and group IV (Ge, Sn) atoms in a 2:1 ratio, compounds of the form I_2-IV-VI_3 are formulated. In a similar fashion, compounds of the form I_3-V-VI_4 have unit cells 4 times larger than those of the II-VI compounds. The I_2-IV-VI_3 and I_3-V-VI_4 compounds have 4 valence electrons per atom and both maintain diamond-like crystal structures.

Increasing the size of the unit cell while maintaining the diamond-like crystal structure presents a distinct advantage for thermoelectric applications in that the lattice thermal conductivity of a given crystalline material is known to decrease with increasing size of the unit cell. Slack [45], and later Morelli and Slack [56], reviewed the thermal conductivity of nonmetallic crystals with $1 \leq n \leq 4$, where n is the number of atoms in the primitive crystallographic unit cell. Slack proposed the following expression for the n-dependence of the lattice thermal conductivity:

$$\kappa_L = \frac{B\bar{M}\delta(\theta_0)^3}{n^{2/3}T\gamma^2} \tag{5.1}$$

where B is a constant, $\bar{M}$ is the average atomic mass, δ is the average volume per atom, θ_0 is the average Debye temperature estimated from elastic constants or specific heat, T is the absolute temperature in Kelvin, and γ is the dimensionless Grüneisen constant [45]. It is clear from equation 5.1 that for a series of compounds with similar atomic mass and interatomic bonding, the lattice thermal conductivity should follow a $n^{-2/3}$ dependence at a fixed temperature T. Such a series is constructed in Table 5.1 using select compositions from the diamond-like families of compounds described above. Here $\kappa_{exp} \propto n^{-1.6}$, representing a more drastic decrease in thermal conductivity with increasing n than predicted by equation 5.1. This offers a novel route towards compounds with low intrinsic thermal conductivity, and thus increased thermoelectric figure of merit. The n-dependence of the forbidden band gap (see Table 5.1) also shows a favorable trend. It has been

shown [57] that, for thermoelectric applications, to avoid minority carrier conduction while allowing for high mobility and doping level, a band gap of approximately 10 k_BT is required, where k_B is Boltzmann's constant and T is the operating temperature. For most applications, this means that appropriate band gaps fall between 0.25 and 1 eV. From Table 5.1 it is clear that the I_2-IV-VI_3 and I_3-V-VI_4 families of compounds are promising candidates for thermoelectric applications, yet they have seen little exploration to that extent.

Table 5.1: Reported thermal conductivities and band gaps for a series of diamond-like semiconductors with increasing number of atoms per unit cell.

Compound	n (atoms)	κ_{exp} (W/m*K)	Band Gap (eV)	Reference
ZnSe	2	19.0	2.7	[45]
$CuInSe_2$	4	8.6	1.07	[58]
Cu_2SnSe_3	6	3.3	0.66	[58]
Cu_3SbSe_4	8	2.2	0.31	[58]

5.1.2 Third-Order Ternary Derivatives of II-VI: I_2-IV-VI_3 Compounds

Hahn and his coworkers reported the Cu_2-IV-VI_3 compounds as having the sphalerite crystal structure with lattice constants ranging from a = 0.53 - 0.604 nm [59]. Goryunova *et. al.* [60] previously reported on the existence of Ag-based compounds in this series, but Scott [61] later found no evidence of ternary phases where I = Ag. The compounds Cu_2SnSe_3 and Cu_2GeSe_3 have been the subjects of several crystallographic studies and sparse physical property characterization.

The crystal structure of Cu_2SnSe_3 has been the subject of some debate in the literature. Palatnik *et. al.* [62] and Sharma *et. al.* [63] reported a cubic unit cell for Cu_2SnSe_3 with a = 0.569 nm. Marcano *et. al.* [64] and Delago *et. al.* [65] recently reevaluated the crystal structure of Cu_2SnSe_3 using single crystal samples. They found additional low-angle peaks in the x-ray diffraction pattern corresponding to a lower symmetry unit cell, which they determined to be monoclinic (space

group Cc) with a = 0.6967 nm, b = 1.20493 nm, c = 0.69453 nm, and β = 109.19°[65]. The authors seem to agree that Cu_2SnSe_3 is a congruently melting compound which melts at 695°C.

Large discrepancies regarding the electronic properties of Cu_2SnSe_3 exist in the literature. While all authors agree that Cu_2SnSe_3 exhibits p-type semiconducting behavior, the reported resistivity values range from 2.53×10^{-3} to 1.67×10^{-1} Ω*cm and the reported Seebeck coefficients range from +51.1 μV/K to +250 μV/K [58], [67]. At the beginning of this work, no efforts to control the carrier concentration through doping had been completed on Cu_2SnSe_3.

The compound Cu_2GeSe_3 was originally reported as cubic with a = 0.555 nm [67], but was later found to have an orthorhombic unit cell with a = 1.1878 nm, b = 0.3941 nm, and c = 0.5485 nm [69]. Goryunova *et. al.* reported that Cu_2GeSe_3 could incorporate up to 14% excess Ge, and in the process transition from tetragonal to cubic symmetry [60]. Later Sharma and Singh studied the crystal structure and microhardness of Ge-deficient and Ge-rich Cu_2GeSe_3 [70]. They found the composition $Cu_2Ge_{0.85}Se_3$ to be monoclinic (a=0.5512 nm, b=0.5598 nm, c=0.5486 nm, β=89.7°) and $Cu_2Ge_{1.55}Se_3$ to be cubic (a=0.5569 nm), and obtained single-phase samples at all compositions bounded by these two compounds. In a subsequent paper they reported all compositions above or below $Cu_2Ge_{1.55}Se_3$ to be multiphase, with the cubic phase occurring only at $Cu_2Ge_{1.55}Se_3$ [71]. Spitzer reported a cubic compound having composition $Cu_2Ge_2Se_3$ with a low room temperature thermal conductivity (0.84 W/m*K) [46]. Subsequent studies on the crystal structure transformations and physical properties of these compounds are absent from the literature.

5.1.3 Fourth-Order Ternary Derivatives of II-VI: I_3-V-VI_4 Compounds

Wernick and Benson first mentioned compounds of the type Cu_3-V-VI_4 where V = As or Sb and VI = S or Se [33]. They reported Cu_3SbSe_4 to be cubic with a melting point of 425°C, and gave no further results. Pfitzner later conducted a thorough crystallographic study on the same compound and found the structure to be tetragonal (space group $I\bar{4}2m$ no. 121) with a =

0.56609 nm and c = 1.1280 nm [72]. Scott *et. al.* found that Cu_3SbSe_4 forms by a peritectic reaction at 390°C, indicating that the slow-cooled samples synthesized by Wernick and Benson likely contained impurity phases [73]. The electronic properties of Cu_3SbSe_4 have been reported by several authors, who agree that it is a narrow band gap semiconductor (Eg between 0.13 and 0.42 eV at 300K) [73], [74], [75]. Controlling the carrier concentration in undoped samples is a challenge due to large concentrations of intrinsic defects; the literature values span nearly an order of magnitude from 2.4×10^{18} cm^{-3} to 2×10^{19} cm^{-3}.

5.1.4 Outline for the Present Work

Based on the approach outlined in Section 5.1.1 and the literature review, the objectives for this portion of the work are as follows:

(1) Synthesize Cu_2SnSe_3, Cu_2GeSe_3, and Cu_3SbSe_4 using the technique described in Seciton 3.1. Resolve the inconsistencies in the literature regarding the crystal structures of these compounds.

(2) Explore solid solutions with related compounds; determine the evolution of the crystal structure, lattice thermal conductivity, carrier mobility, and thermoelectric properties with composition.

(3) Identify dopant species and evaluate the effect of doping on the thermoelectric properties of the compounds mentioned in (1).

(4) Determine the plausibility of these compounds as thermoelectric materials.

Since each of these compounds are unique in their crystal structure and physical properties, a separate section will be devoted to each. The synthesis methods and experimental results for each will be discussed individually.

5.2 Cu_2SnSe_3

5.2.1 Experimental

Samples of Cu_2SnSe_3 were reacted at 900°C for 12 hours in evacuated quartz ampoules. Samples were slow cooled at 0.3°C/min to 400°C, annealed for 1-4 days, and cooled to room temperature. To investigate high temperature phase modifications, some samples were quenched from 900°C into room temperature water.

5.2.2 Results and Discussion

Both slow cooling and quenching resulted in single phase material, as determined by x-ray diffraction. Closer examination of the x-ray patterns revealed subtle differences that indicate differences in the crystal structure. The x-ray pattern for the quenched sample (Figure 5.1) exactly matches that of cubic Cu_2SnSe_3 reported by Palatnik *et. al.* [62]. Additional low angle peaks are present in the pattern for the slow cooled sample (see inset, Figure 5.2) which, as pointed out by Delago *et. al.*[65], correspond to a monoclinic unit cell.

Figures 5.1 and 5.2 suggest that the structures proposed by Palatnik *et. al.* [62] and Delago [65] are both correct, and differ only because of differences in their sample preparation. The primary difference between the structures shown in Figures 5.1 and 5.2 is the ordering of Cu/Sn atoms on the cation sublattice. A random arrangement of Cu and Sn atoms leads to a higher symmetry cubic unit cell whereas an ordered arrangement of Cu and Sn atoms lowers the symmetry to monoclinic. In agreement with these results, Rivet [76] reported an order/disorder transformation in Cu_2SnSe_3 at 450°C.

Nominally undoped samples always displayed p-type conductivity, as confirmed by Seebeck and Hall coefficient measurements, but controlling the hole concentration in these samples proved to be a challenge. Separately made Cu_2SnSe_3 samples had hole concentrations in the range of 4×10^{18} cm^{-3} to 1×10^{21} cm^{-3} at room temperature. Samples that were quenched in water from

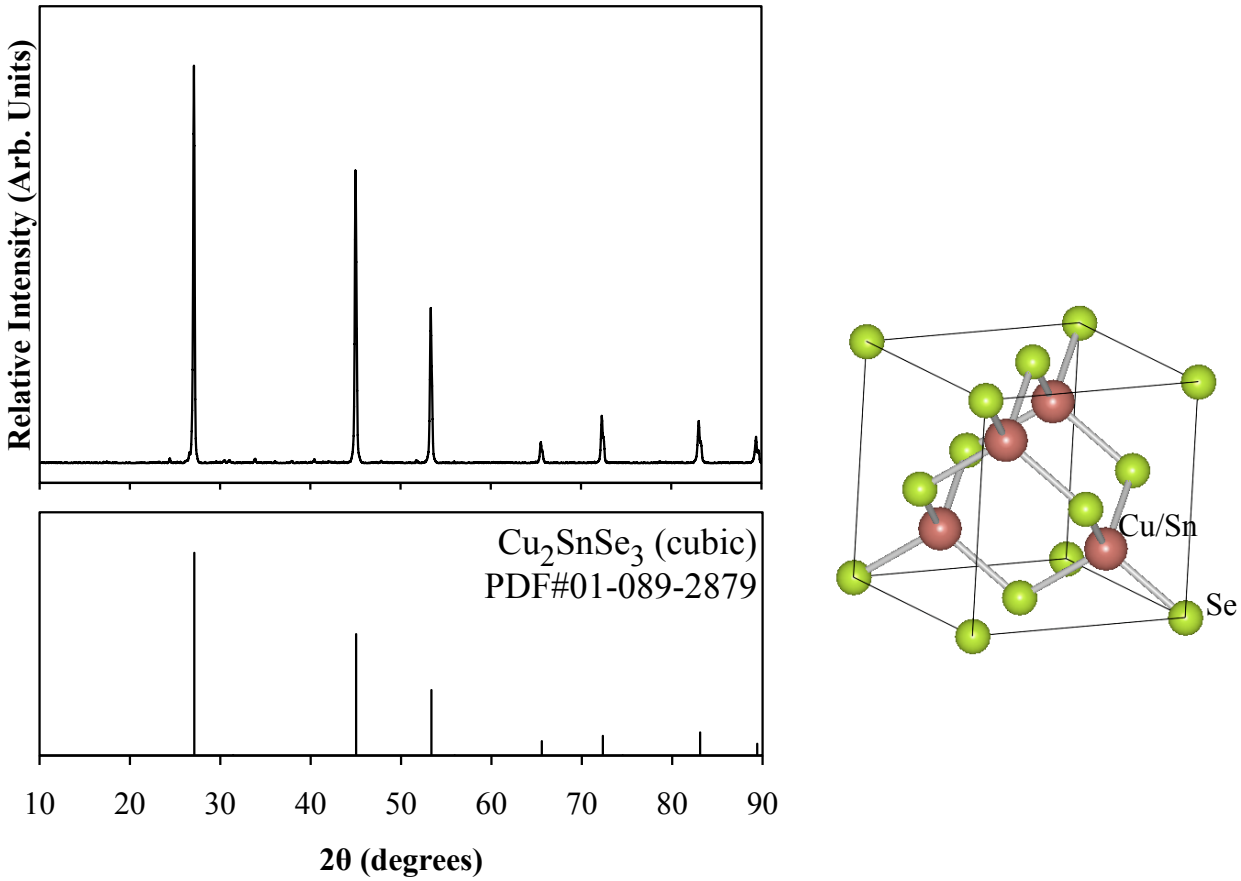

Figure 5.1: X-ray diffraction pattern for Cu_2SnSe_3 quenched in water from 900°C. All peaks correspond to the cubic phase, shown at right, where the larger spheres represent the random arrangement of Cu and Sn atoms on the cation sublattice.

900°C had hole concentrations greater than 10^{20} cm^{-3} at room temperature, presumably due to a large concentration of defects introduced during the quenching process. The inner walls of the ampoules became coated with a red/orange residue after quenching, likely caused by deposited Se vapor, which would promote a large concentration of Se vacancies in the Cu_2SnSe_3 lattice. A Se vacancy in the lattice would likely act as an acceptor impurity, thereby leading to very large hole concentrations.

For slow cooled samples, the hole concentrations were always less than 10^{20} cm^{-3}, but varied significantly from sample to sample and even between different Hall specimens cut from the same

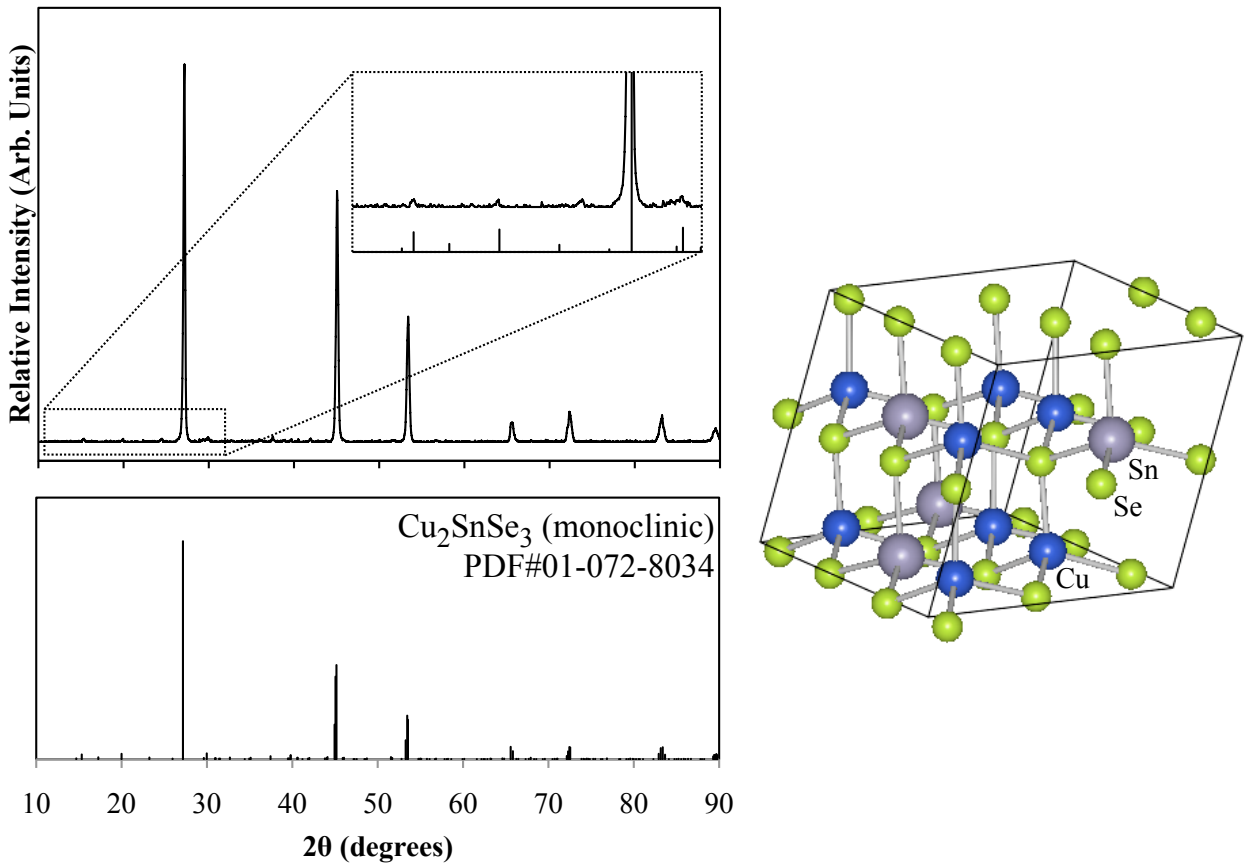

Figure 5.2: X-ray diffraction pattern for Cu_2SnSe_3 slow cooled and annealed at 400°C. Inset shows low angle peaks corresponding to the monoclinic structure, shown at right.

ingot. Annealing for up to 4 days at moderate temperatures (400°C) had no effect on the hole concentration. One possible explanation is that these samples suffer from localized compositional fluctuations that are not detectable using XRD. Cu_2SnSe_3 is known to have a large phase region, allowing for variations in composition while maintaining a single phase structure. In addition, compounds with similar compositions exist, namely $Cu_2Sn_{1-x}Se_3$ and Cu_2SnSe_4. Sharma *et. al.* reported that Sn-deficient Cu_2SnSe_3 had a cubic crystal structure up to $Cu_2Sn_{0.6}Se_3$, but reported no physical properties for these compounds [77]. Marcano et. al. found Cu_2SnSe_4 to be a p-type semiconductor with the zincblende crystal structure, with lattice constant very similar to that of Cu_2SnSe_3 (a = 5.6846(3) Å) [78]. It is important to note that the XRD peaks for Cu_2SnSe_4

nearly overlap those of Cu_2SnSe_3 (cubic and monoclinic phase), and thus the two compounds cannot be distinguished using XRD. They report a hole concentration of approximately 1.5×10^{21} cm^{-3} at room temperature for Cu_2SnSe_4, indicating that this compound could cause large hole concentrations if present in Cu_2SnSe_3. Samples of Cu_2SnSe_3 examined using EDS showed no detectable compositional variations, although EDS cannot distinguish between phases with similar average atomic mass.

Despite the challenges in controlling the hole concentration of Cu_2SnSe_3, doping studies were conducted to determine if the hole concentration could be consistently altered by introducing impurities into the compound. Ga and In were chosen as dopant species for the Sn site since they have one less valence electron and should act as acceptor impurities in the compound. The samples were synthesized by slow cooling from 900°C to 400°C, annealing for 24 hours, and slow cooling to room temperature. Taking the lowest measured hole concentration for Cu_2SnSe_3 as the "true" concentration, the hole concentration increases with increasing Ga and In content (see Figure 5.3, y = 0.01 and 0.025 not shown for clarity). When 5% Ga or In is added, the hole concentration is $\sim1.0\times10^{21}$ $^{-3}$, causing some difficulty in the measurement due to a weak Hall signal. The hole mobility (not shown) is $\sim$20 $cm^2/V*s$ for Cu_2SnSe_3 at 300K and decreases with increasing doping, falling below 10 $cm^2/V*s$ at 300K for all of the doped samples.

The low temperature thermoelectric properties of Ga-doped Cu_2SnSe_3 are shown in Figure 5.4. The electrical resistivity and Seebeck coefficient both decrease rapidly with increasing Ga content due to the increasing hole concentration. The thermal conductivity follows a T^{-1} temperature dependence as expected for these compounds in this temperature range due to phonon-phonon scattering. At room temperature the thermal conductivity increases slightly with Ga content due to an increased electronic contribution, which constitutes 13% of the total at room temperature for the 5% Ga sample (estimated from the Wiedemann-Franz law using $L_0 = 2.45\times10^{-8}$ $W*\Omega*K^{-2}$) . The 2.5% Ga sample has the largest ZT value, reaching 0.037 at room temperature. While this is a modest value, it represents nearly a 3-fold increase as compared to the room temperature ZT of

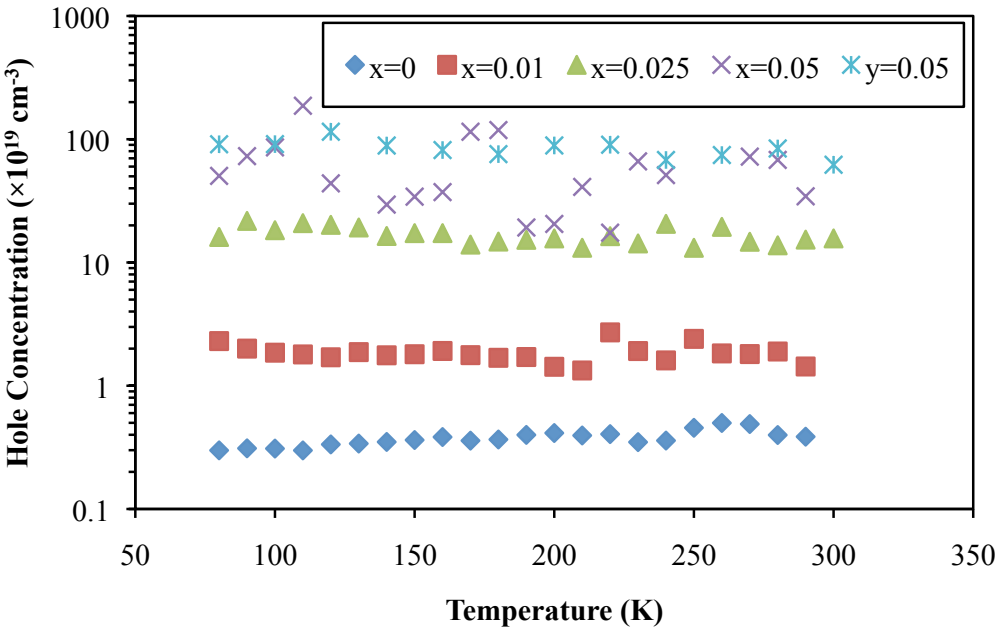

Figure 5.3: Temperature dependence of the hole concentration of $Cu_2Sn_{1-x}Ga_xSe_3$ and $Cu_2Sn_{1-y}In_ySe_3$ compounds.

Cu_2SnSe_3.

The electronic properties of the 2.5% Ga doped sample were measured at higher temperatures, shown in Figure 5.5. The resistivity and Seebeck coefficient both increase rapidly with temperature up to the highest measurement temperature of 600K. The power factor, defined as $S^2\sigma$ (the numerator of the ZT equation), reaches 6.2 μW/cm*K^2 at this temperature. The estimated ZT value (calculated by extrapolating the low temperature thermal conductivity data) approaches 0.28 for this sample at 600K.

Controlling the carrier concentration of the doped compounds again proved to be challenging. In an attempt to reproduce the best composition, another 2.5% Ga sample was made in the same way as the one shown in Figures 5.3 and 5.4. This sample clearly contained a hole concentration gradient and had ZT values ranging from 0.008 to 0.017 at room temperature, never matching the value measured for the first sample.

All Cu_2SnSe_3 samples discussed above displayed p-type conduction. Attempts at producing

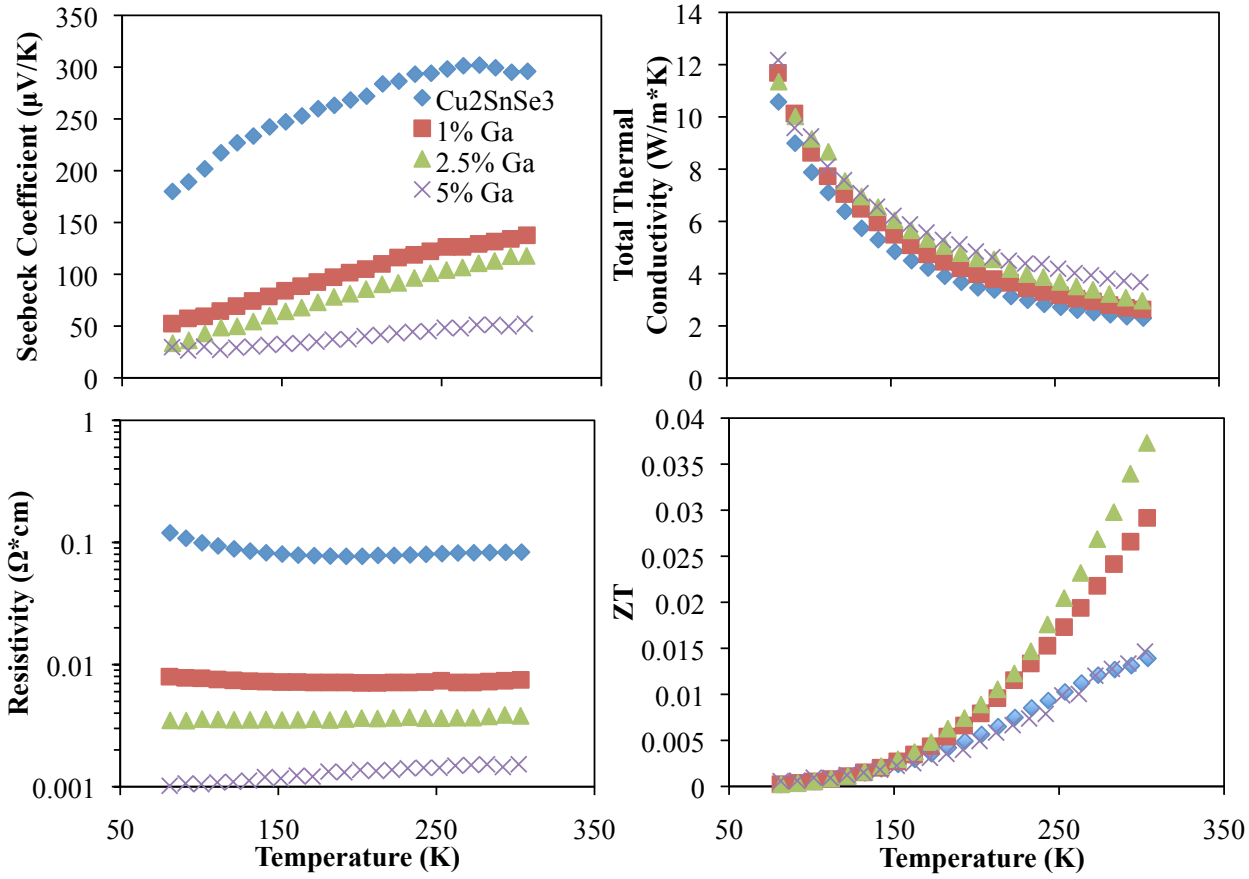

Figure 5.4: Low temperature thermoelectric properties of the $Cu_2Sn_{1-x}Ga_xSe_3$ compounds.

n-type samples were unsuccessful due primarily to the already high hole concnetration in undoped samples. Doping with Zn on the Cu site resulted in the formation of ZnSe as a secondary phase. Doping with either Sb or Bi on the Sn site did not change the sign of the conduction, although no secondary phases were detected using XRD. Adding excess Se did not systematically affect the carrier concentration. No secondary phases were detected by XRD,which was expected due to the wide phase region of Cu_2SnSe_3.

Shi *et. al.* recently reported that Cu_2SnSe_3 can achieve ZT = 1.14 at 850K when doped with 10% In [79]. This result could not be reproduced for the purposes of this work, mainly because Cu_2SnSe_3 becomes unstable near 800K. Ga and In doped samples measured at high temperature showed a dramatic increase in resistivity and Seebeck coefficient at this temperature, indicating

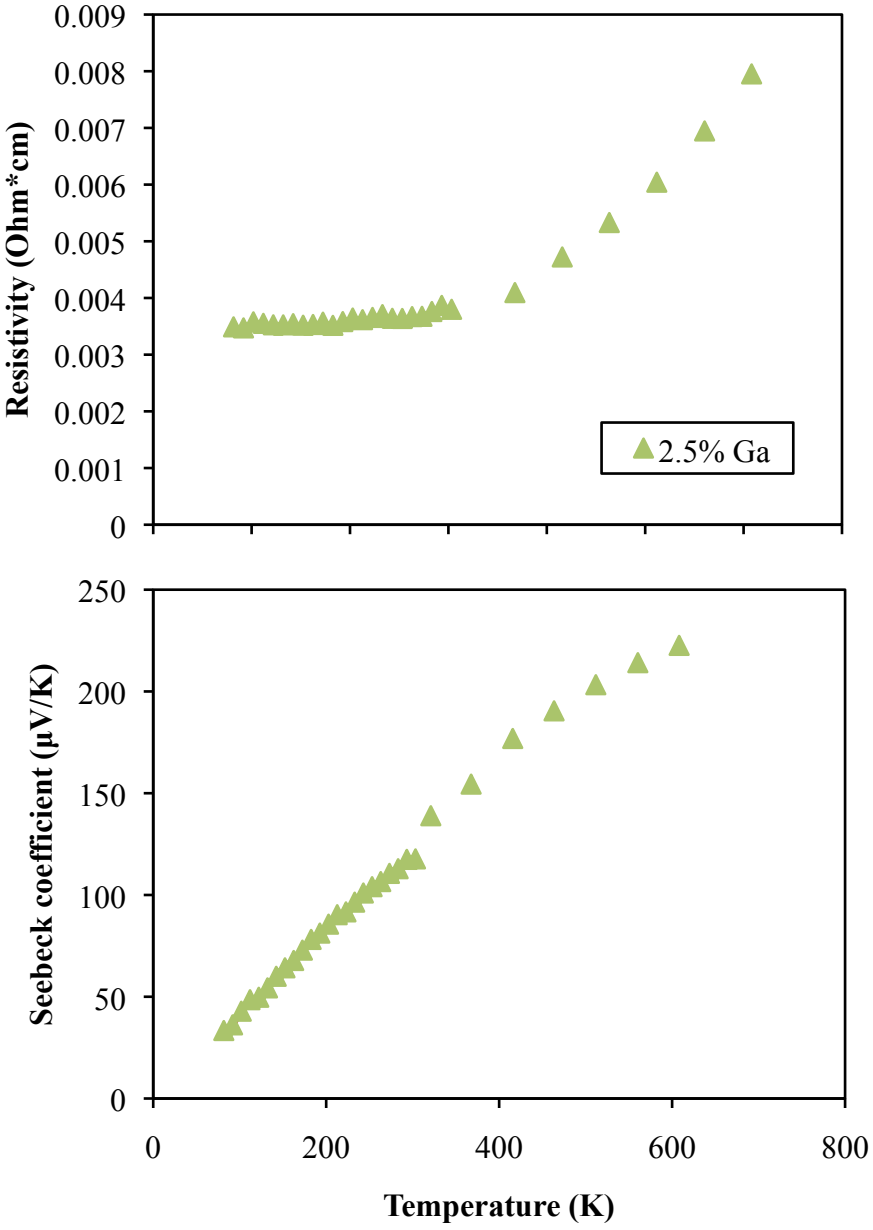

Figure 5.5: High temperature electronic properties of $Cu_2Sn_{0.975}Ga_{0.025}Se_3$.

softening of the sample (see Figure 5.14). In some cases, the samples were deformed during high temperature measurement. Shi *et. al.* coated their samples with glass before high temperature measurement, which could have provided some rigidity at high temperature. The same authors have also reported solid solutions of Cu_2SnSe_3 with ZnSe and CdSe as having ZT $>$ 1 at high temperature when appropriately doped [80], [81]. In light of these results, other solid solutions based on Cu_2SnSe_3 should be investigated for thermoelectric applications.

5.2.3 Summary

From this portion of the work it is concluded that the compound Cu_2SnSe_3 holds potential as a p-type thermoelectric material. Single phase samples can be synthesized by either quenching from 900°C into water or by slow cooling, annealing at 400°C, and slow cooling to room temperature. Samples quenched from high temperature have a cubic sphalerite structure with a disordered arrangement of Cu and Sn atoms on the cation sublattice. Slow cooling and annealing allows for ordering among the Cu and Sn atoms and results in a monoclinic crystal structure. No secondary phases were detected in any of the samples. Quenched samples proved to be extremely brittle and therefore their transport properties could not be reliably measured.

The hole concentration of undoped, slow-cooled samples shows large sample-to-sample variations, and is typically in the range of 10^{18} - 10^{20} cm^{-3}. The reason for the large variations is not known, but is likely associated with intrinsic defects or compositional variations. The hole concentration can be increased through either Ga or In doping on the Sn site, reaching 10^{21} cm^{-3} for 5% doping.

The thermoelectric properties vary systematically with doping level and are optimized for 2.5% Ga doping, which gives ZT=0.037 at room temperature. High temperature measurements yielded an estimated ZT value of 0.28 at 600K for this sample, with material stability concerns preventing measurements at higher temperature.

5.3 The Cu_2SnSe_3-Cu_2GeSe_3 Solid Solution

Averkieva *et. al.* reported that Cu_2SnSe_3 and Cu_2GeSe_3 formed a complete solid solution, yet these compounds have not been studied for thermoelectric applications. For compounds of the form $Cu_2Sn_{1-x}Ge_xSe_3$, they reported a zincblende-type structure for $x \leq 0.67$ and a tetragonal structure for $x > 0.67$, with the smallest measured thermal conductivity of 2.97 W/m*K occurring at x = 0.67 [82].

5.3.1 Experimental

$Cu_2Sn_{1-x}Ge_xSe_3$ samples with x ranging from 0 to 1 were prepared by reacting the pure elements at 900°C as described in section 3.1. The melt was then brought to room temperature either by quenching in water or by cooling at 0.3°C/min. Samples for transport property measurements were cut directly from the solidified ingots using a diamond saw.

5.3.2 Results and Discussion

Water quenched samples were found to have a disordered zincblende-like structure (space group $F\bar{4}3m$ no. 216) for $x \leq 0.7$ and an orthorhombic structure corresponding to that of Cu_2GeSe_3 for $x > 0.7$. The transistion from orthorhombic to cubic symmetry is gradual, and is manifested in the gradual appearance of double peaks near 45°and 55° 2θ (see Figure 5.6). Slow cooled samples had a monoclinic structure similar to that of Cu_2SnSe_3 (space group Cc no. 9) for $x \leq 0.5$ as evidenced by the extra low angle peaks in the XRD pattern (see Figure 5.7). For $0.5 < x < 1.0$ a gradual transition from monoclinic to orthorhombic symmetry is evident from the gradual splitting of the higher angle XRD peaks (see Figure 5.8). When $x = 1.0$, all peaks index to the orthorhombic structure of Cu_2GeSe_3 described by Parthe [69]. No secondary phases were detected using XRD in any of the samples and the decreasing lattice spacing with increasing x, calculated from the x-ray peak shift (see Figure 5.9), indicates that the smaller Ge atoms are substituting for Sn in the

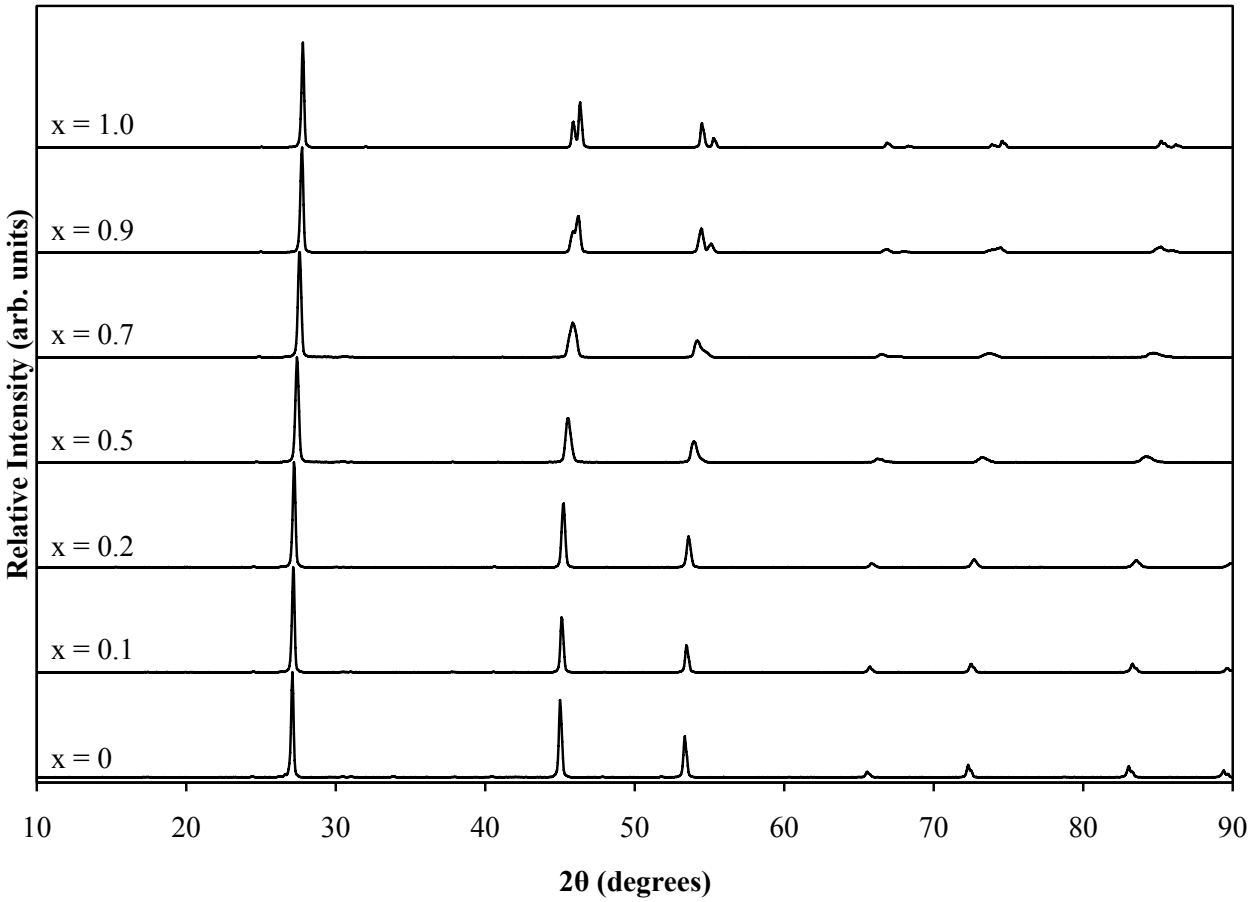

Figure 5.6: X-ray diffraction patterns of quenched $Cu_2Sn_{1-x}Ge_xSe_3$ compounds, $0 \leq x \leq 1.0$.

structure.

Transport property measurements were conducted only on the slow cooled samples since significant cracking in the quenched samples prevented reliable measurements. The electronic transport properties for the $0 \leq x \leq 0.5$ samples (Figure 5.10) show no clear x dependence, which is expected since Ge is isoelectronic to Sn. The Seebeck coefficient shows a maximum value of +210 μV/K at 300 K for x = 0.1 and 0.2, and then decreases with increasing x. The x dependence of the electrical resistivity mirrors that of the Seebeck coefficient, indicating variations in the hole concentration between samples. The measured hole concentrations were $>10^{20}$ cm^{-3} for all samples, indicating unintentional doping. Extended annealing at 400°C had no effect on the

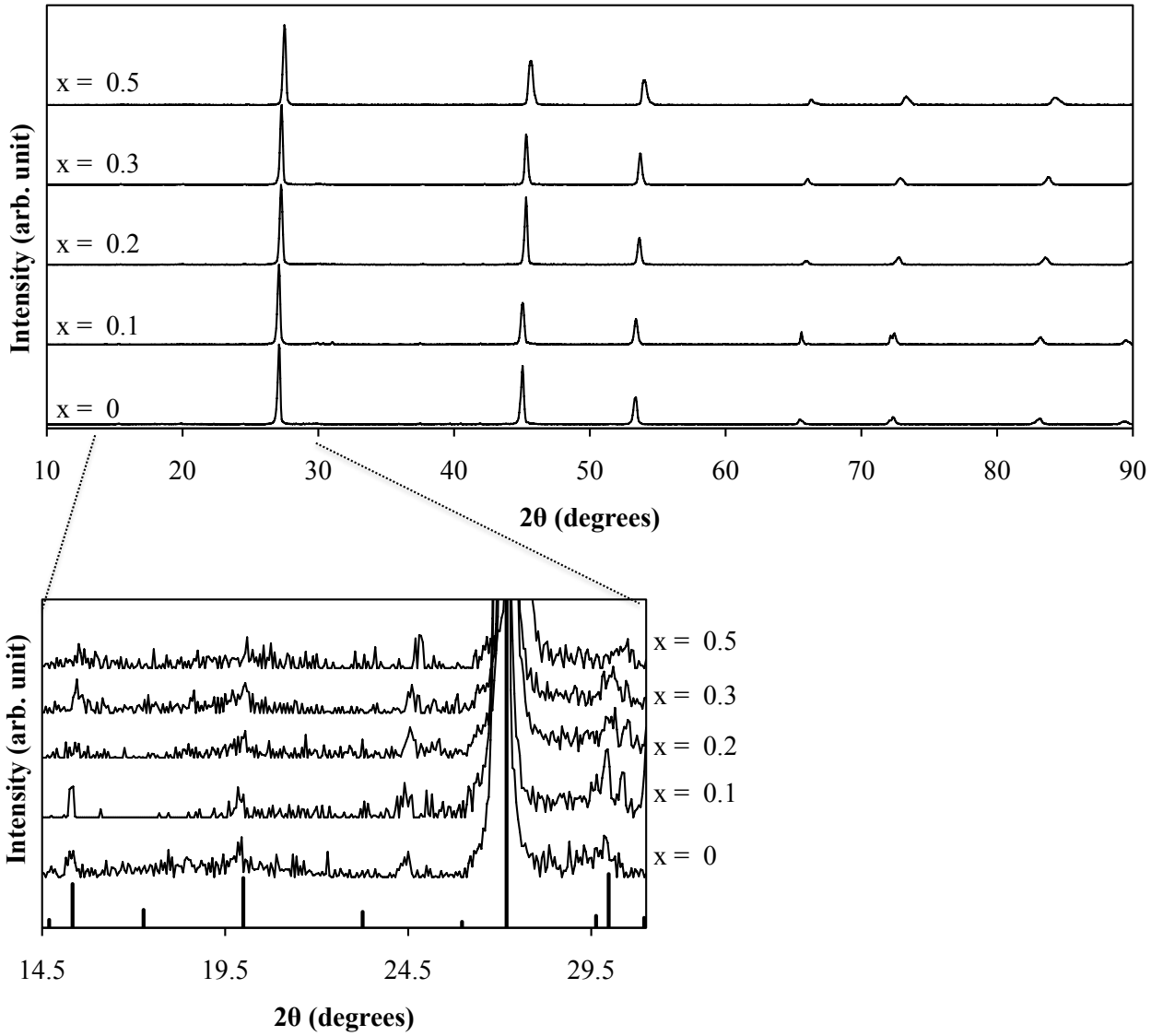

Figure 5.7: X-ray diffraction patterns of slow cooled $Cu_2Sn_{1-x}Ge_xSe_3$ compounds, $x \leq 0.5$. Lower plot shows close-up view of low angle peaks indicating monoclinic structure, vertical lines represent reported peak locations for monoclinic Cu_2SnSe_3 [65].

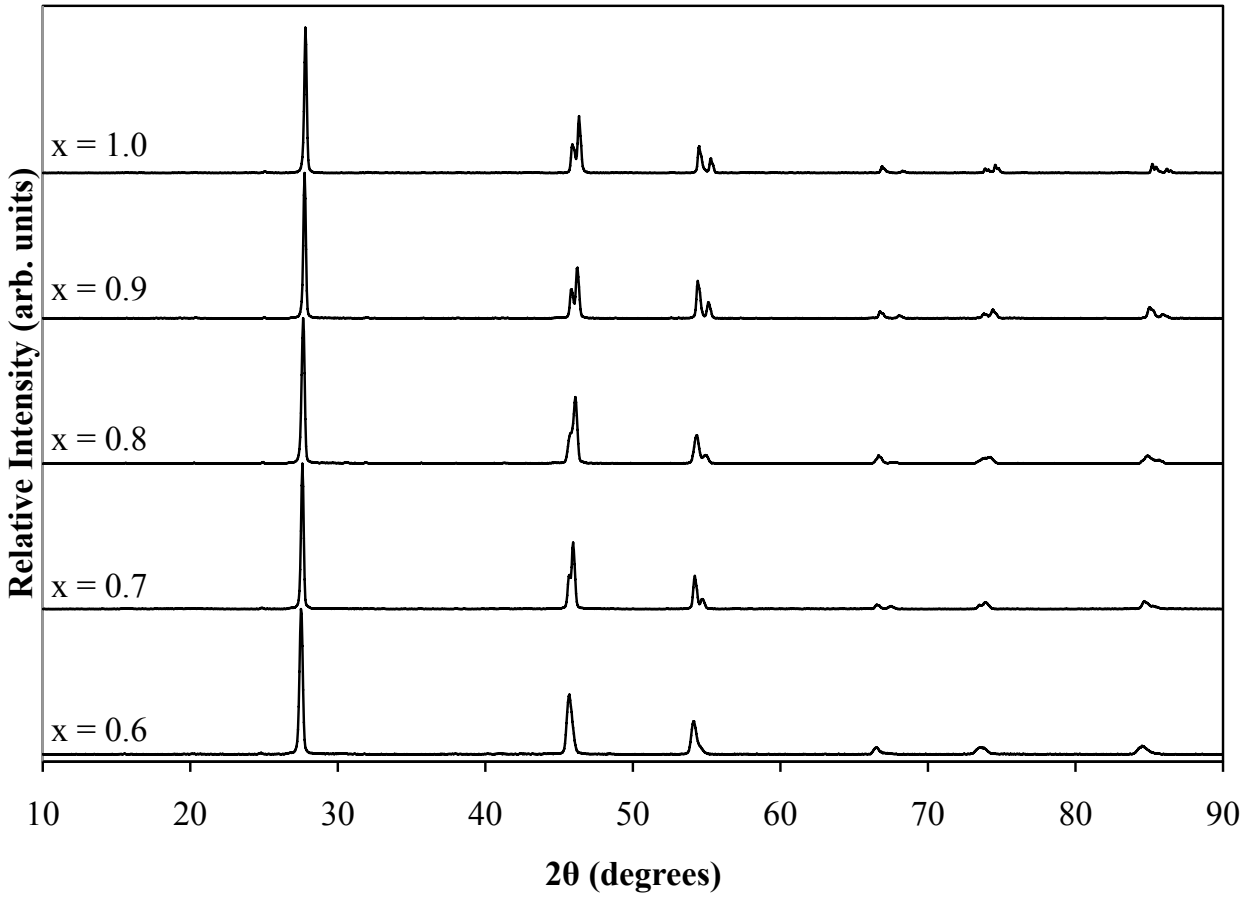

Figure 5.8: X-ray diffraction patterns of slow cooled $Cu_2Sn_{1-x}Ge_xSe_3$ compounds, $x > 0.5$.

hole concentration.

The lattice thermal conductivity of Cu_2SnSe_3 decreases upon the addition of Ge as expected due to phonon-impurity scattering. The measured thermal conductivities of the x = 0 and x = 0.5 compounds are shown in Figure 8; the values for $0 < x < 0.5$ are bounded by these two extremes. The decreasing thermal conductivity with increasing x can be understood using the Debye approximation to the lattice thermal conductivity [84]:

$$\kappa_L = \frac{k_B^4}{2\pi^2\hbar^2 v} T^3 \int_0^{\theta/T} \frac{r^4 e^r}{(e^r - 1)^2} \tau(r) dr \tag{5.2}$$

where k_B is Boltzmann's constant, v is the phonon velocity, θ is the Debye temperature, $\hbar$ is

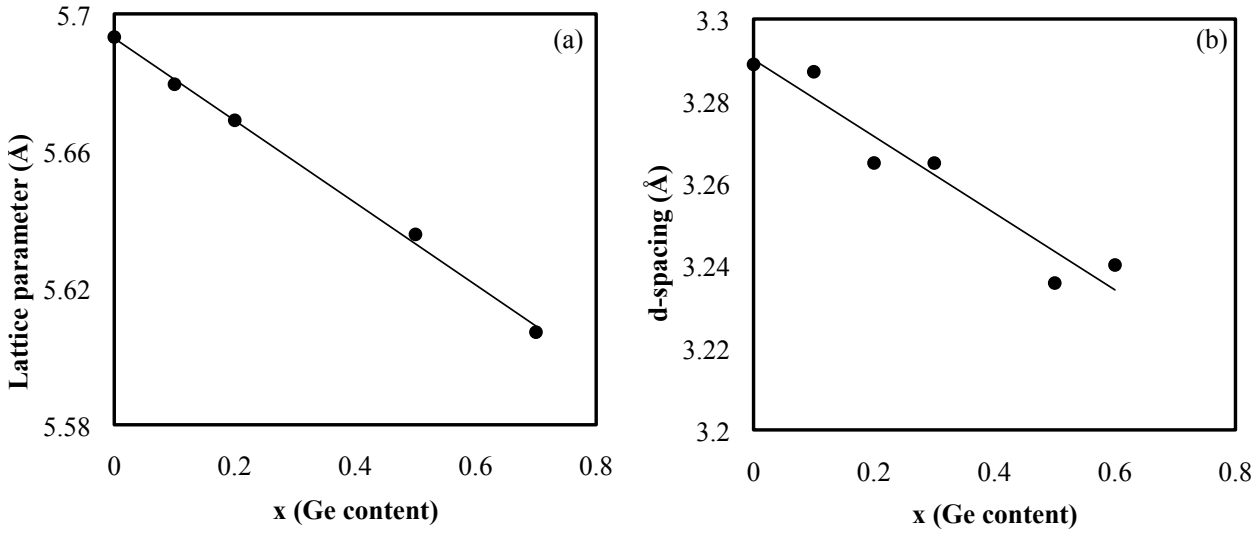

Figure 5.9: Lattice spacing of the $Cu_2Sn_{1-x}Ge_xSe_3$ compounds with Cu_2SnSe_3-type structure: (a) lattice parameter of the cubic (quenched) samples, (b) interplanar spacing of the (200) planes of the monoclinic (slow cooled) samples.

Plancks constant, and $\tau(r)$ is the phonon scattering time in terms of the dimensionless parameter r:

$$r = \frac{\hbar\,\omega}{k_B\,T} \tag{5.3}$$

where ω is the phonon frequency. Since optic phonon modes have low group velocity, the majority of heat in a crystalline material is carried by the acoustic phonon modes. Thus, the values for v, θ and $\tau(r)$ should correspond to the acoustic portion of the phonon spectrum only. Empirically determined values of v and θ for Cu_2SnSe_3 have been reported, but represent averages over all phonon modes in the crystal [85]. Slack showed that θ_a (acoustic mode Debye temperature) can be estimated from θ_0 (average Debye temperature, estimated from elastic constants or specific heat) using [45]:

$$\theta_a = \theta_0 n^{-1/3} \tag{5.4}$$

where n is the number of atoms per primitive crystallographic unit cell. This yields $\theta_a = 86.4$ K

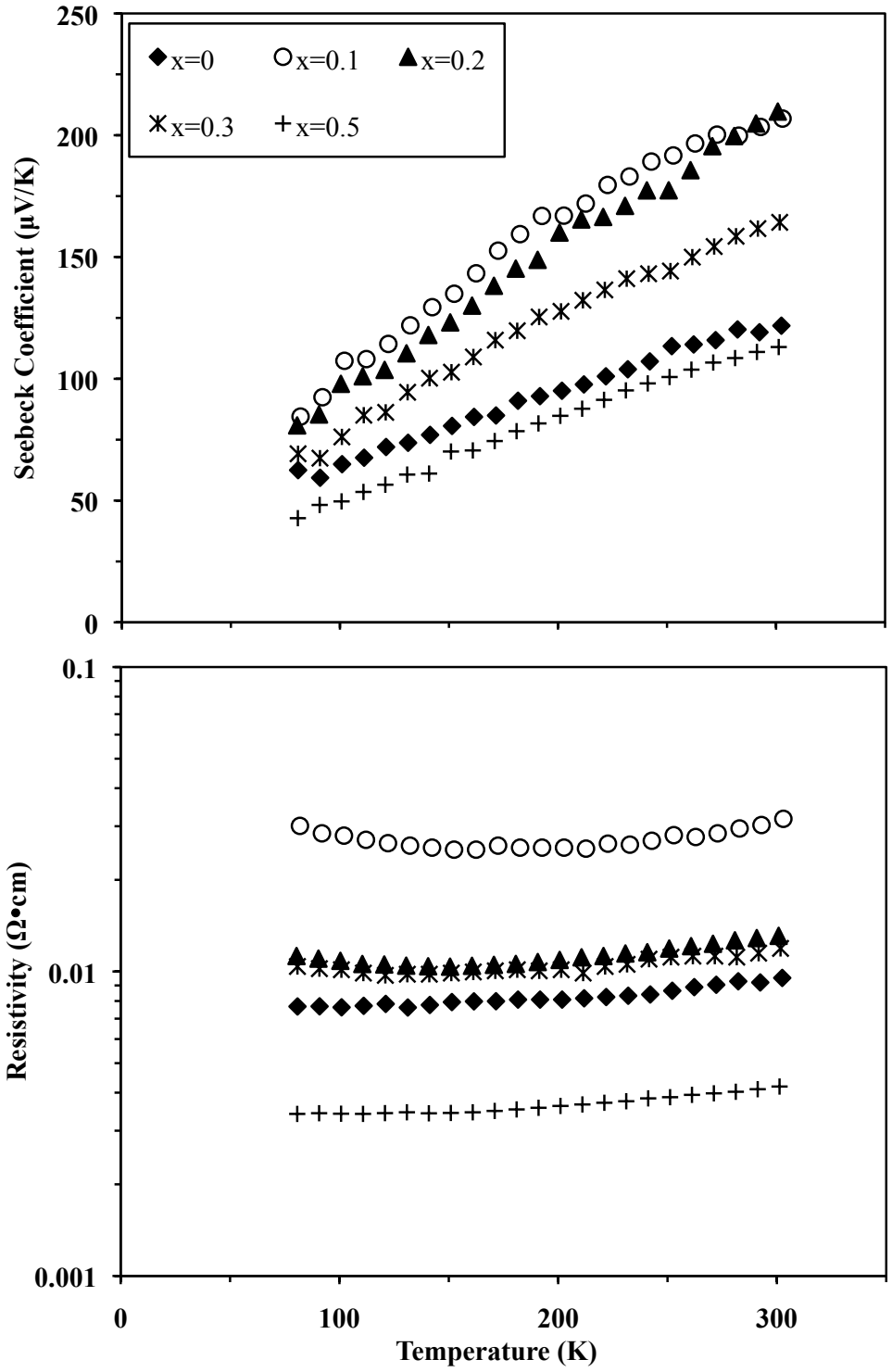

Figure 5.10: Temperature dependence of the Seebeck coefficient and electrical resistivity of the $Cu_2Sn_{1-x}Ge_xSe_3$ compounds for $x < 0.5$

for Cu_2SnSe_3, which has $n = 6$. Similarly, the acoustic mode phonon velocity can be estimated by taking the inverse cubic average of the reported longitudinal and transverse phonon velocities [86], which gives $v_a = 1664$ m/s for Cu_2SnSe_3 [85]. Assuming that the individual phonon scattering rates are additive, the total $\tau^{-1}(r)$ can be expressed as the sum of the individual scattering rates due to grain boundaries, point defects, and phonon-phonon Umklapp scattering:

$$\tau^{-1}(r) = \tau_G^{-1}(r) + \tau_P^{-1}(r) + \tau_U^{-1}(r). \tag{5.5}$$

Expressions for the individual scattering rates have been developed separately [87] - [89], and were compiled and used by Morelli *et. al.* to predict the effect of isotope scattering on the thermal conductivity of diamond-like semiconductors [90]. The same expression for the total scattering rate is used to fit the present data:

$$\tau^{-1}(r) = \frac{v_a}{L} + A(r^4)\, T^4 + B(r^2)\, T^3\, e^{-\theta_a/T} \tag{5.6}$$

where:

$$A = \frac{V k_B^4\, \Gamma}{4\pi\hbar^4 v_a^3} \tag{5.7}$$

and

$$B = \frac{\hbar\, \gamma^2}{M v_a^2 \theta_a} \tag{5.8}$$

where L is the average grain size, V is the average volume per atom, γ is the Grüneisen constant, M is the average atomic mass, and Γ is the phonon-impurity scattering parameter. The original expression for Γ derived by Klemens required knowledge of the interatomic bonding forces in the material and thus is not practical to use for new materials [88]. Abeles later developed an expression for Γ that accounts for differences in atomic mass and size between the host and impurity

atoms and only requires knowledge of the atomic masses and radii of the constituent atoms [91]. Recently Yang et. al. generalized this expression for compounds containing more than one sublattice [92]:

$$\Gamma = \Gamma_M + \Gamma_S \tag{5.9}$$

where Γ_M and Γ_S are the impurity scattering parameters for mass and strain field fluctuations respectively. For the case of $Cu_2Sn_{1-x}Ge_xSe_3$ there are two distinct atoms on the Sn sublattice, which are denoted below as A and B [92]:

$$\Gamma_M = \frac{c_S \left(\frac{\bar{M}_S}{\bar{M}}\right)^2 f^A f^B \left(\frac{M^A - M^B}{\bar{M}_S}\right)^2}{\left(\sum_{i=1}^{n} c_i\right)} \tag{5.10}$$

and

$$\Gamma_S = \frac{c_S \left(\frac{\bar{M}_S}{\bar{M}}\right)^2 f^A f^B \varepsilon_S \left(\frac{r^A - r^B}{\bar{r}_S}\right)^2}{\left(\sum_{i=1}^{n} c_i\right)} \tag{5.11}$$

where c_S, $\bar{M}_S$, and $\bar{r}_S$ are the total occupancy, average mass and average atomic radius of the sublattice. $f^{A,B}$, $M^{A,B}$ and $r^{A,B}$ are the fractional occupancies, atomic masses, and atomic radii of the A and B atoms respectively, $\bar{M}$ is the average mass of the compound, and c_i is the total occupancy of the ith sublattice. The phenomenological adjustable parameter ε_S depends on the Grúneisen parameter and the elastic constants of the material and typically ranges from 10 to 100.

Calculating Γ_M for the $Cu_2Sn_{1-x}Ge_xSe_3$ compounds is straightforward using c_S = 1, $\bar{M}_S$ = 95.64, M^{Sn} = 118.7, M^{Ge} = 72.58, Σc_i = 6, and letting $\bar{M}$ vary with composition. The maximum value of Γ_M = 0.0151 is occurs at x = 0.5, corresponding to the maximum disorder in the lattice.

The only unknown parameter in the expression for Γ_S (equation 5.11) is ε_s which, following the procedure of Abeles [91], can be estimated using:

$$\varepsilon_s = 12.3 + 39.4\gamma + 31.5\gamma^2 \tag{5.12}$$

where γ is the Grüneisen parameter. This yields ε_s = 116 for γ = 1.3, giving Γ_S = 0.142 at x = 0.5. The lattice thermal conductivity of the $Cu_2Sn_{1-x}Ge_xSe_3$ compounds can now be calculated using the following assumptions:

- The grain size does not vary substantially from sample to sample, a large grain size, L = 1 mm, is assumed for all samples such that grain size effects are essentially eliminated from the model since phonon-impurity scattering is the primary interest.

- The compositional dependence of the Debye temperature follows Lindemann's rule, $\theta = a + bT_m^{0.5}V^{-1}M^{-0.5}$, where T_m, V, and M are the melting temperature, volume per atom, and atomic mass of the compound, respectively [10].

- The phonon velocity does not vary significantly with composition, v_a = 1664 m/s is used for all calculations.

- The Grüneisen constant is treated as an adjustable parameter to fit the data of the x = 0 compound and is then held constant with composition. This procedure yields γ = 1.3, a very reasonable estimate for zincblende-type compounds [45].

The calculated lattice thermal conductivities of the x = 0 and x = 0.5 compounds are plotted in figure 5.11 along with the experimental data (the thermal conductivities of the x $<$ 0.5 compounds fall betweeen these two extremes). To obtain the fit for the x = 0.5 sample, only phonon-impurity scattering due to mass fluctuations (Γ_M) was taken into account; the parameter ε_s in equation 5.11 was set to zero, resulting in Γ_S = 0. This is in stark contrast to ε_s = 116 given by equation 5.12

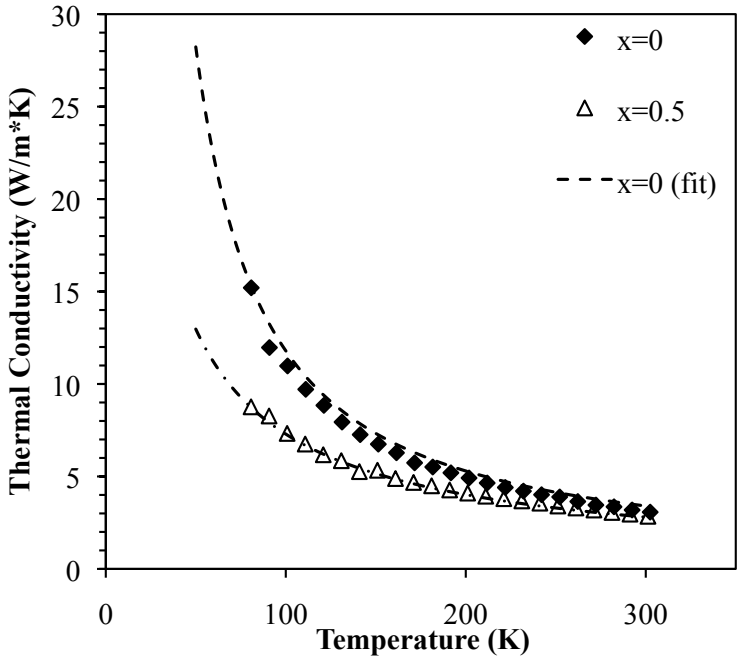

Figure 5.11: Temperature dependence of the thermal conductivity of the $Cu_2Sn_{1-x}Ge_xSe_3$ compounds for x = 0 and 0.5. Dotted lines represent lattice thermal conductivity calculated from the Debye model (equation 5.2).

with $\gamma = 1.3$ but, as Abeles pointed out [91], the ε_s parameter should be treated as adjustable. The fact that $\varepsilon_s = 0$ reveals that the substitution of Ge for Sn in Cu_2SnSe_3 causes phonon scattering primarily due to the atomic mass difference between Ge and Sn and results in little strain-field fluctuation in the lattice. This is in agreement with the XRD patterns for these compounds (Figures 5.7 and 5.8) which show very little peak broadening for the intermediate compositions, indicating little microstrain in the lattice [93].

The x = 0.2 sample showed the best thermoelectric properties, with ZT = 0.035 at room temperature. Doping the $Cu_2Sn_{1-x}Ge_xSe_3$ compounds with Ga or In on the Sn/Ge site were largely unsuccessful due to the already large hole concentrations of the undoped compounds. The results (not shown) indicate that Ga and In can substitute on the Sn/Ge site, but do not improve the thermoelectric properties.

5.3.3 Summary

The above results confirm the existence of a complete solid solution in the Cu_2SnSe_3-Cu_2GeSe_3 system. $Cu_2Sn_{1-x}Ge_xSe_3$ samples cooled slowly from 900°C show a transition from the monoclinic Cu_2SnSe_3 structure to the orthorhombic Cu_2GeSe_3 structure at x = 0.5 as indicated by XRD peak splitting for samples with $x > 0.5$. The high temperature cubic Cu_2SnSe_3 phase was prevalent in samples with $x \leq 0.7$ that were quenched from 900°C, but these samples proved to be too brittle for transport property measurements.

The lattice thermal conductivity of the slow-cooled $Cu_2Sn_{1-x}Ge_xSe_3$ compounds can be understood using the Debye model with the correct choice of phonon scattering rates. Allowing only the point defect scattering rate to change with composition, an excellent fit to the experimental data of the x = 0 and 0.5 samples was produced. An analysis of the phonon-impurity scattering parameter Γ revealed that phonons are scattered primarily due to the atomic mass difference between Ge and Sn rather than lattice strain introduced from the difference in their atomic radii. The absence of significant lattice strain is confirmed by the lack of peak broadening in the XRD patterns, and may be an artifact of the gradual change from monoclinic to orthorhombic symmetry that occurs in these compounds.

Optimization of the thermoelectric properties of the $Cu_2Sn_{1-x}Ge_xSe_3$ compounds was frustrated by large ($>10^{20}$ cm^{-3}) hole concentrations in the undoped material. Doping with Ga or In on the Sn/Ge site failed to improve the modest ZT values achieved for the nominally undoped compounds.

5.4 The Cu_2SnSe_3-Cu_2SnS_3 Solid Solution

The compound Cu_2SnS_3 exists in both high-temperature cubic (disordered) and low-temperature monoclinic (ordered) variations, analogous to Cu_2SnSe_3. Irie reported a complete solid solution for Cu_2SnSe_3-Cu_2SnS_3 [68], with a 37% reduction in κ_L occurring near the 50% composition. The thermoelectric properties of this system have not been reported and are evaluated here as a means of improving upon those of Cu_2SnSe_3 and potentially stabilizing the compound at high temperatures.

5.4.1 Experimental

Samples of $Cu_2SnSe_{3-x}S_x$ ($0 \leq x \leq 1.5$) were prepared by slow cooling the melt (24°C/hour) from 900°C to 500°C, annealing for 4 days, and slow cooling to room temperature. The resulting ingots were vibratory ball milled for 30 minutes and hot pressed at 500°C for 30 minutes at a pressure of 70 MPa, giving pellets with >94% of the theoretical density. Samples for transport property measurements were cut directly from the hot pressed pellets.

5.4.2 Results and Discussion

The X-ray diffraction patterns of selected $Cu_2SnSe_{3-x}S_x$ compounds are shown in Figure 5.12. The low-temperature monoclinic structure is maintained at all compositions studied, as indicated by the extra low angle peaks in the X-ray patterns. The X-ray peaks shift to lower 2θ values with increasing x indicating a contraction of the lattice, which is expected due to the smaller size of S relative to Se. No secondary phases were detected in any of the compounds using X-ray diffraction or EDS (not shown).

The temperature dependence of κ_L of the samples shown in Figure 5.12 is plotted in Figure 5.13 (electronic contribution is negligible in the undoped compounds). The magnitude of κ_L decreases dramatically with increasing S content, and is reduced by as much as 70% at 80K and 40%

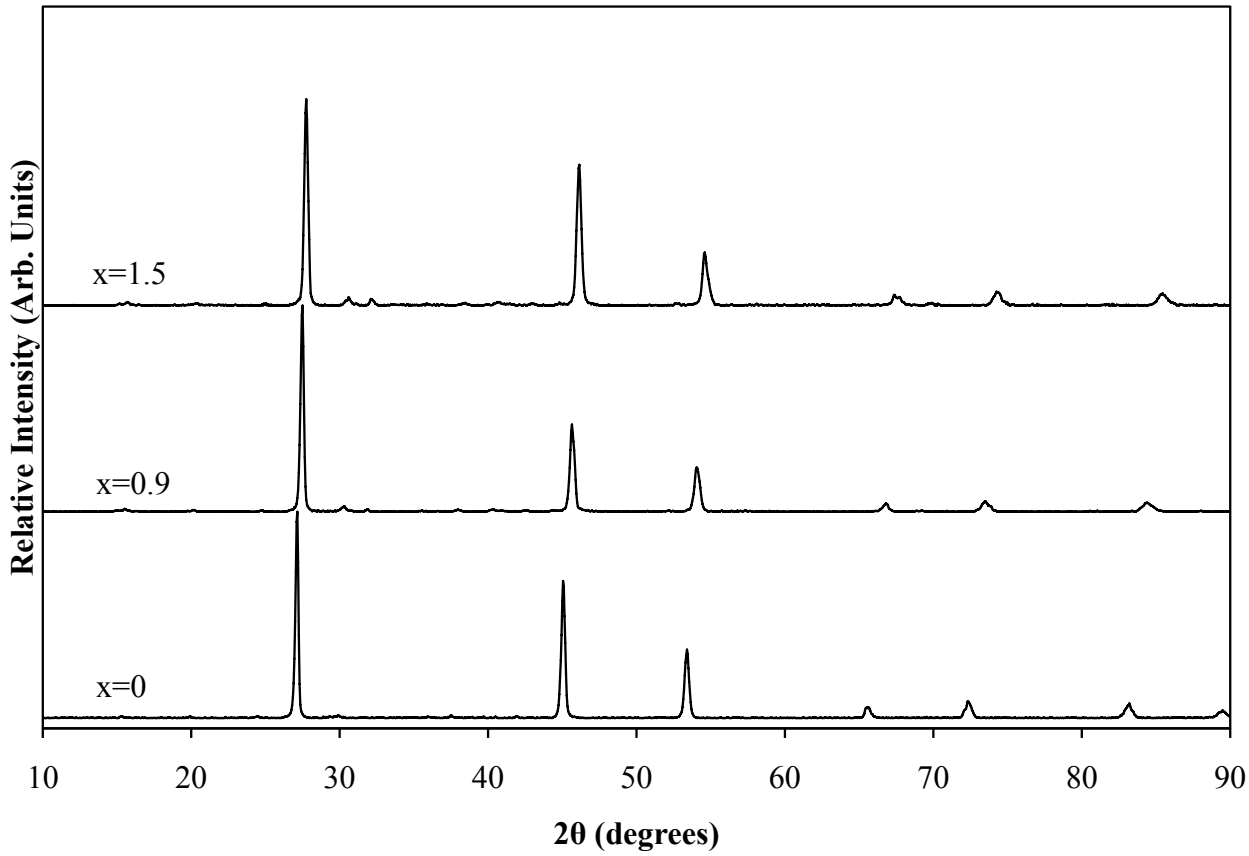

Figure 5.12: X-ray diffraction patterns of the $Cu_2SnSe_{3-x}S_x$ compounds.

at 300K. It is counterintuitive that the x=0.9 sample has a lower κ_L than the x=1.5 sample since the maximum disorder should be achieved at x=1.5, but the minimum in κ_L is not always achieved at the 50% composition for a given solid solution. The difference in κ_L between the end compounds (Cu_2SnSe_3 and Cu_2SnS_3 in this case) can cause the compositional dependence of κ_L to become skewed, causing the minimum in κ_L to occur outside of the 50% composition.

The x=0.9 composition was chosen for doping studies since it has the lowest κ_L. Both Ga and In were found to be effective p-type dopant species when substituted for Sn. The problem of sample to sample variations in hole concentration again plagued repeatability in these samples, with lengthy annealing and minor changes in composition unable to produce consistent results. The high temperature thermoelectric properties of the best-performing sample, $Cu_2Sn_{0.925}In_{0.075}Se_{2.1}S_{0.9}$,

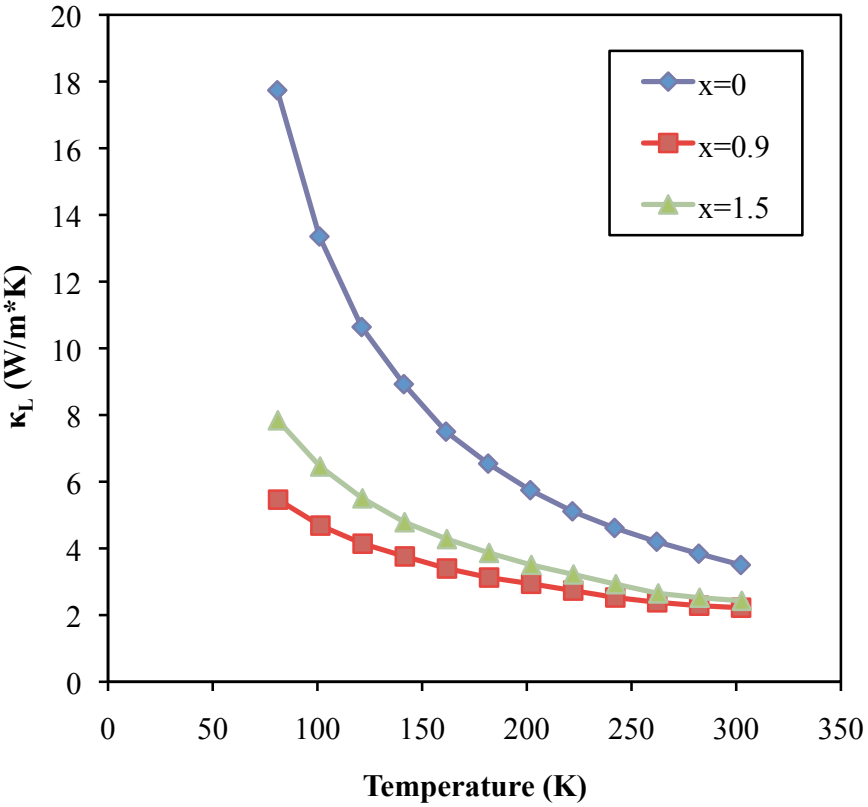

Figure 5.13: Lattice thermal conductivity of the $Cu_2SnSe_{3-x}S_x$ compounds.

are shown in Figure 5.14. The ZT reaches 0.62 at 760K, at which point the sample softened, causing an abrupt increase in the resistivity. There is no evidence in the available phase diagrams for Cu_2SnSe_3 of a decomposition near 800K.

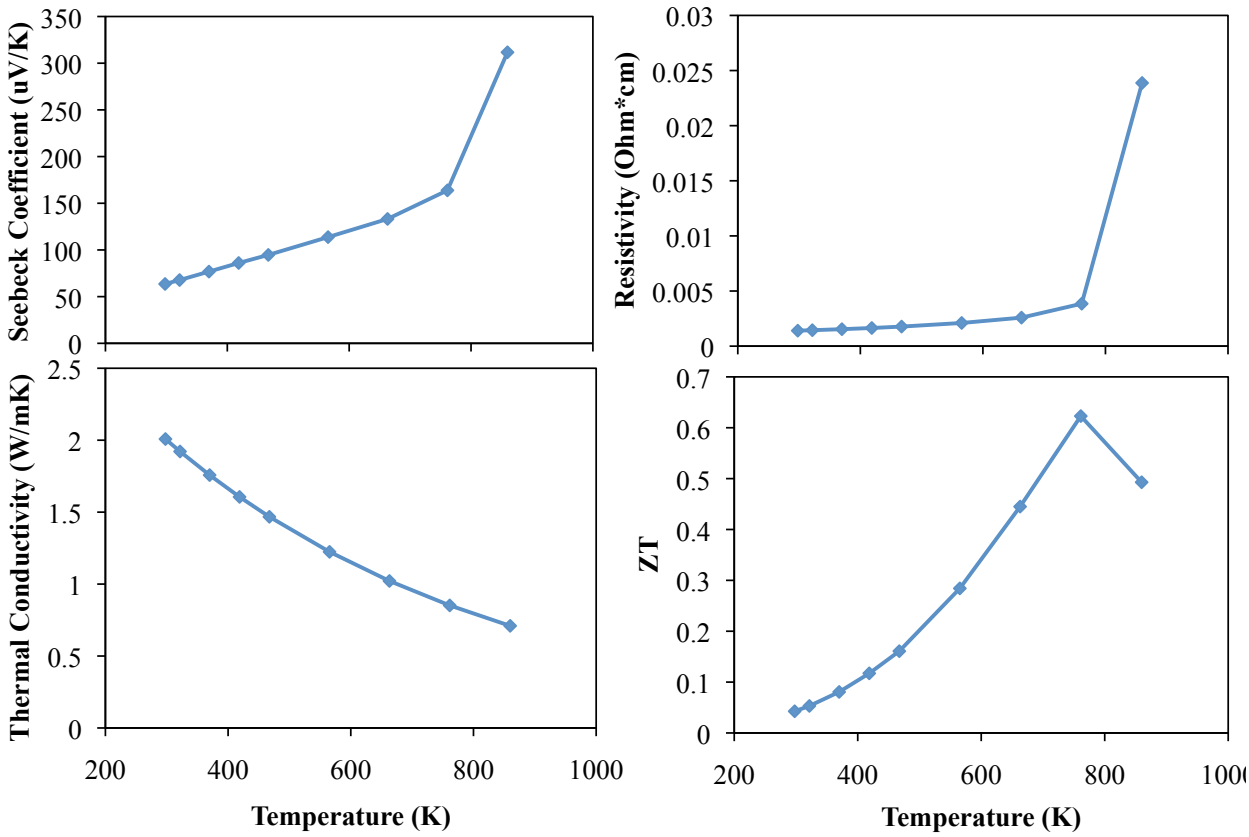

Figure 5.14: High temperature thermoelectric properties of $Cu_2Sn_{0.925}In_{0.075}Se_{2.1}S_{0.9}$

5.4.3 Summary

From this portion of the work it is concluded that S for Se substitution is a viable way to improve the thermoelectric performance of Cu_2SnSe_3. The lattice thermal conductivity is decreased by 70% at 80K and 40% at 300K when 30% S is added. Both Ga and In are effective p-type dopants in the $Cu_2SnSe_{3-x}S_x$ compounds, although reproducibly controlling the hole concentration is still an issue. Sample-to-sample variations in the hole concentration were always present independent of the synthesis procedure or doping level, which indicates that intrinsic defects play a major role in determining the hole concentration.

The optimum thermoelectric performance was obtained for the $Cu_2Sn_{0.925}In_{0.075}Se_{2.1}S_{0.9}$ compound, which reaches ZT=0.62 at 760K. Above this temperature the material undergoes soft-

ening which limits the viable operating temperature range for these compounds. Despite the reproducibility and softening problems, the relatively large ZT value obtained for these compounds warrants further exploration. Electronic band structure and defect thermodynamics calculations could provide insight as to an appropriate method of controlling the hole concentration. An investigation of the mechanical properties of these compounds would allow for a better understanding of the softening that occurs near 800K.

5.5 Off-Stoichiometric Cu_2GeSe_3 Compounds

The stoiciometric compound Cu_2GeSe_3 has been studied to some extent for thermoelectric applications, but there is a wide range of compounds with similar compositions that have remain unexplored. It has been reported that Cu_2GeSe_3 can accommodate both a deficiency and an excess of Ge, and the evolution of the physical properties with composition has not been reported.

5.5.1 Experimental

Samples with composition $Cu_2Ge_{1+x}Se_3$ (x ranging from -0.15 to 2) were prepared according to the procedure outlined in Section 3.1. Samples were cooled either by quenching the melt from 900°C into water or by slow-cooling from 900°C to room temperature at 0.4°C/min. SEM analysis was performed at the MSU center for advanced microscopy. Samples for transport property measurements were cut directly from the solidified ingots.

5.5.2 Results and Discussion

The orthorhombic crystal structure of Cu_2GeSe_3 reported by Parthe [69] was prevalent for both slow cooled and quenched x = 0 samples, as shown in Figures 5.6 and 5.8, indicating that ordering among the Cu and Ge atoms is preferred over a disordered structure which would have a higher symmetry unit cell (likely cubic as for quenched Cu_2SnSe_3). Early reports of cubic Cu_2GeSe_3 may have been erroneous due to inaccuracy of the older XRD techniques employed, or a cubic Cu_2GeSe_3 phase may be possible if very fast cooling rates are achieved. All Cu_2GeSe_3 samples were p-type with degenerate hole concentrations on the order of 10^{20} cm^{-3} over the temperature range studied. Initial results indicated that doping with Ga or In on the Ge site successfully increased the hole concentration, however the largest room temperature ZT value of 0.016 was obtained for the undoped compound.

The primary interest here is the Cu_2GeSe_3 compounds of off stoichiometric composition, some

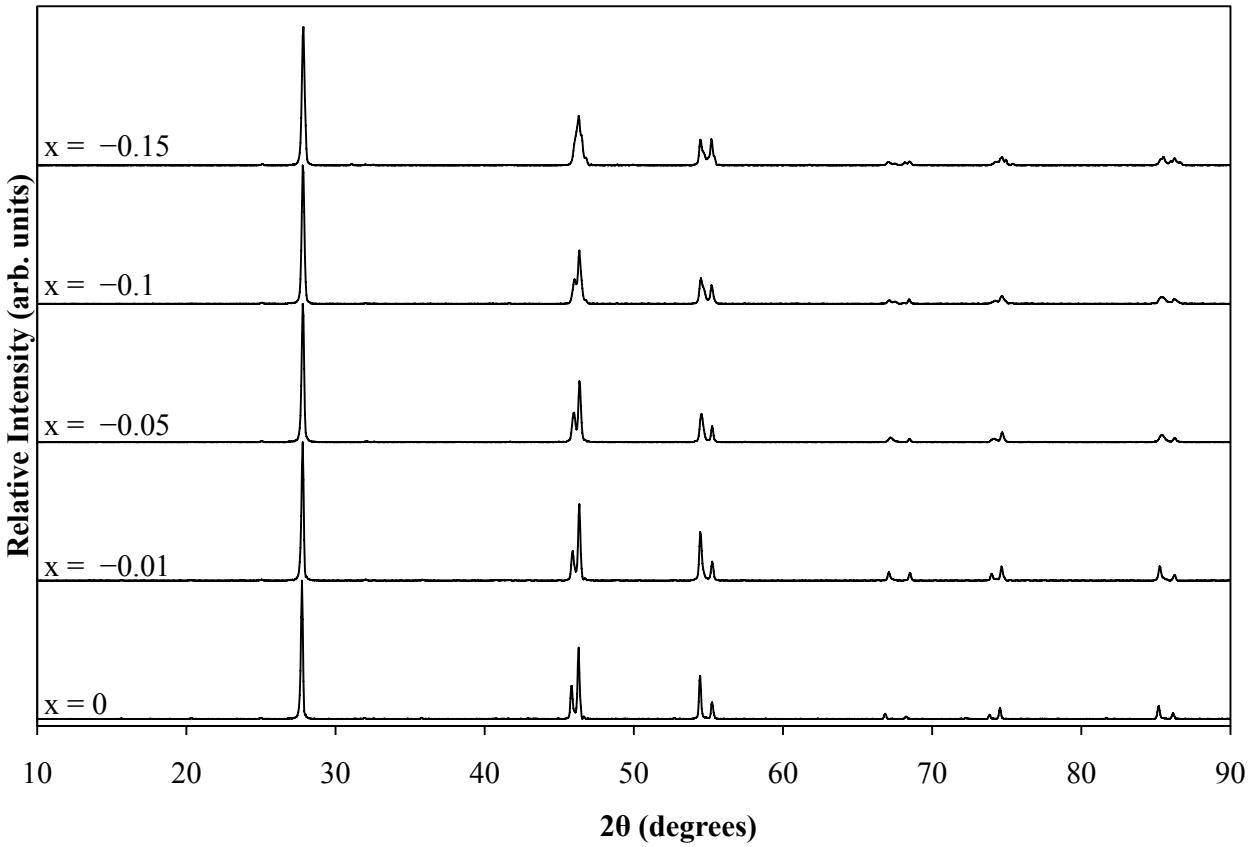

Figure 5.15: XRD patterns for slow cooled $Cu_2Ge_{1+x}Se_3$ compounds with negative values of x.

of which have reportedly low thermal conductivity [46]. Compounds deficient in Ge (negative values of x) were reported by Sharma [70] as having a monoclinic crystal structure associated with the terminal compound $Cu_2Ge_{0.85}Se_3$. The XRD patterns for samples with negative values of x (Figure 5.15) show a gradual transition from orthorhombic (x = 0) to monoclinic (x = -0.15) symmetry, as evidenced by the gradual change in the peaks near 45°and 55° 2θ. All of the peak locations for the x = -0.15 sample matched with those reported by Sharma and no impurity phases were detected in any of the samples [70].

The thermoelectric properties of the Ge deficient compounds are shown in Figure 5.16. The electrical resistivity and Seebeck coefficient decrease rapidly with decreasing x, indicating that the Ge deficiency has a strong doping effect on Cu_2GeSe_3. The change in x did not change the

sign of the carriers and all samples displayed p-type conduction. The x = -0.1 and -0.15 samples show essentially metallic character, indicated by their low and temperature independent Seebeck coefficients. There is a substantial electronic contribution to the thermal conductivity for the x $<$ 0 compounds, which comprises 29% of the total at room temperature for the x = -0.15 sample as calculated from the Wiedemann-Franz law using $L_0 = 2.45\times10^{-8}$ WΩK^{-2}. The lattice thermal conductivity (lower right, Figure 5.16) decreases with decreasing x at low temperature, which could be due to phonon scattering at vacancies created from the decreasing Ge content. The x = -0.01 sample has the largest ZT value, but it reaches only 0.011 at room temperature.

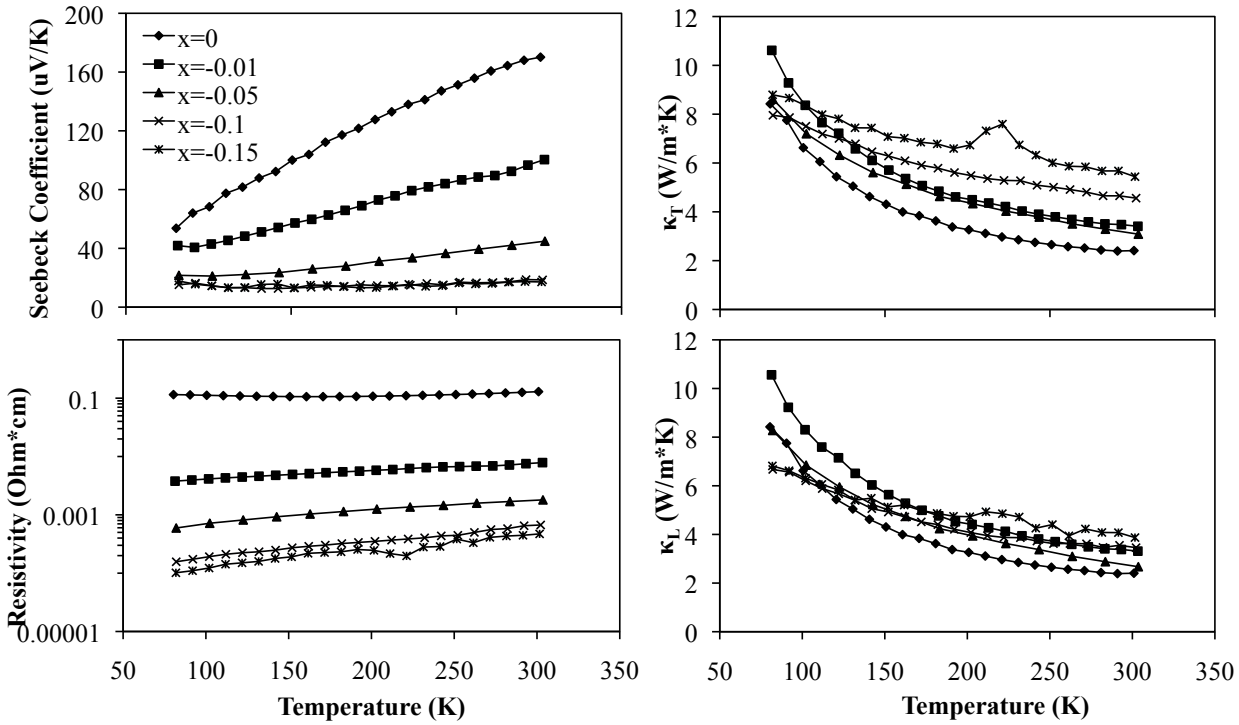

Figure 5.16: Temperature dependence of the electrical resistivity, Seebeck coefficient, and thermal conductivity for slow cooled $Cu_2Ge_{1+x}Se_3$ compounds with negative values of x.

The change in crystal symmetry for positive values of x was found to be considerably more complex than the gradual distortion observed for negative x values. Due to the wide range of compositions studied the results are split into two groups, x$\leq$ 0.55 and x$\geq$ 0.55, based on previ-

ous results that indicate the solubility limit of Ge in Cu_2GeSe_3 is x=0.55 [70]. The x-ray pattern changes significantly when excess Ge is initially added (Figure 5.17), and the double peaks indicative of the Cu_2GeSe_3 structure are nearly gone at x = 0.4. When x = 0.55, only peaks corresponding to the cubic $Cu_2Ge_{1.55}Se_3$ structure remain. The evolution of the x-ray patterns suggest that the intermediate compositions, $0 < x < 0.55$, are mixtures of the two end compounds Cu_2GeSe_3 and $Cu_2Ge_{1.55}Se_3$. The x-dependence of the thermal conductivity (Figure 5.18) highlights the transition between these two compounds, which occurs between x = 0.4 and x = 0.5, resulting in a 50% reduction in thermal conductivity at 80K. The electronic transport properties show no clear x dependence, indicating that the addition of excess Ge has no doping effect on Cu_2GeSe_3.

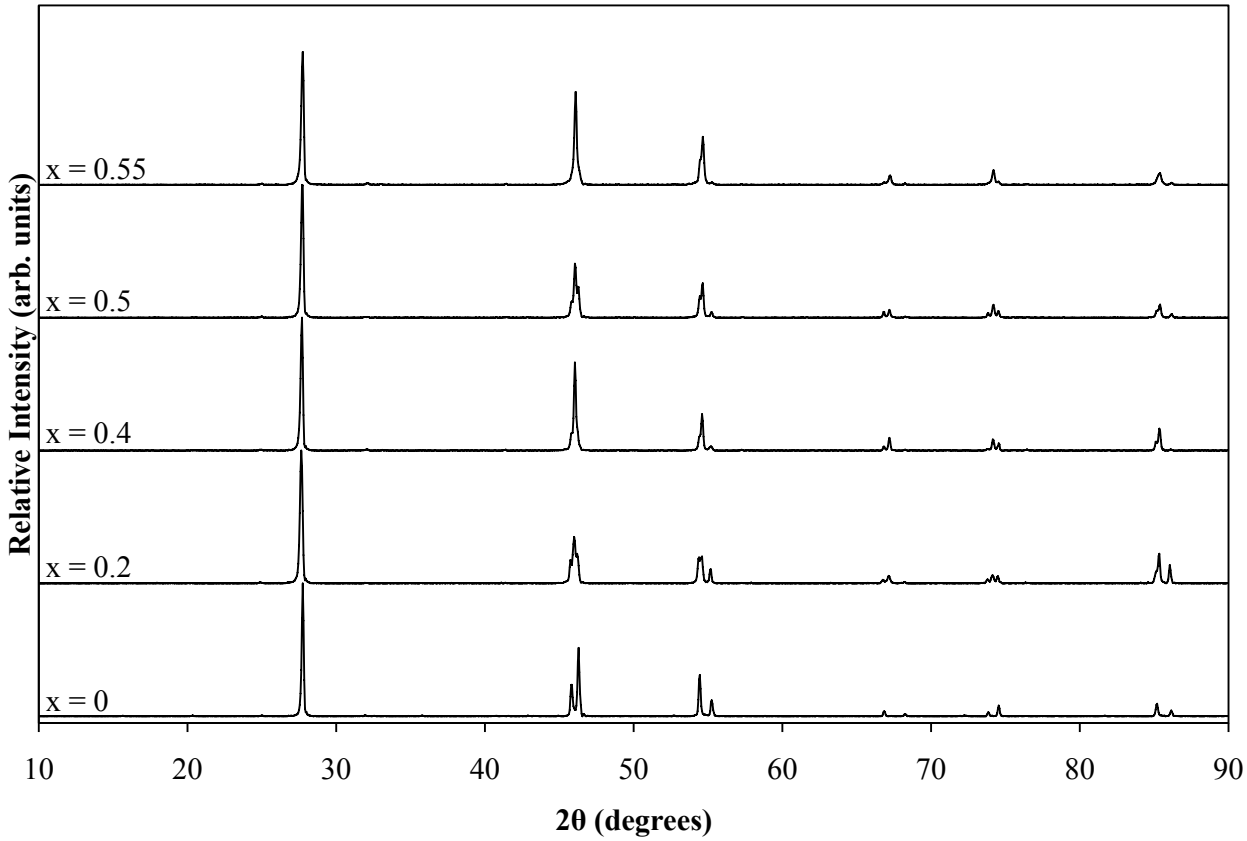

Figure 5.17: XRD patterns for the $Cu_2Ge_{1+x}Se_3$ compounds with $0 \leq x \leq 0.55$.

The x-ray diffraction patterns for the $x \geq 0.55$ samples (Figure 5.19) suggest that a single phase

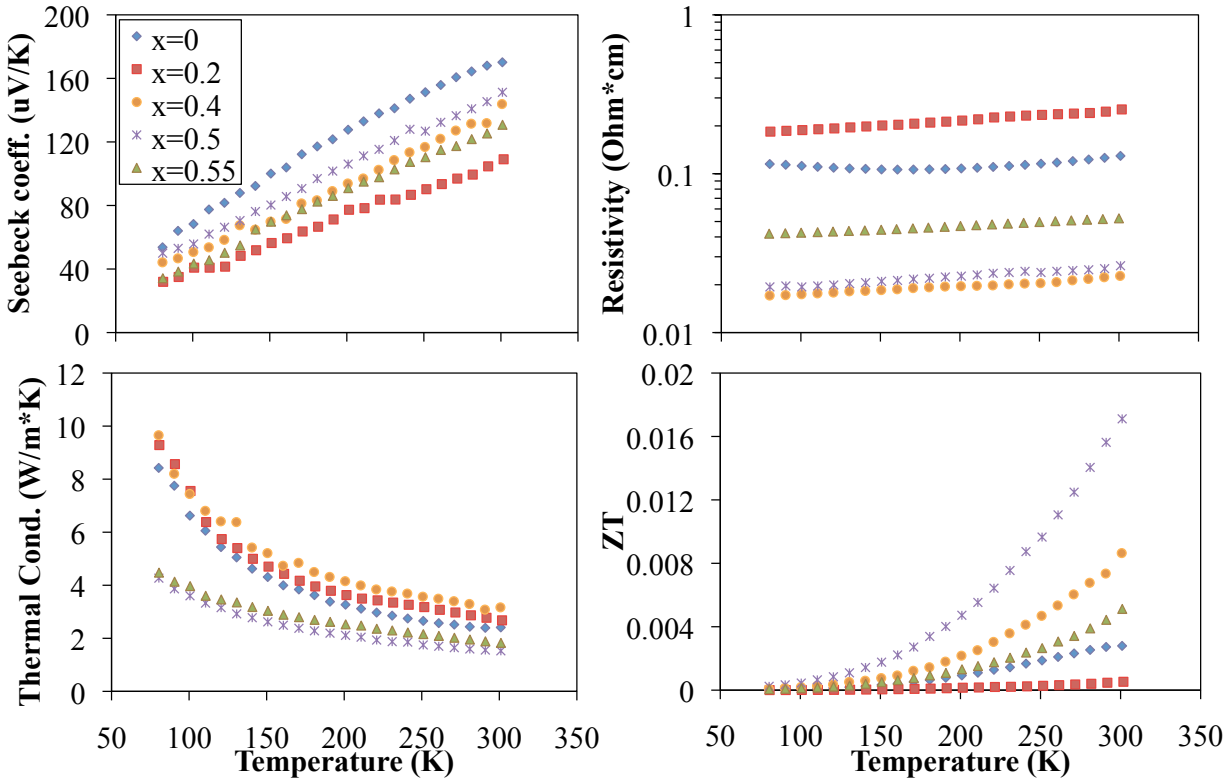

Figure 5.18: Temperature dependence of the thermoelectric properties of the $Cu_2Ge_{1+x}Se_3$ compounds with $0 \leq x \leq 0.55$.

cubic (zincblende) structure is maintained for $0.55 \leq x \leq 1.0$. For all samples with $x > 1.0$ (not shown), elemental Ge was present as a secondary phase. The Seebeck coefficient increases with increasing x but the resistivity shows no obvious x dependence, indicating that excess Ge does not have a doping effect in $Cu_2Ge_{1.55}Se_3$ (Figure 5.20). The thermal conductivity again shows a transition, in this case a 40% reduction is realized at 80K between the x=0.6 and 0.8 samples (lower left, Figure 5.20). The results from a water quenched x=1.0 sample (denoted x = 1.0Q) are also shown in Figures 5.19 and 5.20. The peaks shift to lower 2θ values, indicating an increase in the lattice constant, and the thermal conductivity is the lowest observed for any of the $Cu_2Ge_{1+x}Se_3$ compounds. It is likely that more Ge is incorporated into the lattice of the quenched sample (similar to the case of the Cu_2SnSe_3-Cu_2GeSe_3 solid solution).

Since $Cu_2Ge_{1.55}Se_3$ (a = 5.569 Å) and elemental Ge (a = 5.66 Å) have the same crystal struc-

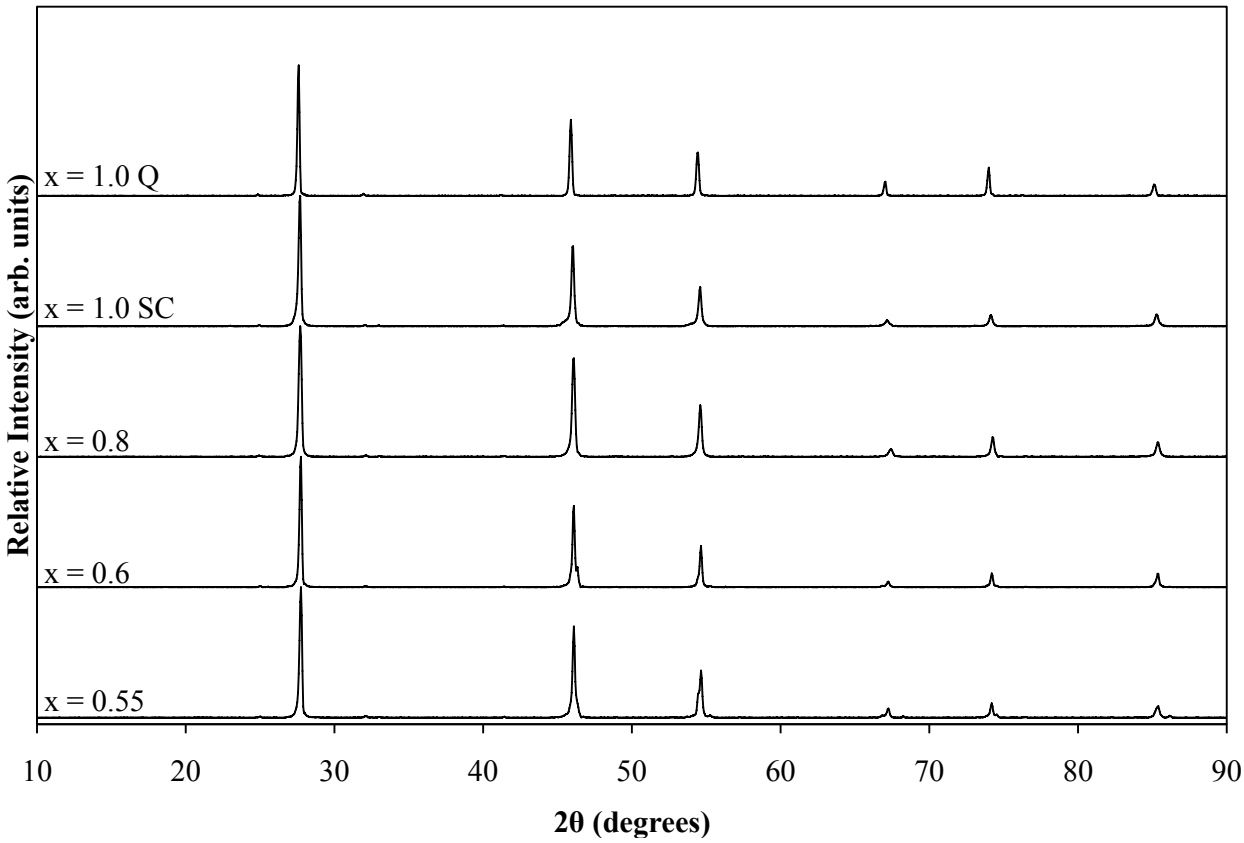

Figure 5.19: XRD patterns for the $Cu_2Ge_{1+x}Se_3$ compounds with $0.55 \leq x \leq 1.0$, "SC" and "Q" labels indicate slow cooled and quenched samples respectively.

ture and similar lattice constants, the possibility of a solid solution between these two materials should be considered. Assuming that excess Ge will occupy the Cu, Ge, and Se sites with equal probability, the solid solution takes the form $(Cu_2Ge_{1.55}Se_3)_{1-y}Ge_y$, or $Cu_{2-2y}Ge_{1.55-0.55y}Se_{3-3y}$. Using this notation, the y = 0.5 composition would correspond to the compound $Cu_2Ge_{2.55}Se_3$, which according to the present results does not exist, and the y = 0.3 composition corresponds to the compound $Cu_2Ge_2Se_3$ (data shown in Figures 5.19 and 5.20). The data extracted from Figures 5.19 and 5.20 for the $Cu_2Ge_{1+x}Se_3$ compounds are in excellent agreement with what one would expect for the $Cu_2Ge_{1.55}Se_3$-Ge solid solution. Figure 5.21 shows the calculated lattice constants and measured thermal conductivities (at 80K) versus Ge content (in terms of y) for the compounds studied here. The lattice constants show a nearly linear relationship with Ge content (as predicted

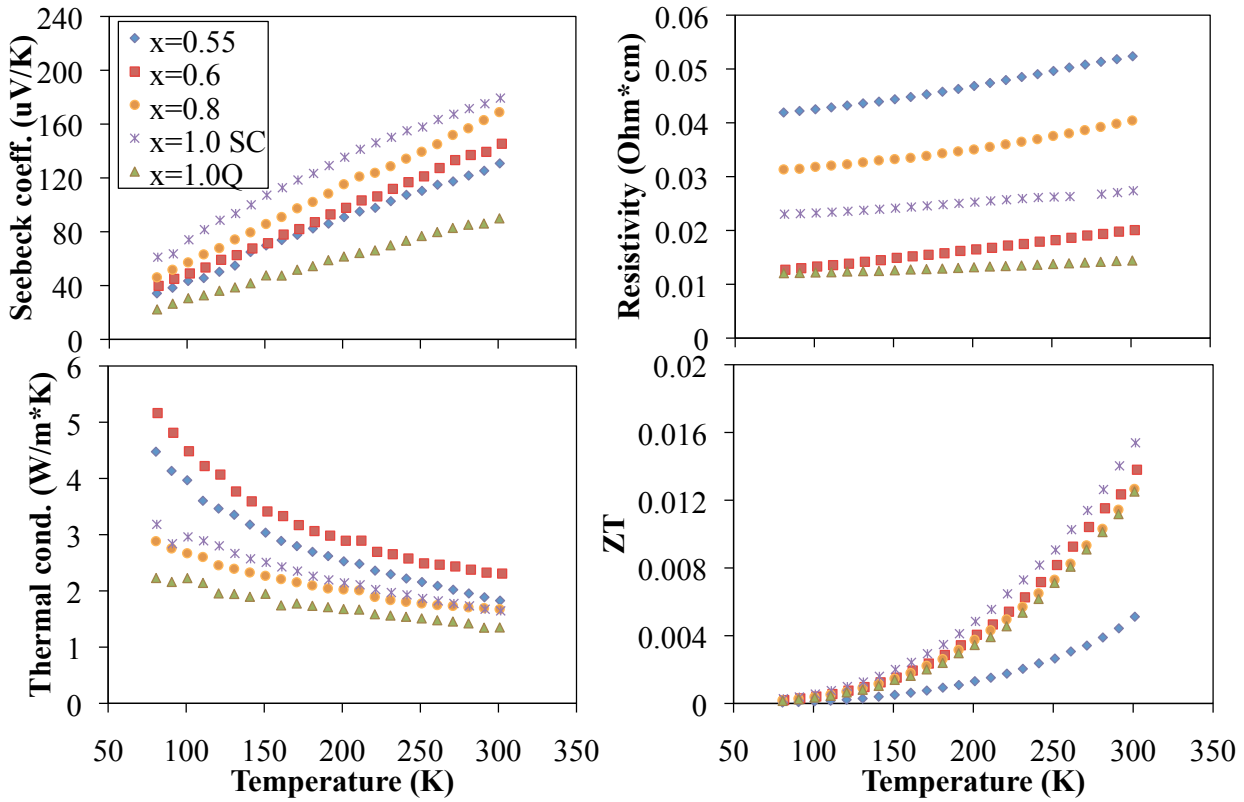

Figure 5.20: Temperature dependence of the thermoelectric properties of the $Cu_2Ge_{1+x}Se_3$ compounds with $0.55 \leq x \leq 1.0$, "SC" and "Q" labels indicate slow cooled and quenched samples respectively.

by Vegard's law) and the thermal conductivity decreases with increasing Ge content, as we would expect for compositions below 50%. These results are the first experimental evidence that the $Cu_2Ge_{1+x}Se_3$ ($x \geq 0.55$) compounds are a solid solution between $Cu_2Ge_{1.55}Se_3$ and elemental Ge, as originally proposed by Sharma and Singh [70].

SEM and EDS were completed on the excess Ge samples (positive x values) to determine the effect of Ge on the microstructure of $Cu_2Ge_{1+x}Se_3$ and evaluate the possibility of a Cu_2GeSe_3-Ge solid solution. It was found that all samples with $x>0$ contained small inclusions of a Ge-rich phase (essentially pure Ge as determined by EDS) as shown in Figure 5.22. The Ge inclusions are discontinuous, typically measuring tens of microns in diameter, and comprise only a small fraction ($<10\%$) of the microstructure. The remaining phase (light region in Figure 5.22 BSE) contains Cu,

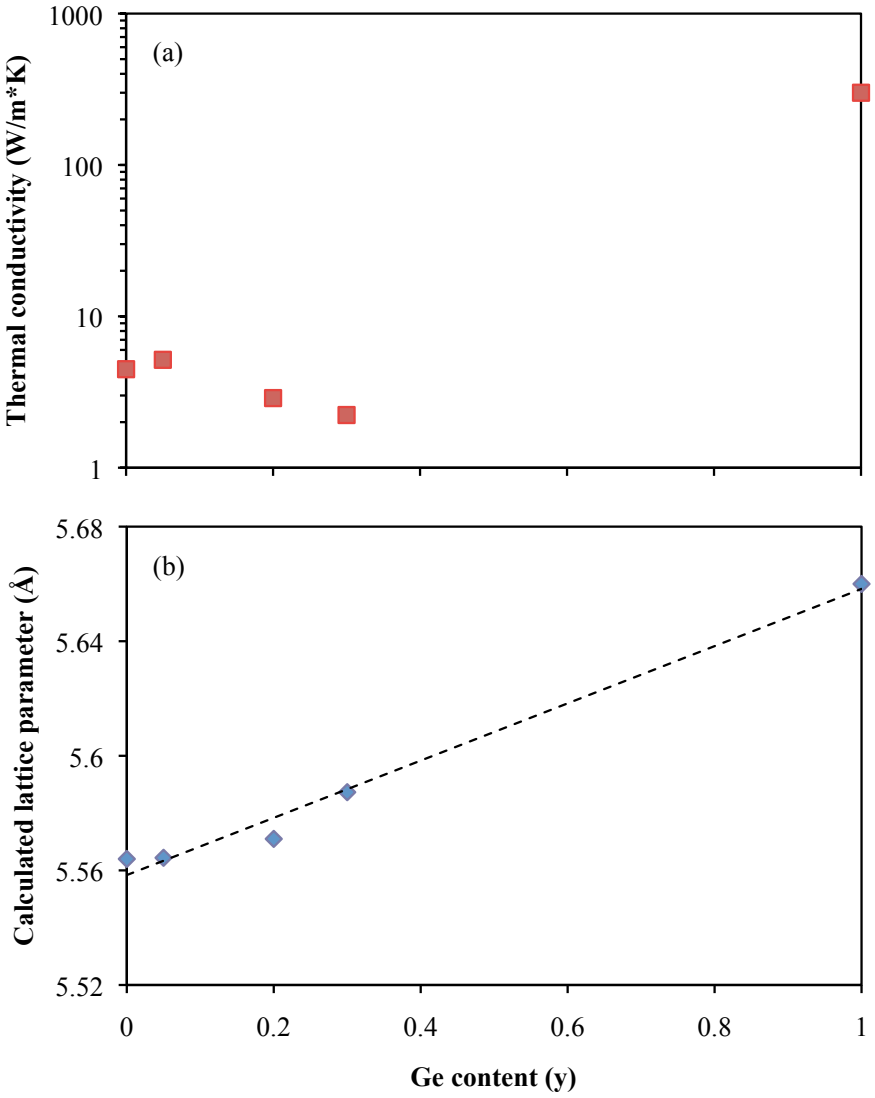

Figure 5.21: Measured thermal conductivity at 80K (a) and calculated lattice constant (b) versus Ge content for the $(Cu_2Ge_{1.55}Se_3)_{1-y}Ge_y$ solid solution. The dashed line in (b) represents the linear relation predicted by Vegard's law. The data for pure Ge are taken from [45] and [94].

Ge, and Se. The results of EDS analysis on the majority phase in the $Cu_2Ge_{1+x}Se_3$ samples given in Table 5.2 indicate that the composition of the majority phase region is changing with increasing x. The increasing measured Ge content with increasing x (see Figure 5.23) confirms the hypothesis that the Cu_2GeSe_3 lattice is able to incorporate excess Ge, and refutes the claim by Sharma *et. al.* that the only off-stoichiometric ternary compound occurs at x = 1.55 [71].

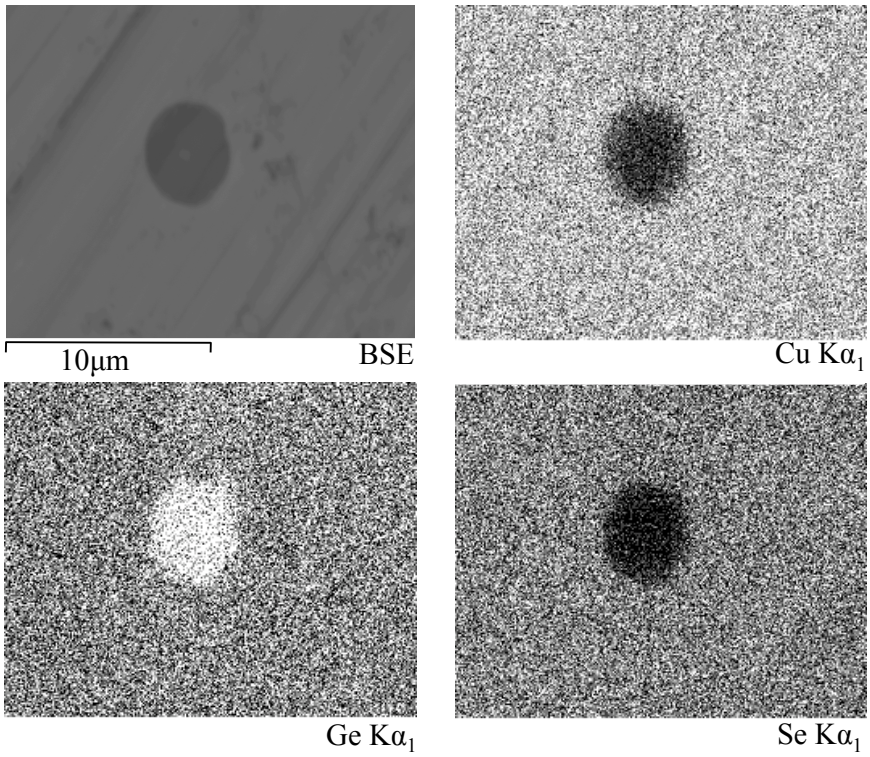

Figure 5.22: EDS X-ray mapping of a typical region of a $Cu_2Ge_{1+x}Se_3$ sample. Upper left BSE image shows the mapped region, remaining images show the distribution of Cu, Ge, and Se as indicated

Figure 5.23 shows that the measured composition is always slightly greater than the ideal composition until x=1.2 where the Ge content begins to saturate. The $Cu_2Ge_{2.2}Se_3$ sample was found to have very large Ge-rich regions (see Figure 5.24), likely because the solubility limit of Ge in Cu_2GeSe_3 was reached and the excess Ge was rejected. Based on these results it is concluded that Ge is soluble in Cu_2GeSe_3 although this system does not form a complete solid solution. The

Table 5.2: EDS compositions of the majority phase for selected $Cu_2Ge_{1+x}Se_3$ compounds.

Ideal Composition		at% Cu	at% Ge	at% Se	EDS Composition
Cu_2GeSe_3	ideal	33.3	16.67	50.00	$Cu_{2.01}Ge_{0.99}Se_{3.01}$
	measured	33.43	16.44	50.13	
$Cu_2Ge_{1.2}Se_3$	ideal	32.26	19.35	48.39	$Cu_{1.77}Ge_{1.71}Se_{2.73}$
	measured	28.47	27.54	43.99	
$Cu_2Ge_{1.4}Se_3$	ideal	31.25	21.88	46.88	$Cu_{1.68}Ge_{1.62}Se_{3.10}$
	measured	26.28	25.32	48.41	
$Cu_2Ge_{1.55}Se_3$	ideal	30.53	23.66	45.80	$Cu_{1.87}Ge_{1.81}Se_{2.86}$
	measured	28.64	27.64	43.72	
$Cu_2Ge_{1.6}Se_3$	ideal	30.30	24.24	45.45	$Cu_{1.93}Ge_{1.91}Se_{2.76}$
	measured	29.18	29.00	41.82	
$Cu_2Ge_{1.8}Se_3$	ideal	29.41	26.47	44.12	$Cu_{1.87}Ge_{2.06}Se_{2.86}$
	measured	27.64	30.24	42.13	
$Cu_2Ge_2Se_3$	ideal	28.57	28.57	42.86	$Cu_{1.94}Ge_{2.08}Se_{2.98}$
	measured	27.73	29.74	42.52	
$Cu_2Ge_{2.2}Se_3$	ideal	27.78	30.55	41.67	$Cu_{2.21}Ge_{2.19}Se_{2.81}$
	measured	30.63	30.35	39.03	

results from EDS analysis and lattice thermal conductivity measurements indicate that the solubility limit of Ge in Cu_2GeSe_3 is approximately 16.67%, in reasonable agreement with the original finding of 14% by Goryunova [60].

The microstructure of the quenched $Cu_2Ge_2Se_3$ sample was also investigated using SEM and EDS, and no secondary phases were found. Quenching the $Cu_2Ge_{1+x}Se_3$ may be a viable route to forming single phase compounds, but the brittle nature of the resulting ingots makes transport property measurements difficult. This could potentially be avoided using ball milling and hot pressing, but a separate investigation on the effect of hot pressing on the microstructure of these compounds would be required which is beyond the scope of this work. In addition, the isolated secondary phase regions found in the slow cooled samples will likely have little impact on the thermal con-

ductivity values reported here since they comprise only a small portion of the microstructure and are on the order of tens of microns, much larger than would be required to produce a substantial phonon scattering effect.

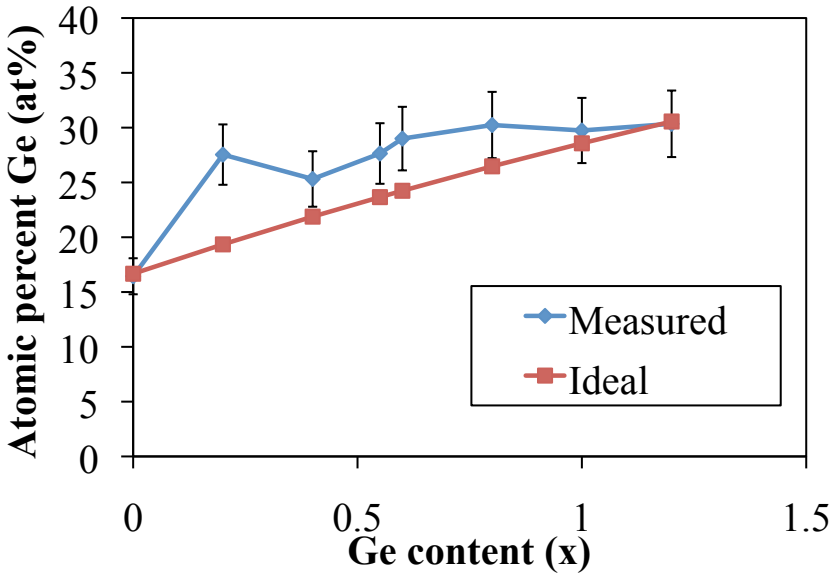

Figure 5.23: EDS composition (at% Ge) versus starting Ge content (x) for $Cu_2Ge_{1+x}Se_3$ compounds. Error bars indicate $\pm 10\%$ error associated with EDS measurement.

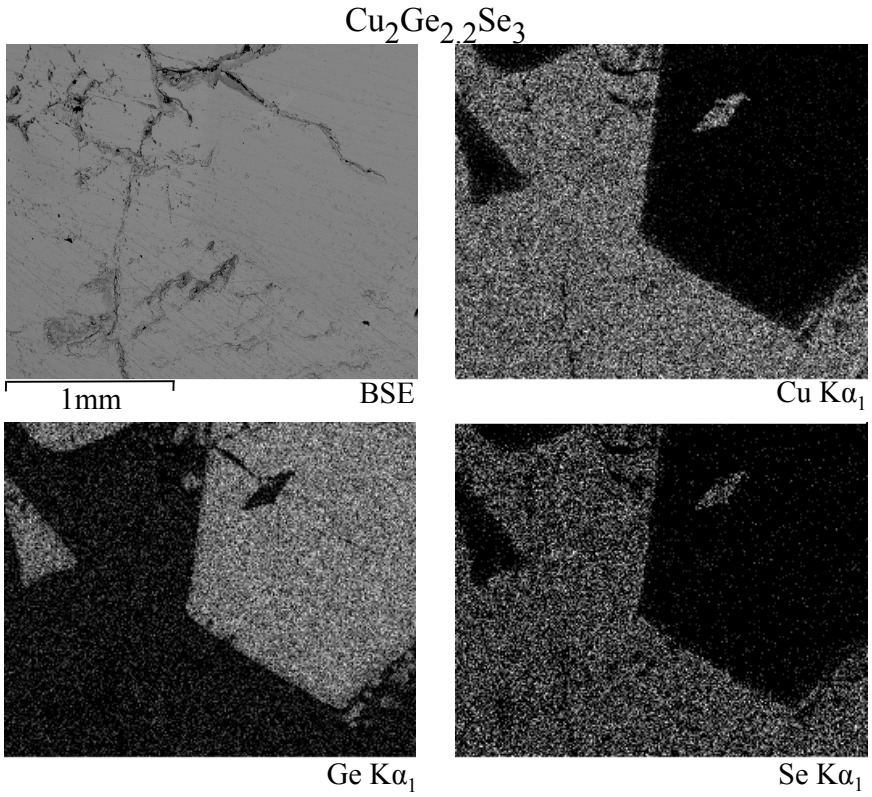

Figure 5.24: EDS X-ray mapping of a typical region of a $Cu_2Ge_{2.2}Se_3$ sample. Upper left BSE image shows the mapped region, remaining images show the distribution of Cu, Ge, and Se as indicated

5.5.3 Summary

The structural and thermoelectric properties of $Cu_2Ge_{1+x}Se_3$ compounds with x ranging from -0.15 to 1.2 have been evaluated. The stoichiometric Cu_2GeSe_3 compound was found to have an orthorhombic structure with a =1.1878 nm, b = 0.3941 nm, and c = 5.485 nm in agreement with Parthe [69]. The orthorhombic structure formed independent of cooling rate indicating that a disordered cubic phase is unlikely for this compound, in contrast to Cu_2SnSe_3. Off-stoichiometric Cu_2GeSe_3 was investigated as a means of reducing the lattice thermal conductivity and improving the thermoelectric properties.

For compounds with x<0 the crystal structure gradually changed from orthorhombic to monoclinic as x decreased. The compound $Cu_2Ge_{0.85}Se_3$ had a purely monoclinic structure with a = 0.5512 nm, b = 0.5598 nm, c = 0.5486 nm, and β = 89.7°, in agreement with Sharma *et. al.* [70]. The lattice thermal conductivity did not decrease substantially as a result of the change in composition, indicating that vacancies are not being created in the lattice. The Ge deficiency did have a large effect on the electronic properties; the hole concentration increased rapidly with decreasing x and at x = -0.15 the compound is essentially metallic, as evidenced by its low electrical resistivity and small temperature independent Seebeck coefficient. The thermoelectric properties of Cu_2GeSe_3 were improved only slightly for the x = -0.01 sample, and thus the x<0 compounds were not pursued further.

For compounds with x>0 the crystal structure gradually changed from orthorhombic to cubic for small x values, and at x = 0.55 the structure was purely cubic (zincblende) with a = 0.5561 nm, in agreement with Sharma *et. al.* [70]. When x>0.55 the structure remained cubic and the X-ray diffraction peaks shifted to lower 2θ values with increasing x, indicating an expansion of the lattice from excess Ge substitution. The lattice thermal conductivity decreased substantially with increasing x and was approximately 32% lower at room temperature for the x = 1 sample relative to the x = 0 sample. The shifted X-ray peaks and lowered lattice thermal conductivity indicated a solid solution between the cubic $Cu_2Ge_{1.55}Se_3$ and Ge which, based on calculated

lattice constants, seemed likely. SEM and EDS were used to evaluate the microstructure and phase purity of the x>0 samples. For all samples with excess Ge small (tens of microns) inclusions of a Ge rich phase (nearly pure Ge) were always present in a matrix of a Cu, Ge, and Se ternary phase. The composition of the majority phase changed with increasing x as expected, indicating that the excess Ge is incorporated in to the Cu_2GeSe_3 lattice. The Ge content saturates at approximately x = 1, and for x = 1.2 very large (millimeter size) Ge rich phase regions were present. The Ge-rich inclusions can be eliminated by quenching the sample in water from high temperature, but the resulting ingots are extremely brittle which makes reliable transport property measurements challenging. The thermoelectric properties were optimized for the x = 1.0 sample, which showed ZT = 0.016 at room temperature. Controlling the carrier concentration proved to be a problem in these compounds and sample to sample variations in the electronic properties were prevalent, similar to the situation encountered for Cu_2SnSe_3.

5.6 Cu_3SbSe_4

The compound Cu_3SbSe_4, a fourth-order ternary derivative of ZnSe, was identified by Hirono *et. al.* [67] and Nakanishi *et. al.* [74] as a potential thermoelectric material, yet it has since been explored very little for thermoelectric applications. At the beginning of this work no systematic doping studies had been completed, and thus the original intent of this work was to identify dopant species and optimize the carrier concentration for thermoelectric applications.

5.6.1 Experimental

Samples of $Cu_3Sb_{1-x}A_xSe_4$ (A = Ge or Sn) were prepared according to the procedure outlined in Section 3.1. The reaction temperature was 900°C and samples were cooled to room temperature either by water quenching or slow cooling in the furnace.

Water quenched samples were found to have significant red/orange deposits on the inside of the ampoule after quenching and were subsequently annealed for 48 hours at 300°C. After annealing all of the deposited material was reincorporated into the ingot, and samples were prepared for transport measurements.

The as-solidified ingots were very brittle and preparing a sample for reliable transport measurements proved to be a challenge. Thus, powder processing was used to form high-quality samples for all of the measurements reported here. The annealed $Cu_3Sb_{1-x}A_xSe_4$ ingots were ball milled in an argon environment for 30 minutes using a SPEX 8000M vibratory mixer equipped with a stainless steel vial and grinding media. The milled powders were then sieved using a 100 mesh screen to remove any remaining large pieces. Finally, the powders were hot pressed in a graphite die under argon using 70 MPa of pressure at 400°C for 30 minutes. The hot pressed samples had measured densities >93% of the theoretical density (measured using the Archimedes method), and samples for transport property measurements were cut directly from the hot pressed pellets. SEM analysis for this portion of the work was completed at Oak Ridge National Laboratory.

5.6.2 Results and Discussion

Slow cooled samples of Cu_3SbSe_4 were found to contain Sb_2Se_3 as an impurity phase (see Figure 5.25), in agreement with the results of Scott and Kench [73]. Since Cu_3SbSe_4 forms via a peritectic reaction, only quenched samples had a single phase microstructure. Originally, samples were quenched from 900°C, but it was later determined that quenching from 500°C produced the same single phase microstructure without vigorous splashing of the melt. Thus, all of the samples reported here were quenched from 500°C into water. Figure 5.26 shows the XRD pattern of a Cu_3SbSe_4 sample quenched from 500°C and hot pressed at 400°C, illustrating that the single phase microstructure is maintained after hot pressing. All of the peak positions match with those reported by Pfitzner for tetragonal Cu_3SbSe_4 (space group $I\bar{4}2m$, a = 5.6609 Å, c = 11.28 Å). The single phase microstructure was confirmed using scanning electron microscopy; Figure 5.27 shows EDS X-ray mapping of a typical region of Cu_3SbSe_4, indicating a homogeneous distribution of Cu, Sb, and Se. No high temperature cubic phase was found for Cu_3SbSe_4, indicating that the Cu and Sb atoms prefer an ordered arrangement.

Similar to the Cu_2-(Ge, Sn)-Se_3 compounds, controlling the carrier concentration in Cu_3SbSe_4 proved to be a challenge. Samples that were prepared without the post-quench annealing step had hole concentrations $>10^{19}$ cm^{-3}, with large variations in the hole concentration from sample to sample. As mentioned above, after annealing at 300°C for 48 hours all of the deposited red/orange material was reincorporated into the Cu_3SbSe_4 ingot. The deposited material was likely amorphous Se since Se has the highest vapor pressure among the constituent elements. With deposited Se on the ampoule wall after quenching the stoichiometry of the Cu_3SbSe_4 ingot is deviated from ideal, causing Se vacancies in the structure. A Se vacancy ($V_{Se}^{\bullet\bullet}$) acts as an acceptor impurity in Cu_3SbSe_4, causing the hole concentration to increase. This self doping causes a hole concentration of $\sim 10^{19}$ cm^{-3} that is degenerate over the entire temperature range studied (Figure 5.29). After annealing, the stoichiometry is returned to the ideal 3:1:4 and the hole concentration is decreased to $\sim 4\times10^{17}$ (see Figure 5.29). The temperature dependence of the hole mobility follows a $T^{-3/2}$

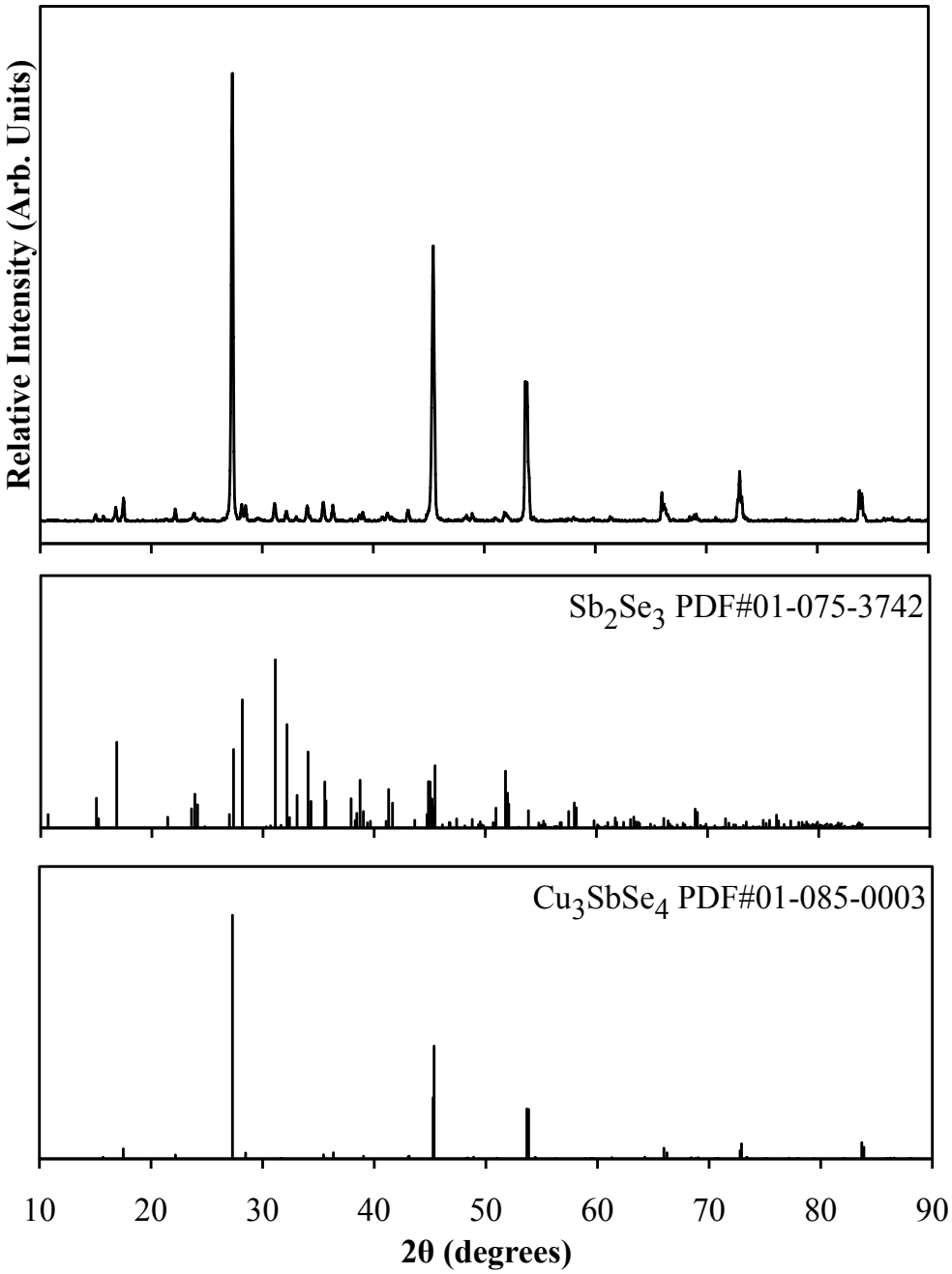

Figure 5.25: XRD pattern of a Cu_3SbSe_4 sample slow cooled from 900°C to room temperature, along with the PDF data for Sb_2Se_3 and Cu_3SbSe_4.

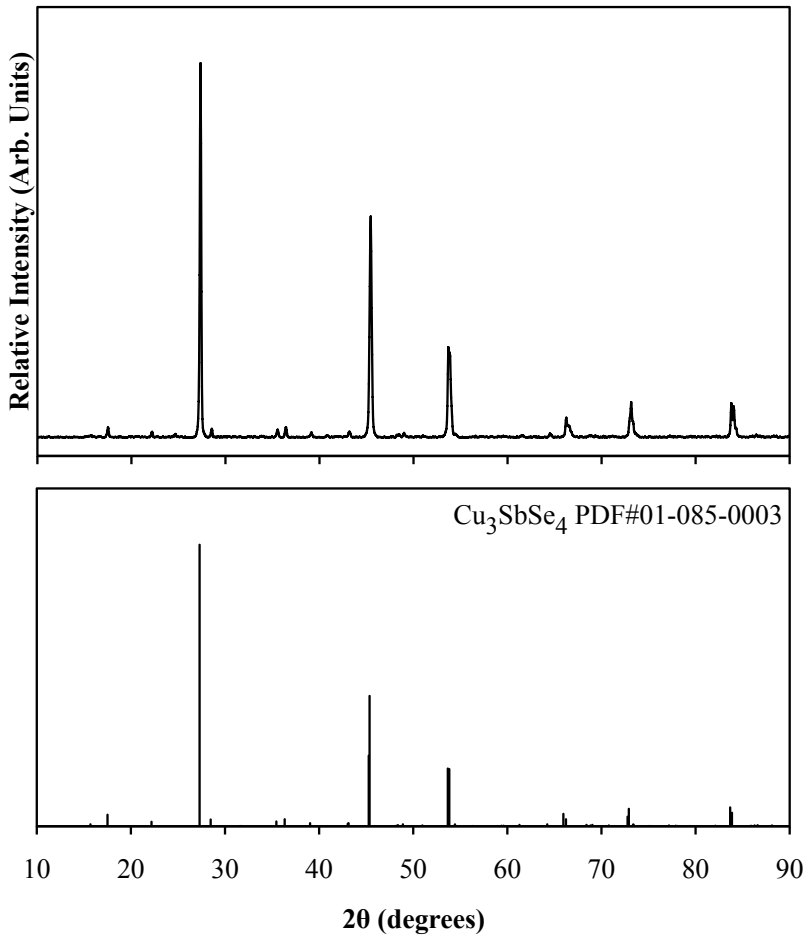

Figure 5.26: XRD pattern of a Cu_3SbSe_4 sample quenched from 500°C to room temperature, along with the PDF data for Cu_3SbSe_4.

trend, indicating that holes are scattered predominantly by acoustic phonons. The lowered hole concentration is easily reproduced for samples that are prepared by quenching, annealing, and hot pressing as described above.

Subsequent to establishing the synthesis procedure for Cu_3SbSe_4, the focus was shifted to systematically controlling the carrier concentration. Ge and Sn were chosen as p-type dopant species because they have one less valence electron than Sb, and they will act as acceptor impurities on the Sb site. Samples with up to 4% Ge or Sn on the Sb site were synthesized with no detectable

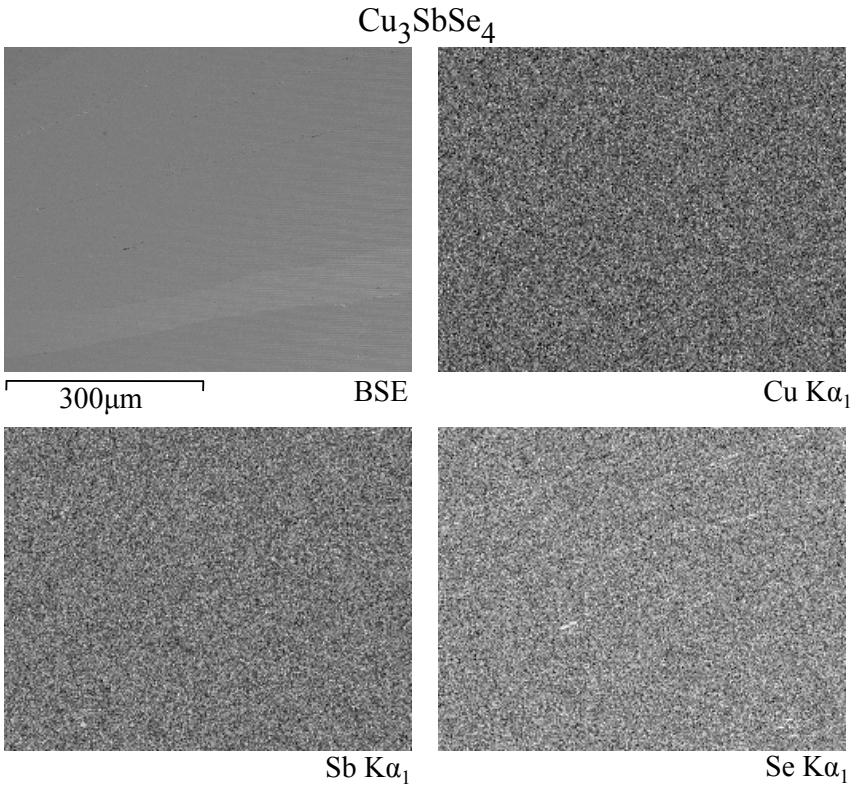

Figure 5.27: EDS X-ray mapping of a typical region of Cu_3SbSe_4 (work completed at ORNL). Upper left image shows a backscattered electron image of a 600μm x 600μm region, and the distributions of Cu, Sb, and Se in the same region are shown as indicated (white pixel indicates presence of element).

impurity phases. The hole concentration and mobility of the Ge and Sn doped samples are shown in Figure 5.29. The hole concentration increases with increasing doping and is degenerate for all doped samples, and the mobility decreases with increasing doping due to ionized impurity scattering. The mobilities of the Ge-doped samples are slightly larger than those of the Sn-doped samples likely due to the smaller electronegativity difference between Sn and Sb which, as discussed by Slack, causes increased carrier scattering [99].

The electronic properties (80 - 630K) of the doped compounds are shown in Figure 5.30. The onset of intrinsic conduction occurs just above room temperature for the undoped (x = 0) com-

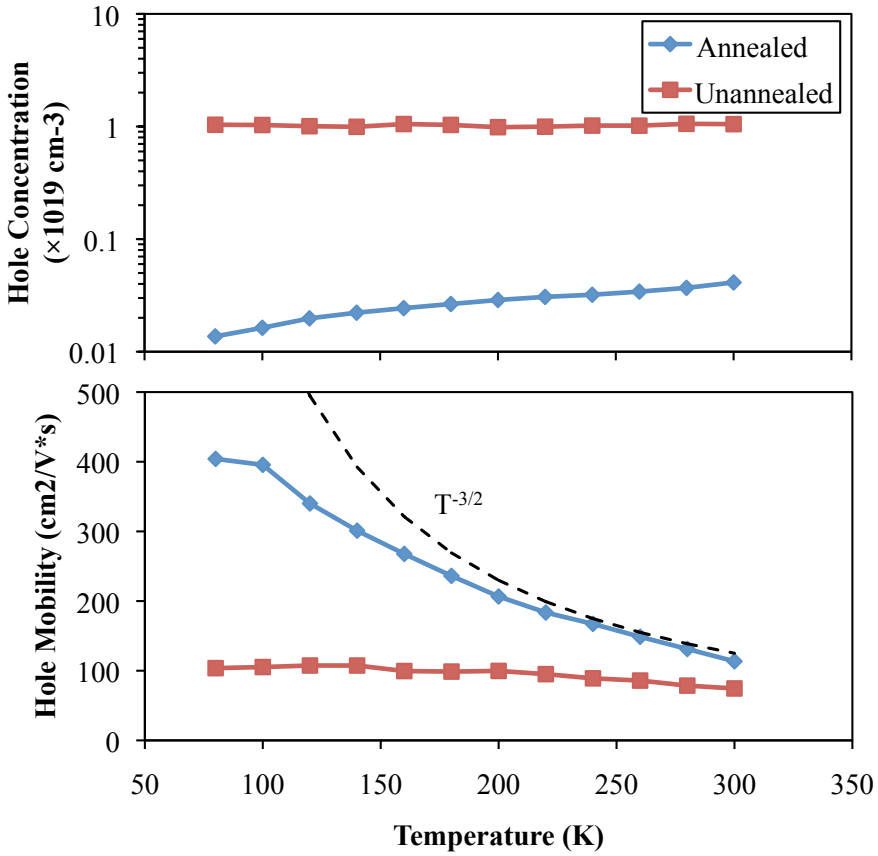

Figure 5.28: Temperature dependence of the hole concentration and mobility for Cu_3SbSe_4, with and without the post-quench 300°C/48 hrs annealing step. Dashed line indicates the $T^{-3/2}$ temperature dependence characteristic of carrier scattering by acoustic phonons.

pound, as evidenced by the simultaneous decrease in Seebeck coefficient (S) and electrical resistivity (ρ). Intrinsic conduction is suppressed with doping, and S and ρ both increase with temperature for all of the doped samples. S and ρ decrease with increasing doping as is expected due to the increasing carrier concentration. The power factor (S^2/ρ) is optimized at the 3% doping level for both Ge and Sn, although it is higher for the 3% Ge doped sample due to the slightly higher mobility. The power factor reaches nearly 16 μW/cm*K^2 for the 3% Ge doped sample at 630K, rivaling that of state of the art thermoelectric materials such as PbTe in this temperature range [95].

The thermal conductivity (Figure 5.31) follows a T^{-1} temperature dependence over the entire

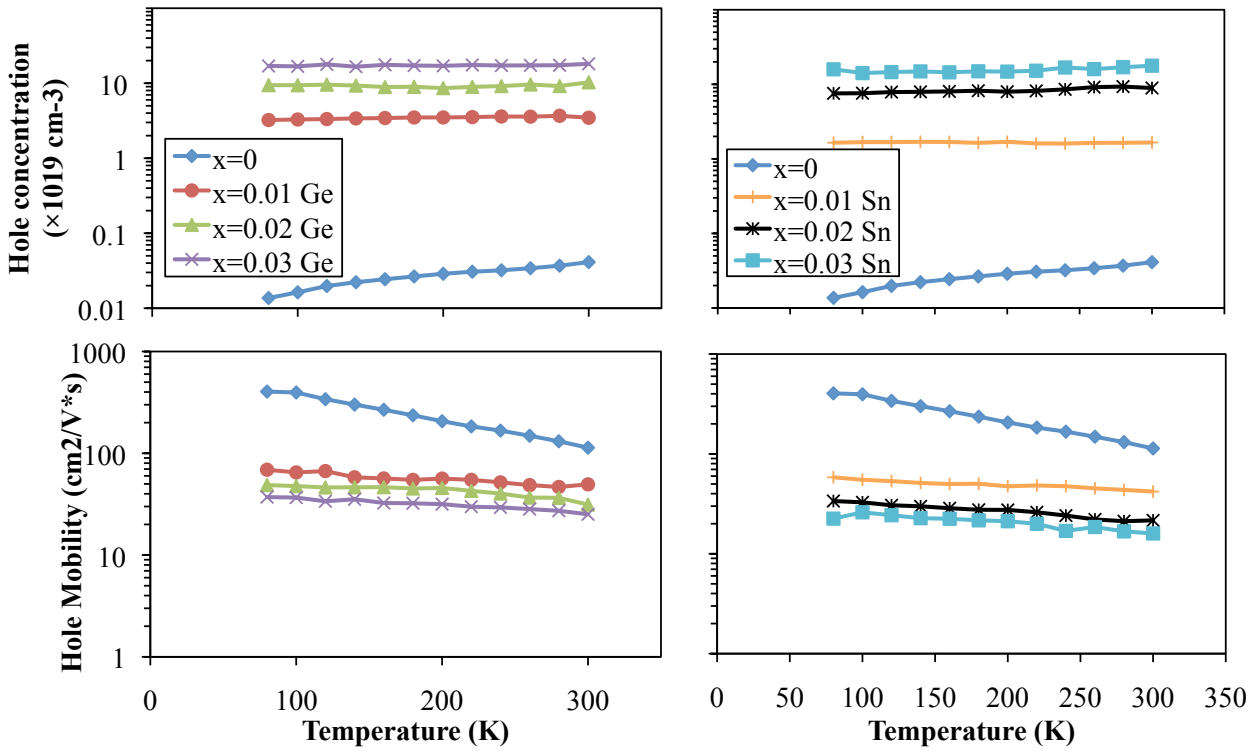

Figure 5.29: Temperature dependence of the hole concentration and mobility of $Cu_3Sb_{1-x}A_xSe_4$ compounds (A = Ge or Sn).

temperature range, indicative of phonon-phonon Umklapp scattering, and is still decreasing at 630K. The high temperature thermal conductivity was calculated as follows:

$$\kappa = D\,\rho\,c_p \tag{5.13}$$

where D, ρ, and c_p are the measured values for thermal diffusivity, density, and specific heat capacity respectively (for measurement techniques refer to Section 3.3). The total thermal conductivity approaches 1 W/m*K at 630K and increases slightly with increasing doping level due to the electronic contribution, which constitutes approximately 15% of the total at high temperature for the 3% doped samples (calculated from the Wiedemann-Franz law using $L_0 = 2.44\times10^{-8}$ $W\Omega K^{-2}$). The 2% doped samples have the highest ZT values (lower plot, Figure 5.31), in the neighborhood

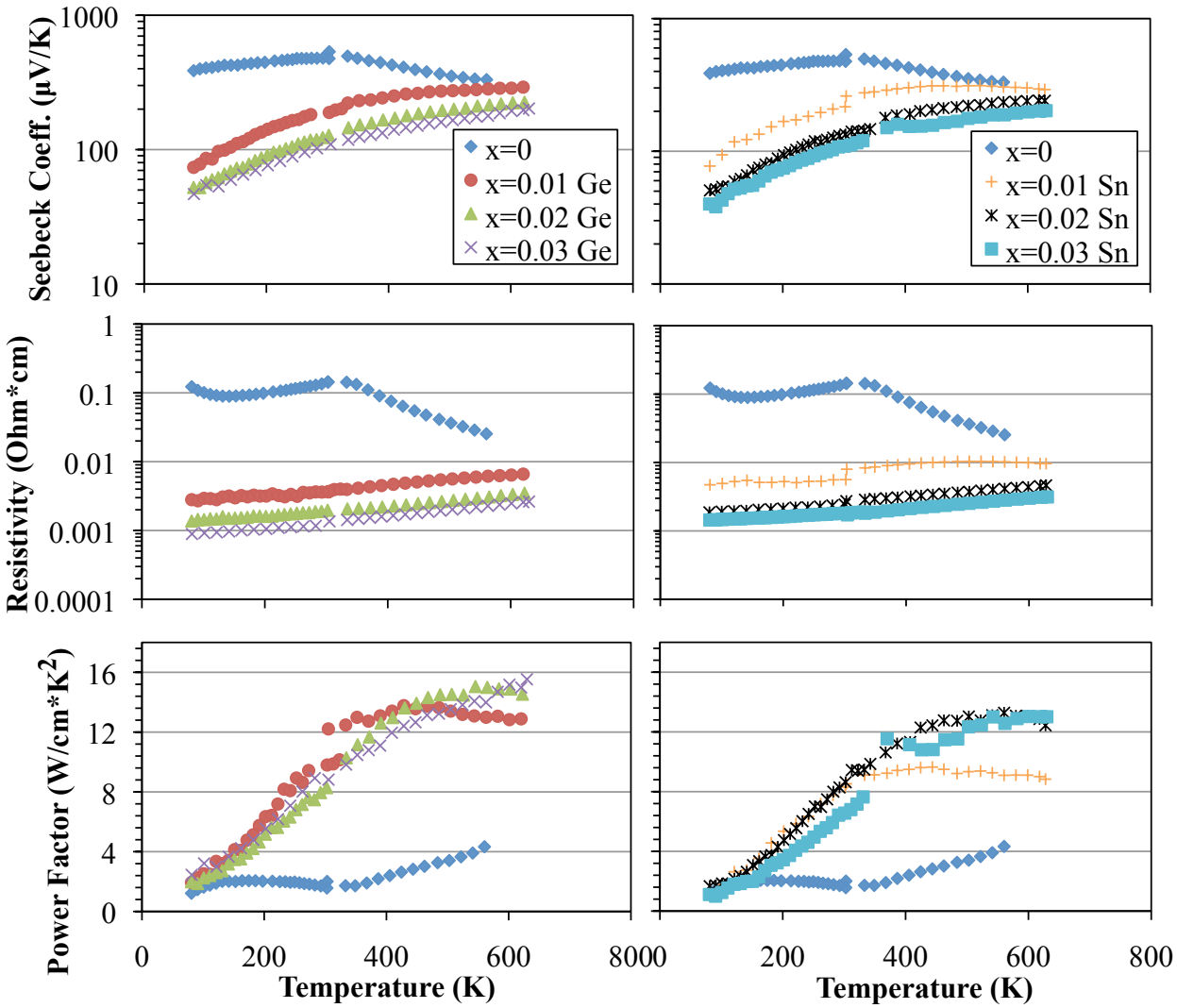

Figure 5.30: Temperature dependence of the electronic properties of the $Cu_3Sb_{1-x}A_xSe_4$ compounds (A = Ge, Sn).

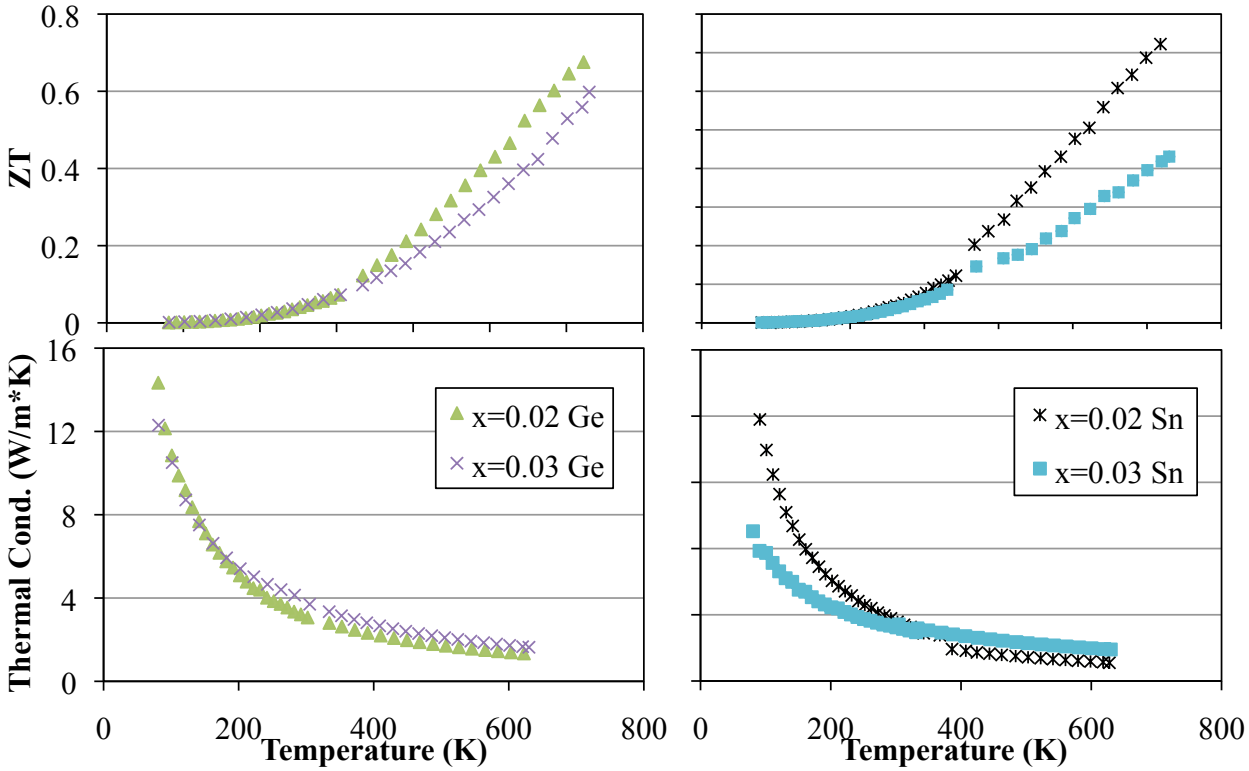

Figure 5.31: Temperature dependence of the thermal conductivity and dimensionless thermoelectric figure of merit of the $Cu_3Sb_{1-x}A_xSe_4$ compounds (A = Ge, Sn).

of 0.7 at 630K. These ZT values rival some of the best p-type thermoelectric materials in this temperature range including PbTe, Ce-filled skutterudites, and TAGS compounds. They have the added advantage of being free of toxic Pb, costly Ag, and rare earth elements that are in uncertain supply. Unfortunately, the low melting temperature of these compounds ($\sim$460°C) prevents the extension of the measurements to higher temperatures.

Many attempts were made to produce n-type Cu_3SbSe_4, but all were unsuccessful. Zn doping on the Cu site was tried first in an effort to reproduce the results of Scott *et. al.* [73], but n-type conductivity was never achieved. The problem with Zn doping in Cu_3SbSe_4 is that its crystal structure is very similar to ZnSe, and a ZnSe impurity in Cu_3SbSe_4 cannot be detected by XRD. This similarity in crystal structure was exploited in an attempt to formulate compounds of the form $(Cu_3SbSe_4)_{1-x}(ZnSe)_x$ and in particular the quaternary compound $Cu_3ZnSbSe_5$ (in the spirit of

the Cu_2SnSe_3 - ZnSe solid solution which is known to contain $Cu_2ZnSnSe_4$, a thermoelectric material with ZT_{max} = 0.95 [18]), but it was found that Cu_3SbSe_4 and ZnSe are immiscible. Subsequent n-type doping attempts included Ga and In on the Cu site, Br and I on the Se site, and Se on the Sb site (varying the Sb/Se ratio), but none were able to produce n-type material. The strong preference of Cu_3SbSe_4 towards p-type conductivity is attributed to intrinsic defects which create impurity levels in the band structure and dominate the conduction even after optimizing the synthesis procedure and adding n-type dopants.

5.6.3 Summary

This work has revealed Cu_3SbSe_4 to be a promising new p-type thermoelectric material. Single-phase material can be easily produced by quenching the melt from 500°C into water, suppressing the formation of secondary phases that are present in slow-cooled samples. The crystal structure of Cu_3SbSe_4 is tetragonal wtih the Cu and Sb atoms assuming an ordered arrangement on the cation sublattice. The hole concentration of as-quenched, undoped material is always $>10^{19}$ cm^{-3} and varies from sample to sample. A post-quench 300°C annealing step reincorporates lost Se into the material, presumably decreasing the number of intrinsic defects which cause self-doping, and produces samples with hole concentrations reproducibly near 10^{18} cm^{-3}.

P-type doping can be accomplished using Ge or Sn as dopant species on the Sb site. The hole concentration increases with increasing Ge or Sn content, and all doped samples studied here were found to be degenerate. The hole mobility remains above 25 $cm^2/V*s$ at room temperature for all doping levels. The Seebeck coefficient and electrical resistivity both decrease with increasing doping, and the optimized thermoelectric power factor reaches 16 $\mu W/cm*K^2$ for the 3% Ge doped compound. The thermal conductivity follows a T^{-1} temperature dependence and approaches 1 W/m*K at high temperature. The highest ZT value is obtained for the 2% Sn doped sample, which has ZT=0.72 at 630K, approaching that of some of the best p-type thermoelectric materials in this temperature range.

The Cu_3SbSe_4-based compounds offer several advantages over traditional thermoelectric materials in that they contain no toxic or expensive elements and require no nanostructure to achieve good thermoelectric performance. Their operating temperature is limited by the melting temperature of the compound, but could be used in applications with 300-400°C operating temperatures.

5.7 The Cu_3SbSe_4-Cu_3SbS_4 Solid Soluiton

The above results on Cu_3SbSe_4 are promising, but there is much room for improvement. The lattice thermal conductivity of the $Cu_3Sb_{1-x}A_xSe_4$ compounds is in the range of 0.9 - 1.0 W/m*K at the highest measurement temperature, approximately twice that of the calculated minimum lattice thermal conductivity of 0.46 W/m*K (refer to Section 6 for a discussion of "minimum thermal conductivity"). Thus, in an effort to reduce the lattice thermal conductivity and improve the thermoelectric properties of Cu_3SbSe_4, solid solutions with similar compounds were investigated. The only reported solid solution in the I_3-V-VI_4 family of compounds has been Cu_3AsS_4-Cu_3SbS_4, which forms a complete solid solution with a structural transformation at 80% Cu_3AsS_4 [96]. The options for isoelectronic substitutions in Cu_3SbSe_4 are limited since As is highly toxic and Ag-based compounds do not exist in this series. Bi substitution on the Sb site and Te substitution on the Se site were attempted, but neither element was able to be incorporated into the Cu_3SbSe_4 lattice. This leaves Cu_3SbS_4, which has the same tetragonal crystal structure as the selenide (space group $I\bar{4}2m$ no. 121) with smaller lattice constants a = 5.391 Å and c = 10.764 Å [97]. Cu_3SbS_4 has seen mainly structural investigations, although it is known to be a semiconductor with E_g = 0.46 eV [98]. No investigations of the Cu_3SbSe_4-Cu_3SbS_4 system appear in the literature.

5.7.1 Experimental

Samples of $Cu_3SbSe_{4-x}S_x$ (x ranging from 0 to 4) were prepared in the same way as the Cu_3SbSe_4 compounds (see Section 5.6.1). The only difference was that compounds with $x > 0$ were quenched from 600°C and then annealed at 350°C to account for the increase in melting temperature with S content. Additional XRD data were collected at Oak Ridge National Laboratory from 15 to 140° 2θ on a Panalytical MPD with Cu Kα radiation, parafocusing geometry, and a position-sensitive detector. The lattice parameters were then refined using the Rietveld method, with the HighScore Plus computer program. All hot pressed samples were > 94% dense, and all samples for transport

property measurements were cut directly from the hot pressed pellets.

5.7.2 Results and Discussion

Cu_3SbSe_4 and Cu_3SbS_4 form a complete solid solution, as evidenced by the gradual shift of the XRD peaks to higher 2θ values with increasing S content (Figure 5.32), indicating a gradual contraction of the lattice. The refined lattice parameters (Figure 5.33 and Table 5.3) decrease linearly with S content, in agreement with Vegard's law (indicated by dashed lines). The refined lattice constants of the end compounds (x = 0 and 4.0) given in Table 5.3 are in reasonable agreement with previously reported values [72], [97]. The XRD peaks for the intermediate compositions broaden considerably due to increased microstrain in the lattice, which arises due to the smaller S atoms substituting on the Se sites.

Table 5.3: Refined lattice constants for the $Cu_3SbSe_{4-x}S_x$ compounds, estimated standard deviation of the last digit is given in parentheses.

Cu_3SbS_4 content (x)	*a* (Å)	*c* (Å)
0	5.65813(9)	11.2584(3)
0.4	5.62992(5)	11.2052(1)
1.2	5.5773(1)	11.1070(4)
2.0	5.5235(1)	11.0090(5)
2.8	5.4698(3)	10.854(1)
3.6	5.4177(3)	10.765(1)
4.0	5.3937(3)	10.724(1)

Hall data for the $Cu_3SbSe_{4-x}S_x$ compounds ($x \leq 2.0$) are shown in Figure 5.34. The optimized synthesis procedure again produced samples with low hole concentrations on the order of 10^{17} - 10^{18} cm^{-3}. The hole concentration tends to increase with increasing S content, presumably due to defects that were not eliminated during annealing. The hole mobility decreases with increasing

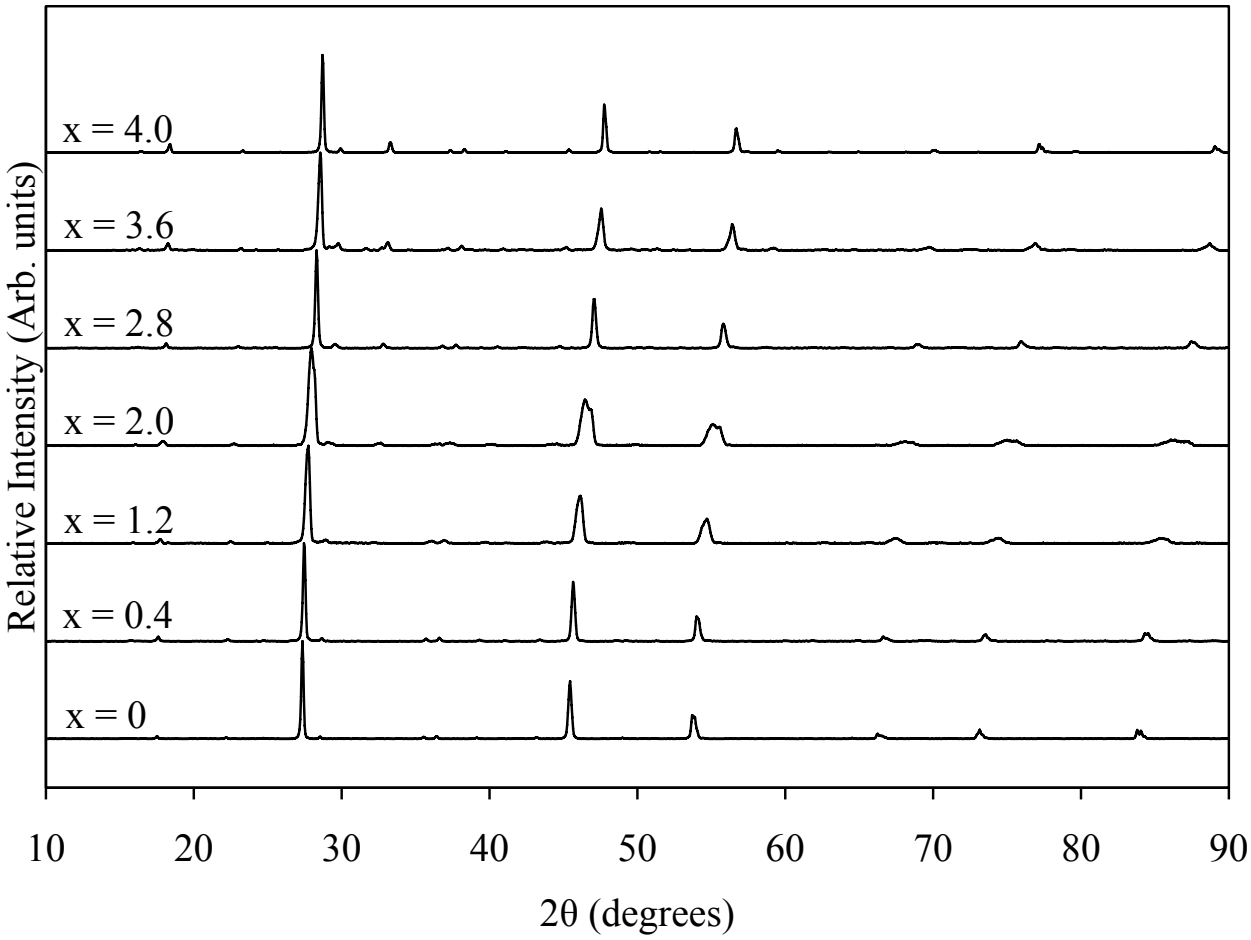

Figure 5.32: XRD patterns of $Cu_3SbSe_{4-x}S_x$ samples.

S content due to neutral impurity scattering, but remains above 10 $cm^2/V*s$ for all samples ($x \leq 2.0$).

The primary interest here is the effect of S substitution on the lattice thermal conductivity (κ_L) of Cu_3SbSe_4. The temperature dependence of κ_L for selected samples is shown in Figure 5.35. For the x = 0 sample, the temperature dependence is the typical T^{-1} indicative of phonon-phonon scattering only, but the addition of just 10% S causes the temperature dependence to weaken substantially due to phonon-impurity scattering. When 50% S is added, κ_L scales as just $T^{-0.5}$, and is reduced by nearly 75% at 80K. The temperature and compositional dependencies of κ_L can be understood using the Debye model, following the same procedure as the $Cu_2Sn_{1-x}Ge_xSe_3$ solid

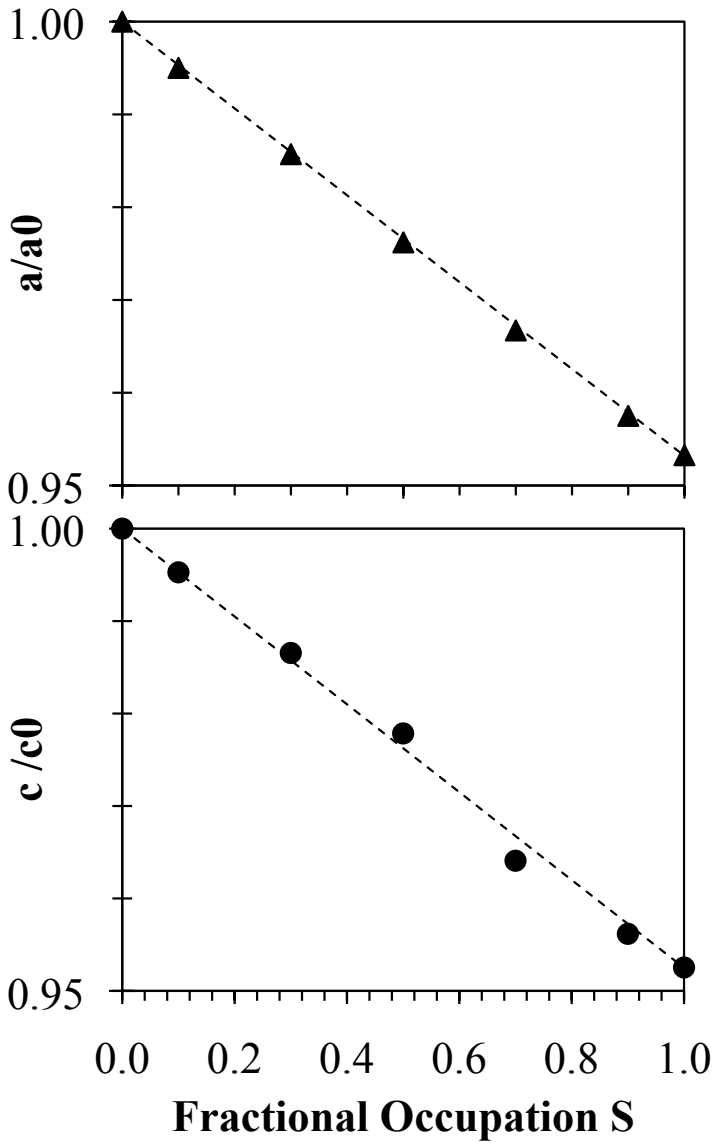

Figure 5.33: Refined lattice constants of the $Cu_3SbSe_{4-x}S_x$ samples (from Figure 5.32) versus fractional occupation S (equal to x/4). Dashed lines indicate linear relationship predicted by Vegard's law.

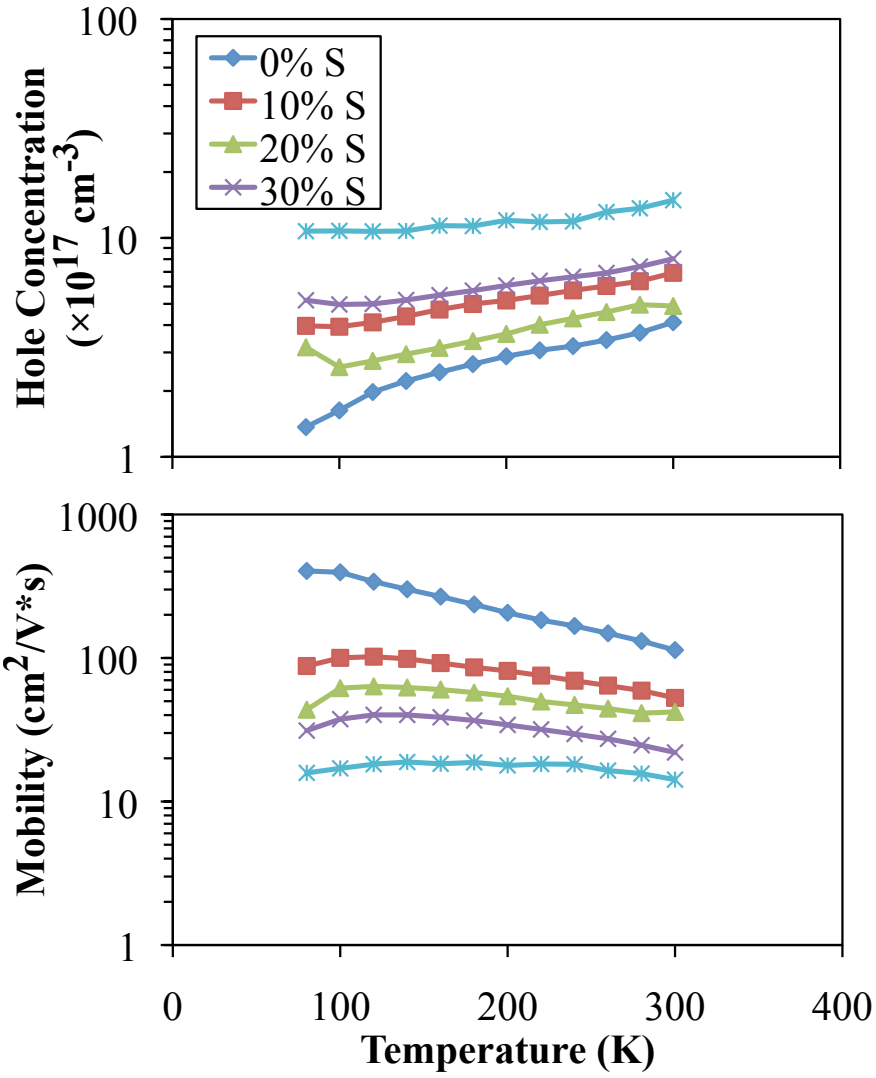

Figure 5.34: Hole concentration and mobility of the $Cu_3SbSe_{4-x}S_x$ compounds.

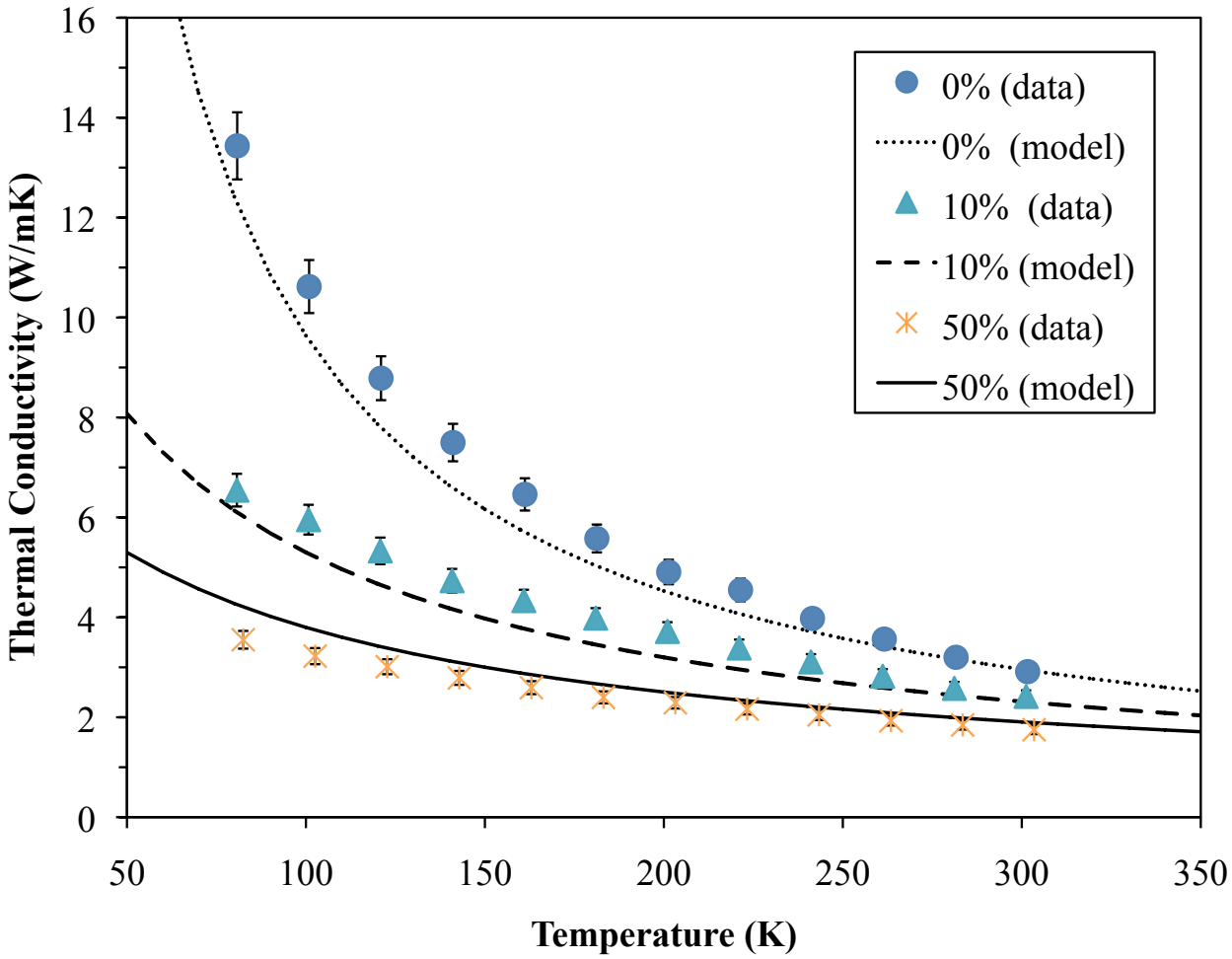

Figure 5.35: Temperature dependence of the thermal conductivity of selected $Cu_3SbSe_{4-x}S_x$ compounds. Dashed lines are the calculated lattice thermal conductivities obtained from the Debye model. Error bars indicate $\pm 5\%$ experimental error.

solution.

Following the procedure in Section 5.3.2, phonon scattering rates corresponding to grain boundaries, point defects, and phonon-phonon interactions (equation 5.6) are chosen for the calculation of κ_L from the Debye model (equation 5.2). Once again normal phonon-phonon processes are neglected due to the imperfect nature of the hot-pressed specimens studied, and thus τ_U^{-1} corresponds to phonon-phonon Umklapp scattering only. Based on SEM analysis, a grain size (L) of 20μm is used for the boundary scattering rate expression for all samples. The Grüneisen parameter

(γ) is again treated as adjustable to fit the data of the x = 0 sample and then held constant with composition. This procedure yields γ = 1.05, which is a reasonable estimate for zincblende-like compounds based on previous results [45]. Since no information is available regarding the Debye temperature (θ) or phonon velocity (v) of Cu_3SbS_4, estimates of the compositional dependence of these parameters must be made. The phonon velocity is held constant at 1991.2 m/s, corresponding to the estimated acoustic mode phonon velocity of Cu_3SbSe_4 [85]. The compositional dependence of θ is estimated from the expression:

$$\beta = \theta\, M^{1/2}\, V^{3/2} \tag{5.14}$$

where M and V are the average mass and volume per atom, and β is a constant for a given crystal system [91]. Using the procedure of Slack [45] and the reported Debye temperature of Cu_3SbSe_4 (θ_0 = 131K), the acoustic mode Debye temperature is estimated as θ_a = 65.5K. Now the compositional dependence of the Debye temperature can be estimated, and θ_a for Cu_3SbS_4 is found to be 84.4K.

The only remaining parameter to be calculated is Γ_T, the phonon-impurity scattering parameter. The best fit to the experimental data is obtained using ε = 190 in the calculation for Γ_S, in reasonable agreement with ε = 136 calculated from equation 5.12 using γ = 1.05 [91]. From equations 5.10 and 5.11, the phonon-impurity scattering parameters due to atomic mass differences (Γ_M) and strain field fluctuations (Γ_S) are calculated and given in Table 5.4. In stark contrast to the $Cu_2Sn_{1-x}Ge_xSe_3$ solid solution, the strain-field fluctuation term is dominant for $x \leq 0.5$ and still contributes significantly for $x > 0.5$, indicating that the size mismatch between S and Se contributes strongly to the reduced lattice thermal conductivity.

The calculated lattice thermal conductivity at 80 and 300K as a function of composition is shown in Table 5.4 and Figure 5.36. At room temperature the model fits the experimental data to within $\pm$ 16%, which is quite remarkable considering that no adjustable parameters were used

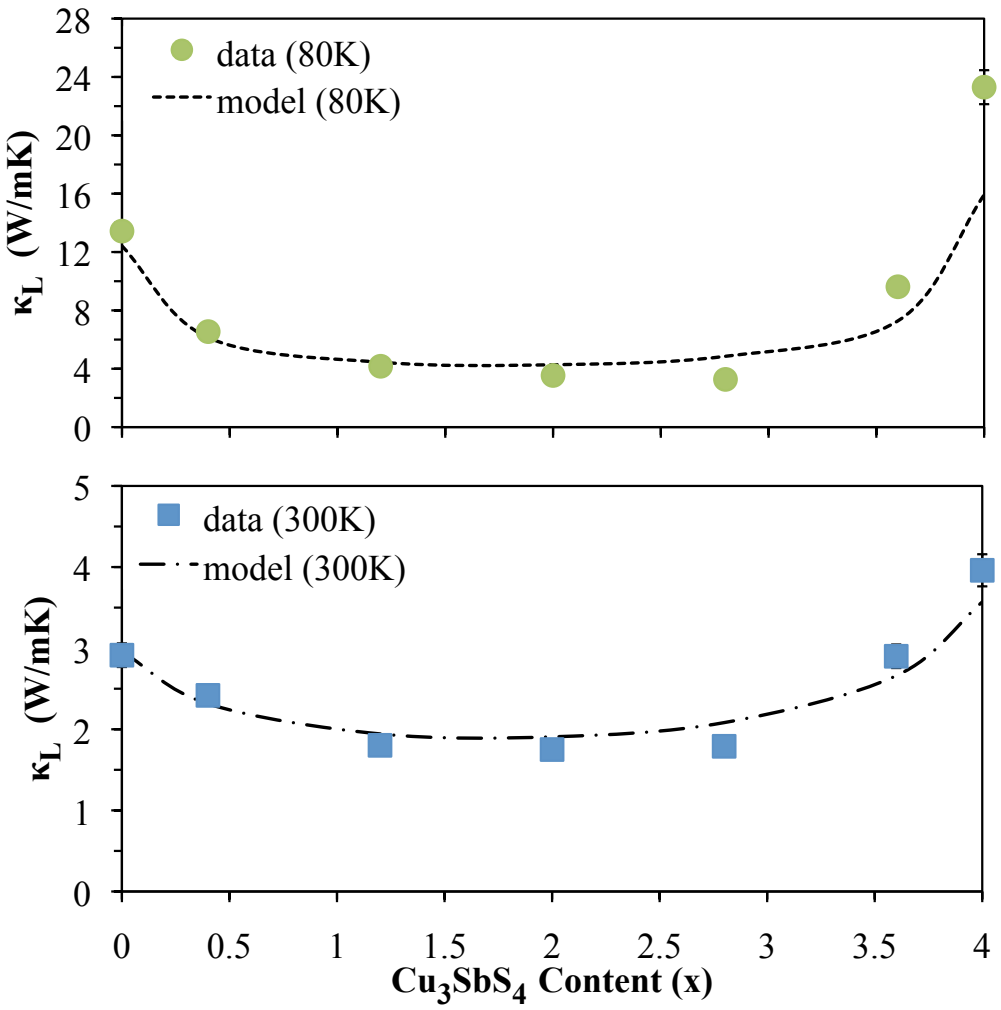

Figure 5.36: Compositional dependence of the lattice thermal conductivity (κ_L) of the $Cu_3SbSe_{4-x}S_x$ compounds at 80K and 300K. Dashed lines are the calculated lattice thermal conductivities obtained from the Debye model. Error bars indicate $\pm 5\%$ experimental error.

Table 5.4: Phonon-impurity scattering parameters along with calculated (κ_{calc}) and measured (κ_{exp}) thermal conductivities (in W/m*K) for the $Cu_3SbSe_{4-x}S_x$ compounds.

Cu_3SbS_4 content (x)	Γ_M	Γ_S	Γ_T	κ_{calc} (80K)	κ_{exp} (80K)	κ_{calc} (300K)	κ_{exp} (300K)
0	0	0	0	12.42	13.43	2.96	2.91
0.4	0.01704	0.04120	0.05824	6.14	6.55	2.31	2.42
1.2	0.04516	0.08576	0.13091	4.45	4.17	1.94	1.80
2.0	0.06157	0.08810	0.14967	4.26	3.54	1.91	1.75
2.8	0.05982	0.06089	0.12071	4.85	3.27	2.08	1.79
3.6	0.03000	0.01997	0.04996	7.28	9.62	2.66	2.90
4.0	0	0	0	15.92	23.30	3.57	3.96

to produce the fit. There is considerably more deviation between the calculated and measured κ_L at 80K for $x > 0.5$, presumably because v_a and γ are not really constant with composition. In addition, extrinsic factors such as grain size and porosity will have a much larger effect on the magnitude of κ_L at low temperature, causing larger deviations from the model. The Deybe model fit to the temperature dependence of κ_L is also quite accurate (black lines, Figure 5.35). Regardless of the accuracy of the model, the data in Figure 5.36 show that the lattice thermal conductivity of Cu_3SbSe_4 can be reduced by as much as 40% at room temperature by introducing S impurities into the lattice. With the low initial hole concentrations still maintained for the $Cu_3SbSe_{4-x}S_x$ compounds, the hole concentration can be adjusted and optimized through doping.

The Cu_3SbSe_4-Cu_3SbS_4 solid solution is particularly attractive for thermoelectric applications due to the nature of the Se/S substitution. Slack [99] reviewed the characteristics of established thermoelectric semiconductor solid solutions and developed a set of criteria that should be met in order for a given solid solution to show high ZT. First, he identified an important parameter for all thermoelectric compounds, the weighted mobility, defined as:

$$U = \mu[m^*/m_0]^{3/2} \tag{5.15}$$

where μ is the carrier mobility, m^* is the carrier effective mass, and m_0 is the free electron mass (9.11×10^{-31} kg). In general, U can be used as a guideline to judge the potential of a new material for thermoelectric applications. The expression for ZT can be rewritten using the Wiedemann-Franz law ($\kappa_e = L_0\sigma T$):

$$ZT = \frac{(S/\sqrt{L_0})^2}{1+\left[\frac{\kappa_L}{L_0\sigma T}\right]} \tag{5.16}$$

which, when combined with the expressions for weighted mobility (equation 5.15) and electrical conductivity of a p-type semiconductor ($\sigma = pe\mu$ where p is the hole concentration), gives:

$$ZT = \frac{(S/\sqrt{L_0})^2}{1+\frac{1}{L_0 eT}\left[\frac{\kappa_L}{U}\right]\left[\frac{[m^*/m_0]^{1.5}}{p}\right]}\,. \tag{5.17}$$

The material-dependent parameters governing ZT are then U/κ_L, which is intrinsic to the chosen material, and $[m^*/m_0]^{1.5}/p$ which depends on doping level. Slack determined that in order to conserve U while reducing κ_L in a solid solution, the electronegativity difference (ΔX) between the host and impurity atoms should be as small as possible, ideally less than 0.05. The Se/S pair satisfies this criterion ($X(S) - X(Se) = 0.03$) whereas the Se/Te pair, more commonly used for thermoelectric materials, does not ($X(Se) - X(Te) = 0.15$). In addition, the Se/S pair should provide comparable phonon scattering to Se/Te since the mass difference is similar ($M^{Se} - M^{S} = 46.9$ versus $M^{Te} - M^{Se} = 48.64$) and the Se/S pair also has a large strain-field effect in $Cu_3SbSe_{4-x}S_x$ as discussed above.

To determine the most suitable compositions for thermoelectric applications, U/κ_L values

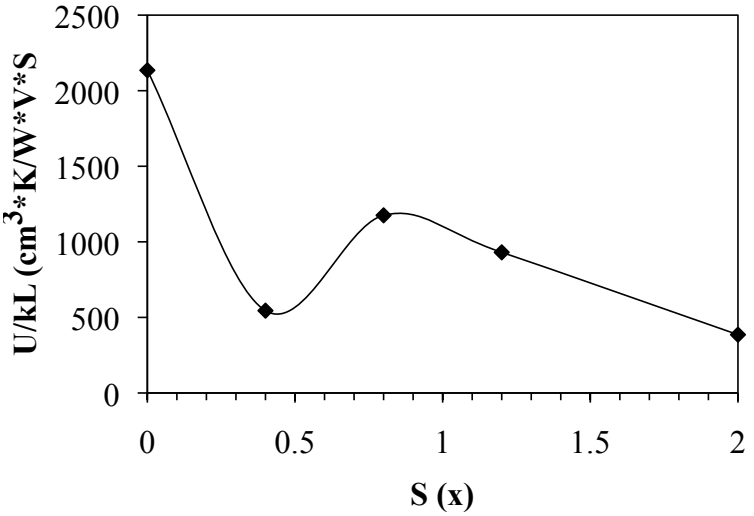

Figure 5.37: Ratio of the weighted mobility (U) to lattice thermal conductivity (κ_L) versus composition in the $Cu_3SbSe_{4-x}S_x$ system for x≤2.

were calculated for samples with x≤2. Values of m^*/m_0 were extracted from Hall and Seebeck coefficient measurements using the following expressions [100]:

$$p = \frac{4}{\sqrt{\pi}} \left(\frac{2\pi m^* kT}{h^2} \right)^{3/2} F_{1/2}(\eta) \tag{5.18}$$

and

$$S = \pm \frac{k}{e} \left(2\frac{F_1(\eta)}{F_0(\eta)} - \eta \right) \tag{5.19}$$

where p is the hole concentration, S is the Seebeck coefficient, and $F_n(\eta)$ are Fermi integrals of order n evaluated at the reduced Fermi energy η. The resulting values of U/κ_L are shown in Figure 5.37. While none of the x>0 compounds match the U/κ_L value of Cu_3SbSe_4, it is clear that the x = 0.8 and 1.2 compositions are the most promising from the $Cu_3SbSe_{4-x}S_x$ system; their room temperature properties are listed in Table 5.5 .

Both Ge and Sn doping on the Sb site were again evaluated for the $Cu_3SbSe_{4-x}S_x$ compounds,

although in this case the addition of Sn caused a more drastic decrease in hole mobility and was not explored further. Doping studies with Ge on the Sb site were completed for compounds with x = 0.8 and x = 1.2, producing compounds of the form $Cu_3Sb_{1-y}Ge_ySe_{1-x}S_x$. The room temperature properties of the compounds studied are given in Table 5.5

Table 5.5: Room temperature properties of the $Cu_3Sb_{1-y}Ge_ySe_{4-x}S_x$ compounds.

Composition	Hole Concentration ($\times 10^{19}$ cm^{-3})	Hole Mobility (cm^2/V*s)	Seebeck Coefficient (μV/K)	Electrical Resistivity (mΩ*cm)	Thermal Conductivity (W/m*K)	Effective Mass (m^*/m_0)
x=0.8, y=0	0.0765	36.0	449	230	2.2	0.83
x=0.8, y=0.02	14.02	15.4	146	2.89	1.7	2.19
x=0.8, y=0.03	19.39	17.1	124	1.89	1.94	2.22
x=1.2, y=0	0.0711	26.0	445	340	1.8	0.77
x=1.2, y=0.02	12.78	17.8	142	2.75	1.88	2.00
x=1.2, y=0.03	20.32	14.8	127	2.08	1.88	2.33

Doping with 2% and 3% Ge increased the hole concentration to approximately 1.3×10^{20} cm^{-3} and 2.0×10^{20} cm^{-3} respectively, independent of S content, resulting in similar Seebeck coefficients for the y=0.02 and 0.03 samples (Figure 5.38). The doped samples have slightly lower mobility than the undoped samples due to ionized impurity scattering, but the mobility remains relatively constant with x, as evidenced by the similar electrical resistivity for the y=0.02 and 0.03 samples (Figure 5.38). The total thermal conductivity (Figure 5.39) follows a T^n temperature dependence, where $n \sim$ -0.5 at low temperature ($T \leq$300K) and $n \sim$ -1 at high temperature ($T >$300K). The change in temperature dependence arises because at low temperature phonon-impurity scattering dominates and weakens the temperature dependence whereas at high temperature phonon-phonon scattering dominates and phonon-impurity scattering is essentially constant, resulting in the characteristic T^{-1} temperature dependence.

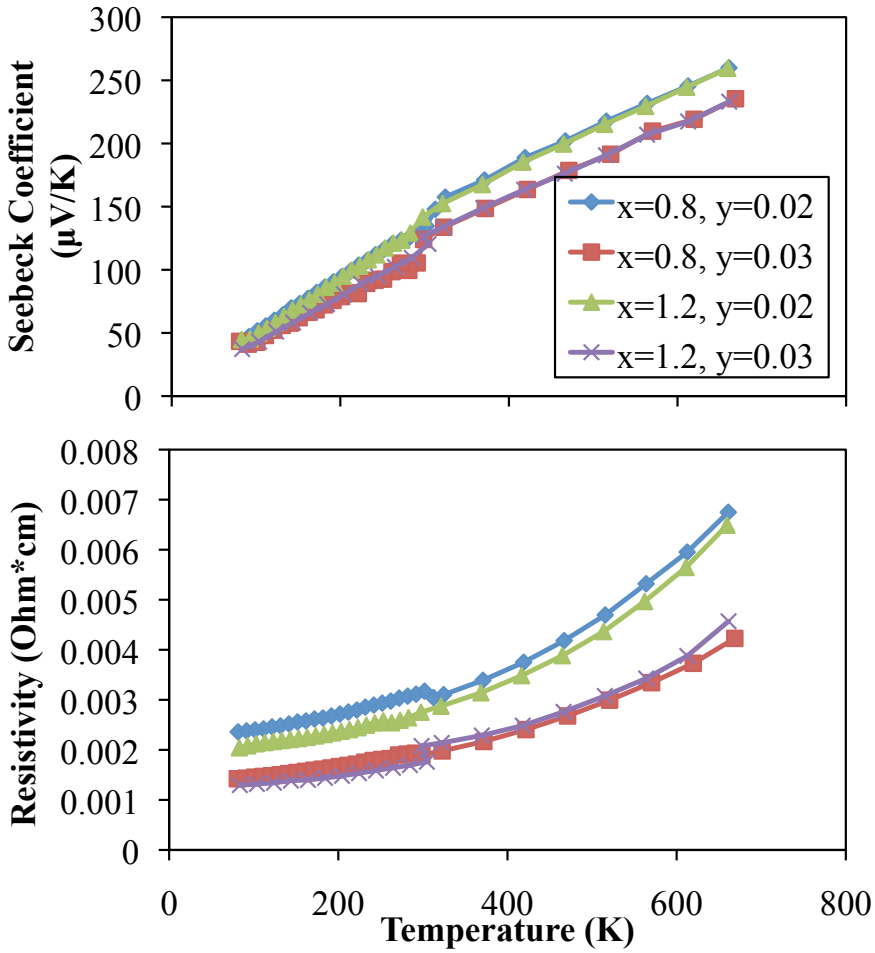

Figure 5.38: Temperature dependence of the Seebeck coefficient and Electrical resistivity of the $Cu_3Sb_{1-y}Ge_ySe_{4-x}S_x$ compounds

The electronic contribution to the thermal conductivity (κ_e) was again calculated from the Weidemann-Franz law, but with Lorentz numbers (L_0) estimated for each sample according to [100]:

$$L_0 = \frac{k}{e}^2 \frac{3F_0(\eta)F_2(\eta) - 4F_1^2(\eta)}{f_0^2(\eta)} \tag{5.20}$$

where the reduced Fermi energy η is estimated from the Seebeck coefficient data given in Table 5.5 using equation 5.19. The calculated high temperature lattice thermal conductivity ($\kappa_L = \kappa_T - \kappa_e$)

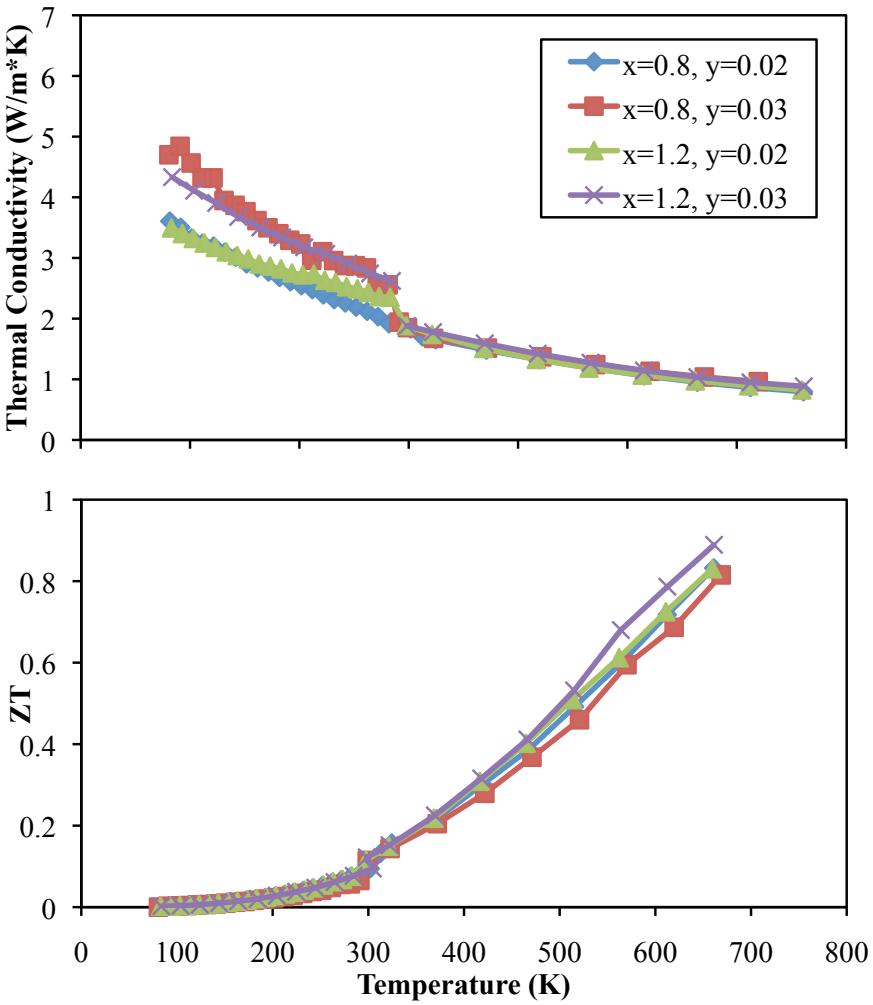

Figure 5.39: Temperature dependence of the thermal conductivity and dimensionless thermoelectric figure of merit of the $Cu_3SbSe_{4-x}S_x$ compounds

is shown in Figure 5.40. κ_L is approximately equal for all samples and independent of x, and agrees quite well with the estimate obtained from the Debye model, calculated following the procedure described above for the x=1.2 composition using γ=1.3 (dashed line, Figure 5.40). The κ_L for the x>0 compounds is approximately 40% lower than that of the x=0, y=0 compound over the entire temperature range due to constant phonon-impurity scattering, and approaches 0.6 W/m*K at 650K for all samples. Using the average measured specific heat (C = 1.85 J/cm^{3}K) and the reported longitudinal sound velocity for Cu_3SbSe_4 (v = 3.0 km/sec [85]), it is possible to estimate the phonon mean free path (ℓ) at 650K using the expression [44]:

$$\kappa_L = \frac{1}{3} C v \ell. \tag{5.21}$$

The estimated phonon mean free path at 650K is $\sim$ 0.3 nm, only slightly larger than the average interatomic spacing in Cu_3SbSe_4 and Cu_3SbS_4 (0.246 nm and 0.234 nm respectively), which represent the minimum possible value of ℓ in these compounds.

The relatively large power factor and low thermal conductivity in these compounds leads to very respectable ZT values at high temperature, approaching 0.9 at 650K (Figure 5.39). All of the compounds studied here have ZT $>$ 0.8 at 650K, and the maximum value is ZT = 0.89 for the x=1.2, y=0.03 sample. These values are comparable with the best performing p-type thermoelectric materials at this temeprature, including PbTe [101], double-filled skutterudites [102], and the $AgSbTe_2$-GeTe (TAGS) compounds [103].

5.7.3 Summary

The Cu_3SbSe_4-Cu_3SbS_4 system has been studied for the first time. These two compounds form a complete solid solution, maintaining the tetragonal crystal structure of the end compounds at all compositions. Samples prepared by quenching from 600°C and annealing at 350°C are single-phase with hole concentrations on the order of 10^{18} cm^{-3} at room temperature. The hole concen-

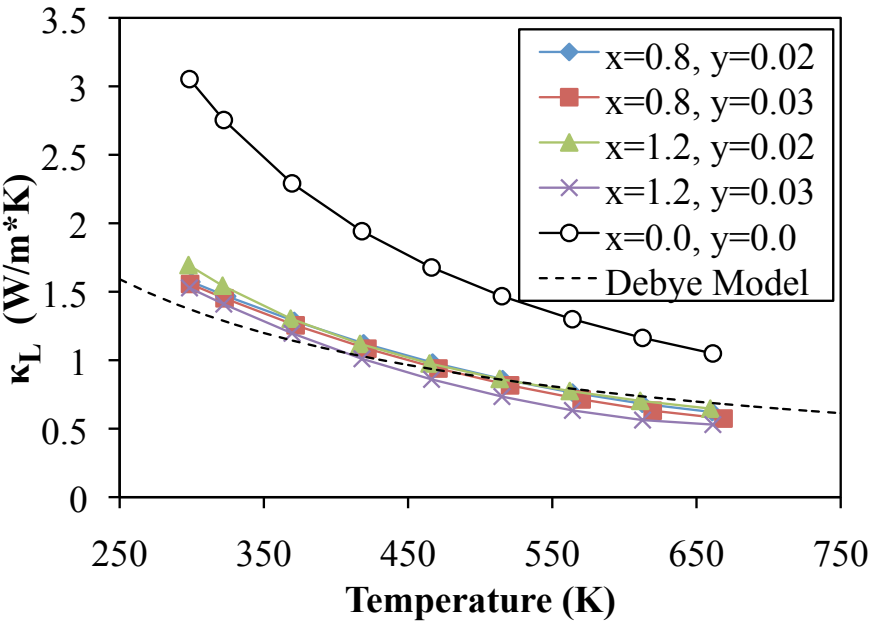

Figure 5.40: High temperature lattice thermal conductivity of the $Cu_3SbSe_{4-x}S_x$ compounds. Dashed line indicates κ_L calculated from the Debye model for x=1.2 using γ=1.3.

tration increases slightly with increasing S content, presumably due to an increase in the number of intrinsic defects in the material resulting from S loss during synthesis. The hole mobility also decreases with increasing S content due to neutral impurity scattering, but remains above 10 $cm^2/V*s$ at all compositions.

Substitution of S for Se in Cu_3SbSe_4 is ideal for improving its thermoelectric performance because it produces a substantial reduction in κ_L without significantly degrading the electronic properties of the material. The κ_L of Cu_3SbSe_4 is reduced by as much as 70% at low temperature and 40% at room temperature and above by introducing S impurities into the lattice. Using the Debye model to fit the experimental κ_L data revealed that both the atomic mass and size difference between Se and S contribute to increased phonon scattering in the material. The small electronegativity difference between Se and S helps to conserve the carrier mobility at intermediate compositions in the $Cu_3SbSe_{4-x}S_x$ system, such that the electronic properties are not significantly

degraded. Both Ge and Sn are effective p-type dopants, although Sn doping tends to give lower hole mobility and was not extensively explored. Doping with 3% Ge on the Sb site gives rise to a thermoelectric power factor of 12 μW/cm*K^2 at 650K. The thermoelectric performance of Cu_3SbSe_4 is optimized with 3% Ge on the Sb site and 30% S on the Se site, which gives ZT = 0.9 at 650K.

The $Cu_3Sb_{1-y}Ge_ySe_{4-x}S_x$ compounds offer the same advantages as Cu_3SbSe_4 in that they do not contain toxic or expensive elements or complex nanostructures. The melting temperature is increased slightly with S content, which allows for higher operating temperatures. With further optimization of the doping level and S content, ZT values greater that unity are likely, making these compounds attractive for thermoelectric power generation at intermediate temperatures.

5.8 Cu-Based Diamond-Like Ternary Compounds: Conclusions and Future Work

From this portion of the work it is concluded that ternary variations on the elemental diamond structure semiconductors are viable candidates for thermoelectric power generation applications. The diamond-like Cu-based ternary compounds are derived schematically from the group IV elemental semiconductors through successive atomic substitutions, which increase the size and complexity of the unit cell and lead to little-known narrow band gap ternary semiconductors with low lattice thermal conductivities. The two-fold ternary derivatives having compositions of the form I-III-VI_2 are not well suited for thermoelectric applications due to their relatively wide band gaps and high thermal conductivity, and thus were not studied here. The three and four-fold ternary derivatives, having compositions of the form I_2-IV-VI_3 and I_3-V-VI_4, were the focus of this work. From these systems, compounds with I = Cu and VI = Se were found to exist as single phase compounds with reported band gaps in the range appropriate for thermoelectric applications.

Cu_2SnSe_3 exists in both low and high temperature modifications, with the high temperature cubic phase corresponding to a disordered arrangement of Cu and Sn atoms and the low temperature monoclinic phase corresponding to an ordered arrangement. The quenching procedure required to form the cubic phase of Cu_2SnSe_3 results in extreme brittleness in the material and thus transport property measurements were conducted exclusively on slow-cooled samples. Undoped samples were always p-type and exhibited a wide range of hole concentrations, 10^{18} to 10^{20} cm^{-3} at room temperature, likely due to self-doping via intrinsic defects. Both Ga and In are effective p-type dopants in Cu_2SnSe_3, although large fluctuations in the hole concentration were still present in doped samples. Lengthy annealing treatments and minor changes in composition did not improve the reproducibility of the samples.

Cu_2SnSe_3 forms a complete solid solution with Cu_2GeSe_3, maintaining a single phase at all compositions. For compounds of the form $Cu_2Sn_{1-x}Ge_xSe_3$, a structural transformation occurred

at either x=0.5 or x=0.7 depending on the synthesis procedure. For quenched samples, the cubic structure of Cu_2SnSe_3 was maintained until x=0.7 before a transition to the orthorhombic Cu_2GeSe_3 lattice occurred. For slow-cooled samples the transition from monoclinic to orthorhombic symmetry occurred at x=0.5. The lattice thermal conductivity decreases slightly with increasing x and can be approximated quite accurately using the Debye model. An analysis of the phonon impurity scattering parameter (Γ) revealed that the decrease in lattice thermal conductivity is almost exclusively due to the atomic mass difference between Sn and Ge with no contribution from lattice strain arising from the atomic radius mismatch. The thermoelectric properties of Cu_2SnSe_3 were not improved by adding Cu_2GeSe_3.

The Cu_2SnSe_3-Cu_2SnS_3 system also forms a complete solid solution, in agreement with previous results [68]. The monoclinic structure of Cu_2SnSe_3 was maintained at all compositions (only slow-cooled samples were investigated). The lattice thermal conductivity is reduced by approximately 40% at room temperature upon the addition of Cu_2SnS_3 due to mass and strain field fluctuations in the lattice. Both Ga and In are effective p-type dopants, and the thermoelectric performance was optimized for 7.5% In doping on the Sn site. Large sample-to-sample hole concentration variations still plague these compounds, along with a mechanical instability near 800K that causes softening of the sample.

Cu_2GeSe_3 maintains an orthorhombic structure when quenched or slow-cooled, indicating a strong preference for ordering among the Cu and Ge atoms. The ability of this compound to accommodate a wide range of Ge concentration was investigated, with an emphasis on the structural transformations and the effect on the transport properties. $Cu_2Ge_{1+x}Se_3$ compounds with negative values of x (Ge deficiency) showed a gradual transition from orthorhombic (x=0) to monoclinic (x=-0.15) symmetry accompanied by a transition from semiconducting to metallic transport behavior. This indicates that a Ge deficiency in Cu_2GeSe_3 has a strong doping effect, but it was found that it does not improve the thermoelectric performance. The addition of excess Ge (positive x values) induced a transition from orthorhombic to cubic symmetry at x=0.55, with a cubic

lattice being maintained for $0.55 \leq x \leq 1.0$. The lattice thermal conductivity decreased strongly with increasing Ge content, which suggests that these compounds are actually a solid solution. $Cu_2Ge_{1.55}Se_3$ and elemental Ge have the same crystal structure and similar lattice constants, and an analysis of the lattice constant change, lattice thermal conductivity reduction, and average composition (determined by EDS) strongly indicates a solid solution. The solubility limit of Ge in Cu_2GeSe_3 occurs at x=1.2, at which point large Ge-rich regions precipitate out. Doping studies on the excess Ge compounds were largely unsucessful and mainly frustrated by the already large hole concentrations in the undoped compounds.

Cu_3SbSe_4 was found to exist only with an ordered tetragonal structure, with no high temperature disordered phase possible. Single phase samples were obtained by quenching, although large hole concentration gradients were found in quenched samples. Annealing the quenched samples at 300-350°C in the same ampoules produced samples with hole concentrations on the order of 10^{18} cm^{-3} with good reproducibility, presumably due to homogenization during the annealing procedure. Doping with Ge or Sn on the Sb site systematically varied the hole concentration and optimized the thermoelectric power factor near 16 $\mu W/cm*K^2$ at 630K. The lattice thermal conductivity approached 1 W/m*K at 630K, resulting in ZT values near 0.7, competitive with some of the best p-type thermoelectric materials.

The Cu_3SbSe_4-Cu_3SbS_4 system forms a complete solid solution with the tetragonal structure of Cu_3SbSe_4 maintained at all compositions. The lattice thermal conductivity is decreased by as much as 40% at room temperature due to atomic mass and strain field fluctuations. The hole mobility remains relatively large (above 20 $cm^2/V*s$) at all compositions due to the small electronegativity difference between Se and S. The reduction in lattice thermal conductivity is realized even at high temperatures, and the minimum possible value is reached at approximately 650K. Ge-doped samples achieved ZT=0.89 at 650K, in the range of many state of the art p-type thermoelectric materials.

There are numerous opportunities for future work on these compounds. The two-fold ternary

derivates Cu_2SnSe_3 and Cu_2GeSe_3 would benefit from electronic band structure and defect calculations, which could provide a means of understanding the unexplained variability of the hole concentration in these compounds. If the hole concentration can be controlled, the $Cu_2SnSe_{1-x}S_x$ are promising as p-type thermoelectric materials. Band structure, defect, and phonon dispersion calculations are currently underway for Cu_3SbSe_4. Equally important to understanding electrical and thermal transport in these compounds is evaluating their mechanical properties. Many of the compounds studied in this work are quite brittle, and poor mechanical properties would likely prevent them from being widely used in thermoelectric applications despite their impressive performance and environmental benefits.

6 The Effect of Lone Electron Pairs on the Lattice Thermal Conductivity of Group VA Chalcogenides

In the preceding chapters, the discussion has focused primarily on the synthesis, characterization, and optimization of Cu-based diamond-like semiconductors for thermoelectric applications. These compounds all possess low κ_L at room temperature which then increases rapidly with decreasing temperature due to vanishing phonon-phonon interactions, as is typical for a crystalline material. More interesting for thermoelectric applications is the case of glass-like thermal conductivity in a crystalline material, where the phonon mean free path is limited to its minimum possible value even at low temperature. This phenomenon occurs in $AgSbTe_2$, one of the motivating factors for this work, and has been reported in relatively few other compounds.

In characterizing the Cu-based ternary systems for this work, namely the Cu-Sb-Se and Cu-Bi-Se systems, several compounds that exhibited glass-like thermal conductivity were found. The common thread among these compounds is that they all contain a group V element which is nominally in the trivalent (+3) state, meaning two fewer electrons per atom are lost than one would naively expect considering only the group number, leaving two valence electrons that do not participate in bonding. Morelli *et. al.* indicated that the "non-bonding" or "lone-pair" electrons around Sb in $AgSbTe_2$ could have an effect on the lattice thermal conductivity [44], but concrete evidence of a relation between the two is absent from the literature. The present chapter delves deeper into the effect of lone electron pairs (LEPs) on the physical properties of semiconductors, in particular κ_L, and how this could be used as a part of the selection criteria for new thermoelectric materials.

6.1 Background and Motivation

The transport of heat in crystalline solids has long been a topic of interest in solid-state physics. Thermal energy is conducted primarily by electrons and phonons in most materials, with the rel-

ative contributions of each determined by the physical properties of the crystal. The electronic contribution to the thermal conductivity of a given material, for instance, is directly proportional to its electrical conductivity as defined by the Wiedemann-Franz law. The electronic contribution is negligible in insulators and many semiconductors, but the phononic contribution is always present in any solid, exhibiting a surprisingly large range of values. Debye studied heat transport by lattice phonons in 1912 [104] and to this day the lattice thermal conductivity of a vast array of crystalline materials can be estimated, to a first approximation, using some form of the Debye model.

An interesting problem arises when one encounters a material whose lattice thermal conductivity cannot be explained using conventional phonon transport theory. Such is the case for ordered crystals that exhibit minimum thermal conductivity behavior at ordinary temperatures. In developing his famous PGEC (phonon glass electron crystal) concept for thermoelectric materials, Slack [99] showed that κ_L must approach the minimum possible value in a given material in order to obtain very large ($>$1.5) ZT values. The concept of "minimum thermal conductivity" was first described by Slack many years earlier [45], which he defined as the case where all phonons are scattered so frequently that the average mean free path is on the order of one phonon wavelength. The minimum phonon mean free path, as pointed out by Roufosse and Klemens [105], is on the order of one interatomic spacing. Cahill *et. al.* later experimentally confirmed the "minimum thermal conductivity" concept by studying a wide range of materials with glass-like thermal conductivity, none of which exhibited κ_L much lower than the κ_{min} estimated using a modified Einstein model. It is not uncommon for κ_L of an ordered crystalline material to approach κ_{min} near its melting temperature due to phonon-phonon interactions alone, however similar behavior near room temperature is quite rare. The underlying mechanism behind glass-like thermal conductivity in ordered crystals at low temperatures is not well understood; based on the results of Slack and Cahill there must be an intrinsic phonon scattering process that limits the mean free path over the entire phonon spectrum. Extrinsic modifications such as introducing substitutional impurities cannot produce glass-like phonon scattering. Obviously, a better understanding of such intrinsi-

cally limited κ_L is of paramount importance for the design of high performance thermoelectric materials.

The existence of glass-like thermal conductivity in the rocksalt structure I-V-VI_2 compounds where I = Ag, V = Sb or Bi and VI = Se or Te was first reported many years ago by Hockings [36]. Zhuze [34] reported linear thermal expansion coefficients in excess of 20 ppm for these compounds, indicating a high degree of anharmonicity in the crystal lattice. Petrov and Shtrum [37] noted the large difference in thermal conductivity and thermal expansion between the chalcopyrite I-III-VI_2 compounds and the I-V-VI_2 compounds, which they attributed to differences in interatomic bonding. In particular, they hypothesized that the interaction of nonbonding electrons around the nominally trivalent group V atoms contribute to a large anharmonicity in the I-V-VI_2 lattice which is not present in the sp^3 hybridized I-III-VI_2 compounds where all valence electrons participate in bonding. Recently Morelli *et. al.* came to a similar conclusion for the case of $AgSbTe_2$ versus $AgInSe_2$, and showed that the phonon mean free path in $AgSbTe_2$ is limited to the minimum possible value even at cryogenic temperatures [44]. Based on specific heat measurements and the reported thermal expansion they estimated the Grüneisen parameter of $AgSbTe_2$ to be 2.05, which is a large value compared to most crystalline materials with simple crystal structures. This reaffirms that $AgSbTe_2$ has a high degree of lattice anharmonicity since the Grüneisen parameter is a direct measure of anharmonicity. Although the κ_L difference between $AgSbTe_2$ and $AgInTe_2$ is intuitively explained using the nonbonding electron argument of Petrov and Shtrum, no concrete evidence in favor of a relation between LEPs and lattice anharmonicity has been provided.

The valence electron configuration of Sb in both naturally occurring and synthetic compounds has long been a topic of interest in the field of solid-state chemistry. There is a large body of work devoted to the stereochemistry of Sb compounds, in particular relating the valence state of Sb to its local atomic environment [106]. Several recent studies have focused on the effect of Sb valence on atomic coordination and electronic properties in Sb chalcogenides [107] - [109], and provide experimental evidence relating the ”activity” of the Sb lone pair (the delocalization of the lone pair

from the Sb nucleus) to the Sb coordination environment. This relation, as will be discussed in the following sections, will be used to relate Sb valence state to κ_L.

The characterization of the Cu-Sb-Se system for the preceding chapters of this manuscript revealed a unique opportunity to establish a link between Sb valence and κ_L. In this system there exist three ternary compounds, $CuSbSe_2$, Cu_3SbSe_3, and Cu_3SbSe_4, which contain Sb nominally in the +3, +3, and +5 valence state respectively, as determined by a simple charge-balance analysis. Initial analysis of Cu_3SbSe_3 versus Cu_3SbSe_4 revealed a glass-like thermal conductivity for the former compound and a crystalline-like thermal conductivity for the latter, as shown in Figure 6.1 [110]. The glass-like thermal conductivity in Cu_3SbSe_3 was again attributed to increased lattice anharmonicity arising from the interaction between the LEPs around Sb^{3+} and neighboring atoms. Using the relation between Sb valence and local atomic environment, the available structural data on the Cu-Sb-Se ternary compounds [111], [72], [112], and the lattice thermal conductivity data for Cu_3SbSe_3 and Cu_3SbSe_4 [110] as well as new data for $CuSbSe_2$, a relationship between Sb valence and lattice thermal conductivity can now be established.

6.2 Experimental

The synthesis procedure for Cu_3SbSe_4 has already been described in section 5.5.1. Synthesis of Cu_3SbSe_3 and $CuSbSe_2$ followed a similar procedure, although obtaining single phase samples of these compounds proved challenging. Samples of $CuSbSe_2$ were prepared by quenching from 900°C in room temperature water and also by slow cooling the melt from 900°C to room temperature. Samples of Cu_3SbSe_3 were prepared by quenching from 900°C into an ice water bath. After quenching the Cu_3SbSe_3 samples were annealed in the same ampoules at 400°C for 5 days. All of the Cu-Sb-Se samples reported here were vibratory ball milled under argon for 30 minutes, sieved (-100 mesh), and hot pressed at 400°C for 30 minutes using 70 MPa of pressure.

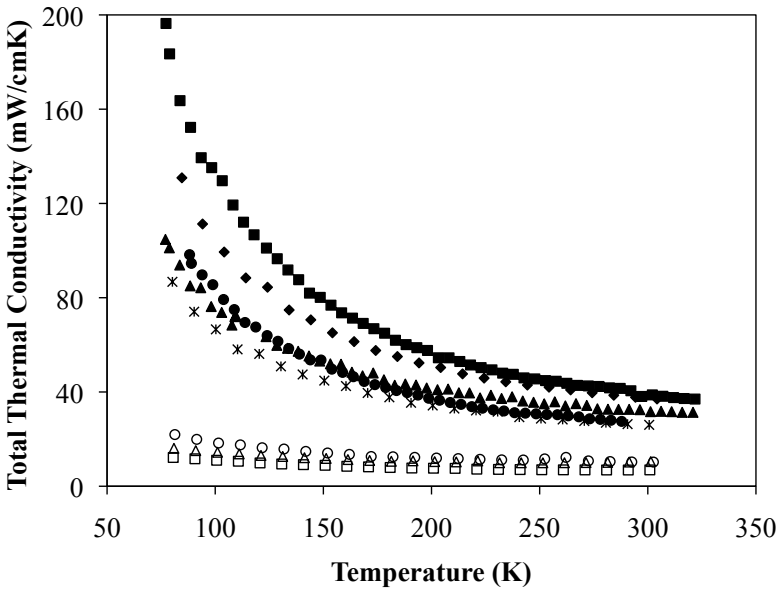

Figure 6.1: Temperature dependence of the thermal conductivity of Cu_3SbSe_3 (open symbols) and Cu_3SbSe_4 (closed symbols). The electronic contribution is negligible for all samples.

6.3 Results and Discussion

6.3.1 Phase Purity of $CuSbSe_2$ and Cu_3SbSe_3

The phase purity of $CuSbSe_2$ and Cu_3SbSe_3 were investigated using XRD and SEM (ORNL). Slow cooled samples of $CuSbSe_2$ contained a single phase with an orthorhombic structure (space group *Pnma*, a = 0.6014 nm, b = 0.37882 nm, c = 1.4472 nm), in agreement with single crystal studies [112]. Slow cooled samples of Cu_3SbSe_3 always contained multiple phases, and thus quenching was used exclusively for this compound.

SEM backscattered electron images of separate samples of Cu_3SbSe_3 quenched from 500°C and 900°C are shown in Figure 6.2. It is clear that these samples are multiphase, but the relative amounts of the secondary phases are quite different (see Table 6.1. X-ray mapping (Figure 6.3) revealed the dark regions to be Cu-rich, the light regions to be Sb-rich, and the distribution of selenium to be relatively uniform. The sample quenched from 900°C contains considerably less of

Table 6.1: Relative amounts of phases present in Cu_3SbSe_3 samples quenched from 500°C and 900°C in room temperature water.

Synthesis method	Phases present		
	$Cu_{2-x}Se$	Cu_3SbSe_3	$CuSbSe_2$
Quenched from 500°C	30%	47%	24%
Quenched from 900°C	11%	22%	68%

the unwanted $Cu_{2-x}Se$ and $CuSbSe_2$ phases compared to the sample quenched from 500°C, likely due to the faster cooling rate achieved upon quenching from higher temperature.

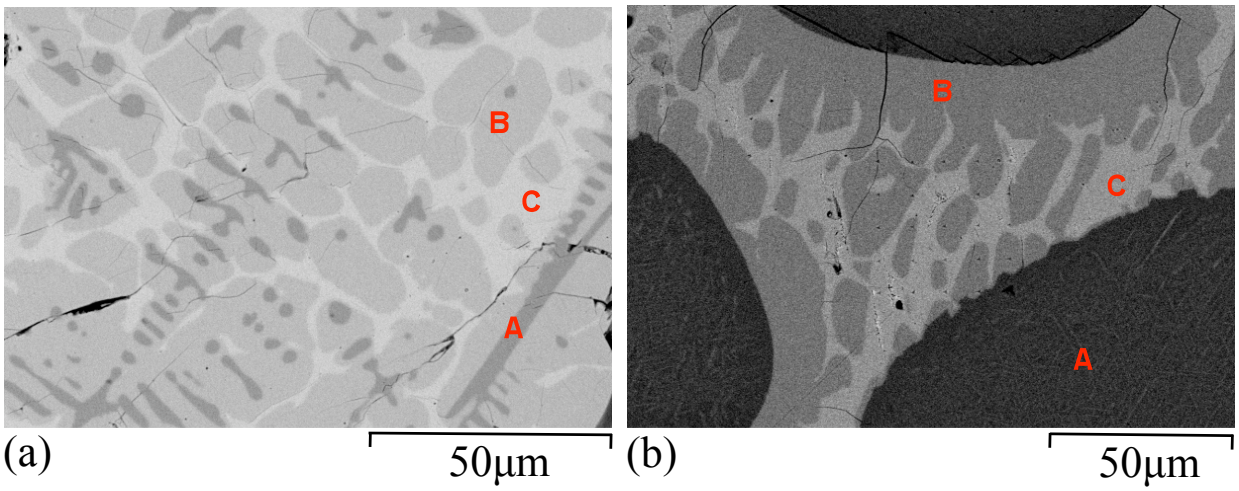

Figure 6.2: Backscattered electron images of Cu_3SbSe_3 quenched from (a) 900°C and (b) 500°C into room temperature water with three phases labeled: A = $Cu_{2-x}Se$, B = Cu_3SbSe_3, C = $CuSbSe_2$.

Based on the above results, subsequent Cu_3SbSe_3 samples were prepared by quenching from 900°C into an icewater bath in order to achieve a faster cooling rate. The icewater quenched samples were found to have a fine dendritic microstructure composed of primarily Cu_3SbSe_3 and $CuSbSe_2$. Annealing at 400°C for 5 days resulted in nearly single phase Cu_3SbSe_3 with only small inclusions of $CuSbSe_2$, and these samples were used for thermal conductivity measurements. The

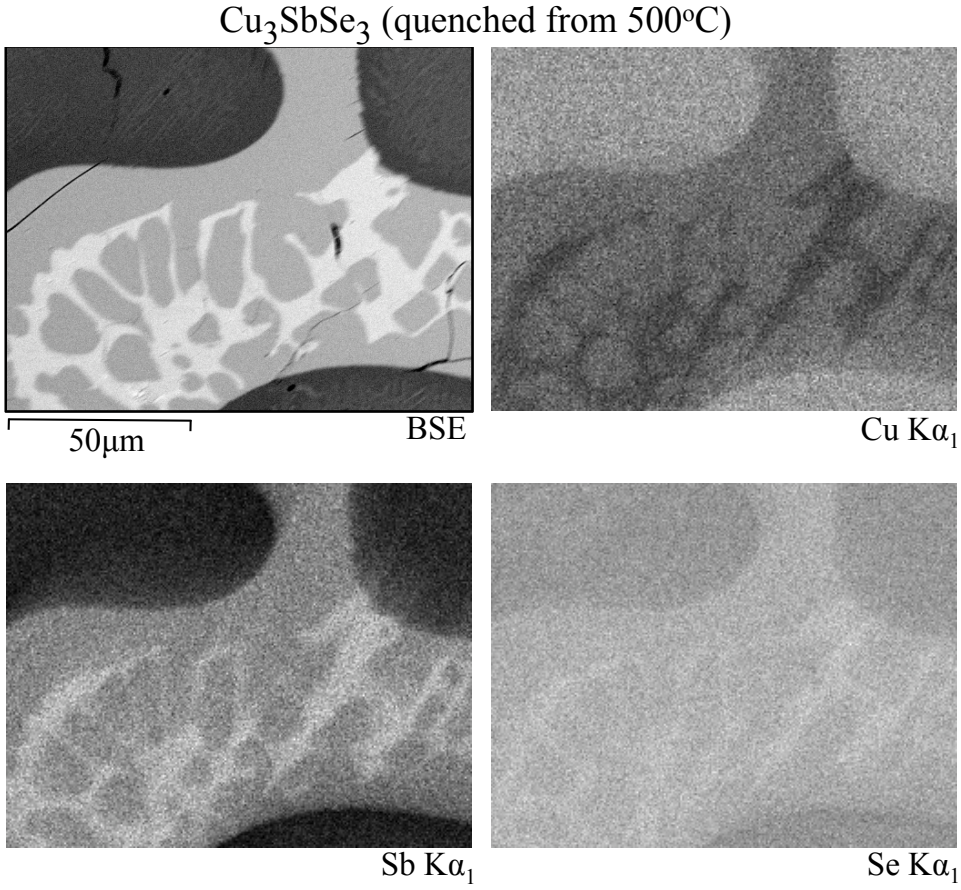

Figure 6.3: X-ray mapping on a similar region of the sample shown in Figure 6.2(b).

X-ray diffraction pattern of a Cu_3SbSe_3 sample that was quenched from 900°C into icewater and annealed at 400°C for 5 days is shown in Figure 6.4. All of the peaks match with the references lines from the JCPDS database, indicating that the sample is composed primarily of Cu_3SbSe_3.

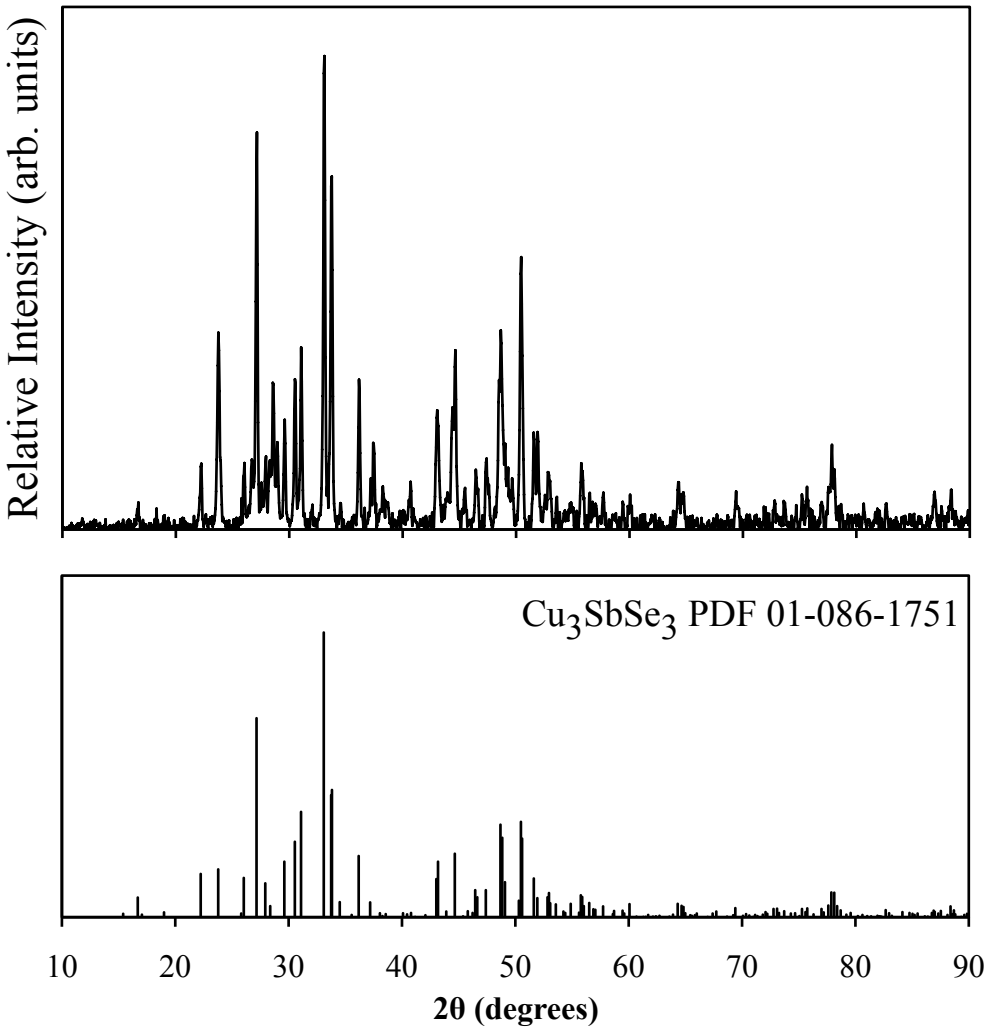

Figure 6.4: X-ray diffraction pattern of a Cu_3SbSe_3 sample quenched from 900°C into icewater and annealed at 400°C for 5 days.

6.4 The Lattice Thermal Conductivity of $CuSbSe_2$, Cu_3SbSe_3, and Cu_3SbSe_4

The initial interest in $CuSbSe_2$ and Cu_3SbSe_3 stemmed from the promising thermoelectric properties of Cu_3SbSe_4, but it was found that the former compounds are not well suited for thermoelectric applications and the results will not be discussed here. In the process of characterizing these compounds, however, it was noticed that the thermal conductivity behavior of each was very different despite their similar compositions. Figure 6.5 shows the temperature dependence of κ_L (the electronic contribution is less than 1% in these undoped samples) of the Cu-Sb-Se compounds. Intuitively one would expect these three compounds to have very similar thermal conductivity since their average atomic masses are nearly the same and none of them possesses a complex crystal structure. The only reasonable explanation for this difference is that there must be a phonon scattering mechanism inherent in these materials that is acting with increasing strength as the composition changes from Cu_3SbSe_4 to $CuSbSe_2$ to Cu_3SbSe_3. These results are consistent with the hypothesis that the LEP around Sb contributes to anharmonicity in the lattice, but since Sb is nominally trivalent (+3) in both $CuSbSe_2$ and Cu_3SbSe_3 the difference in κ_L between these two compounds is not immediately clear.

To better understand the thermal conductivity behavior of these compounds, the subtle differences in their crystal structures will be examined. Of particular interest is the coordination environment of Sb, which has been studied extensively in relation to LEPs.

6.5 The Effect of Lone-Pair Electrons on the Coordination Environment of Sb

Trivalent Sb can adopt coordination numbers ranging from 3 to 6 depending on the bonding nature between Sb and the other atomic species present [106]. The coordination environment of Sb in $CuSbSe_2$, Cu_3SbSe_3, and Cu_3SbSe_4 is illustrated schematically in Figure 6.6. For Cu_3SbSe_4, Sb is coordinated by 4 selenium atoms with ideal tetrahedral $Se-Sb-Se$ bond angles of 109.5°, indi-

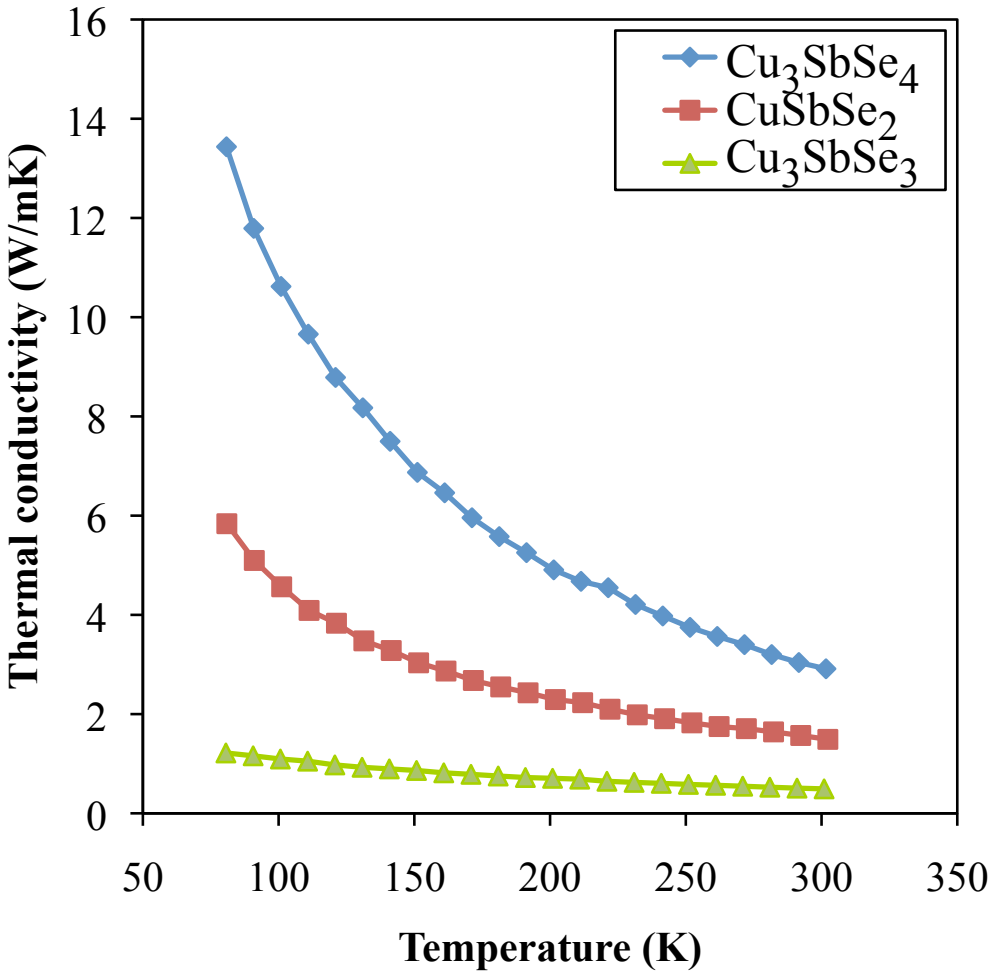

Figure 6.5: Temperature dependence of the lattice thermal conductivity of $CuSbSe_2$, Cu_3SbSe_3, and Cu_3SbSe_4.

cating sp^3 hybridization of the Sb valence electron orbitals. In this case, all of the valence electrons of Sb form bonds with neighboring Se atoms as indicated in Figure 6.6. For the case of $CuSbSe_2$, Sb is coordinated by 3 Se atoms in a pyramidal configuration with an average Se−Sb−Se bond angle of 95.24°. In this arrangement only the Sb 5p electrons participate in bonding with Se, leaving the Sb 5s electrons "free" to orient themselves along the missing vertex of the tetrahedra[1].

[1]The term "free" as used here does not imply that these electrons are free in the sense of conduction electrons in a semiconductor or metal; rather it is only meant to signify that they are capable of assuming a specific orientation about the Sb nucleus to which they belong

The configuration is similar for Cu_3SbSe_3 only the average Se−Sb−Se bond angle is 99.42°, intermediate to that of the other two compounds. Once again the Sb 5s lone pair electrons form a tetrahedron with the Sb 5p bonding electrons.

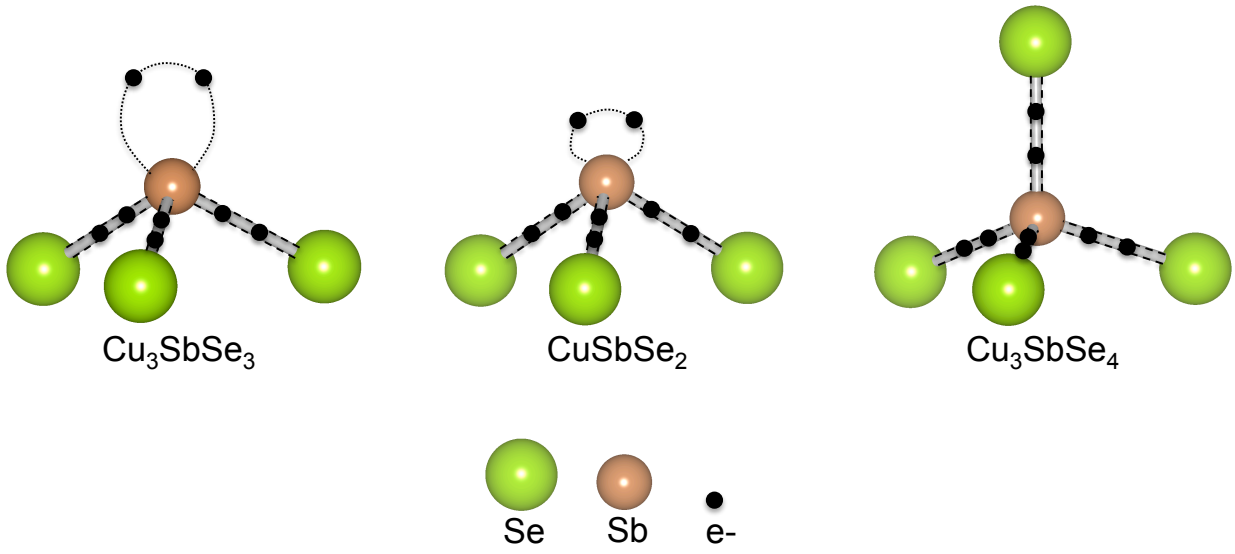

Figure 6.6: Local coordination environment of Sb in $CuSbSe_2$, Cu_3SbSe_3 and Cu_3SbSe_4. Shaded lines represent bonds, dotted ovals represent the approximate morphology of the LEP orbital.

The coordination environment of Sb in Cu_3SbSe_4 requires little interpretation as it is analogous to the well known group IV, III-V, and II-VI compounds. In $CuSbSe_2$ and Cu_3SbSe_3 on the other hand, Sb has the same coordination yet the Se−Sb−Se angle is quite different. This effect was studied by Wang and Liebau, who noted that the change in X−Sb−X bond angle (where X is a chalcogen atom) is related to the delocalization of the Sb 5s lone pair away from the Sb nucleus [109]. This phenomenon stems from the fact that the actual valence of Sb in a given compound is not necessarily purely trivalent or pentavalent, but rather a combination between these two extremes. For a purely pentavalent Sb compound, as in the case of Cu_3SbSe_4, all of the Sb valence electrons are completely delocalized from the Sb nucleus and form bonds that assume the ideal tetrahedral angle of 109.5°. For a purely trivalent compound, the Sb 5s electrons remain concentrated around the Sb nucleus thereby inducing a Coulombic repulsion with the bonding Sb

5p electrons, causing the X−Sb−X bond angle to approach 90°. As the actual Sb valence varies from +3 to +5 the 5s lone pair progressively retracts from the nucleus which weakens the repulsion and causes the bonding angle to increase. Wang and Liebau compiled X−Sb−X bond angles from the literature and derived an expression for the effective valence of Sb^{3+} in SbX_n polyhedra [109]:

$$^{eff}V_{Sb^{3+}}(\overline{\alpha}_i) = 3[1 + 0.0128(\overline{\alpha}_i - 90)] \tag{6.1}$$

where $\overline{\alpha}_i$ is the average X−Sb−X bond angle.

The difference in Se−Sb−Se bond angle between $CuSbSe_2$ and Cu_3SbSe_3 can now be interpreted as a difference in effective Sb valence state. $^{eff}V_{Sb^{3+}}$ = 3.2 for $CuSbSe_2$ while for Cu_3SbSe_3 $^{eff}V_{Sb^{3+}}$ = 3.36, indicating that the lone pair electrons are retracted farther from the Sb nucleus in Cu_3SbSe_3 than in $CuSbSe_2$, as illustrated in Figure 6.6. The main idea behind the relationship between lone pair electrons and low κ_L is that as atoms approach one another during thermal agitation, the wave functions of lone pair electrons will interact with those of electrons from nearby atoms causing increased anharmonicity in the lattice. The closer the lone pair electrons are to the Sb nucleus, the less chance they will have of interacting with electrons from adjacent atoms and the less they will influence the lattice thermal conductivity. The highest degree of anharmonicity should thus be achieved when the lone pair electrons are far removed from the Sb nucleus yet not participating in bonding, intermediate to the case of Sb^{3+} ($\overline{\alpha}_i$ = 90°) and Sb^{5+} ($\overline{\alpha}_i$ = 109.5°). This explains the thermal conductivity difference between the three Cu-Sb-Se compounds shown in Figure 6.5 and provides concrete evidence in favor of a relationship between Sb valence state and κ_L.

6.6 Generalization to Group VA Chalcogenides

The ternary compounds in the Cu-Sb-Se system provide a basis for the argument that lone-pair electrons can affect κ_L, but it remains to be seen whether or not this holds true for similar com-

pounds. If there exists a universal relationship between Sb valence state and lattice anharmonicity, then it should be possible to generalize the results of the Cu-Sb-Se compounds to other group VA chalcogenides. With this in mind, a comprehensive literature review of the crystal structures (in particular the group VA coordination environment) and room temperature κ_L values of binary and ternary group VA chalcogenides was conducted. Literature data are given in Table 6.2 for compounds of the form M_2-X_3 and A_i-M_j-X_k where M = As, Sb, or Bi, X = S, Se, or Te, and A = Cu, Ag, Tl, or an alkali metal. The average X−M−X bond angles were calculated from the bond angles of the nearest neighbor M−X atoms, which comprise the MX_n coordination polyhedra of interest. For compounds in which M is coordinated by more than 4 chalcogen atoms, bond angles $>109.5^\circ$(corresponding to chalcogen atoms on opposite sides of the M atom) were not included in the calculation.

The room temperature κ_L versus average X−M−X bond angle of 33 group VA chalcogenides are plotted in Figure 6.7 (for raw data see Table 6.2). The shaded region represents the range of minimum κ_L for these compounds, calculated from $\kappa_L = 1/3Cv\ell$ using the Dulong-Petit value for the specific heat (C), 3000 m/s for the phonon velocity (v) and the average interatomic distance for the phonon mean free path (ℓ). The minimum in κ_L between the smallest and largest X−M−X bond angle corroborates the trend observed in the Cu-Sb-Se system, but clearly there is not a singular value of $\overline{\alpha_i}$ that produces minimum κ_L. The broad minimum in κ_L values suggests there is more than one factor affecting κ_L with increasing $\overline{\alpha_i}$.

The data from Figure 6.7 (not including the compounds with ideal tetrahedral coordination and $\overline{\alpha_i}$ = 109.5°) are shown in Figure 6.8 separated according to the coordination number (CN) of the M atom. In each case, κ_L decreases nearly linearly with increasing $\overline{\alpha_i}$, and the rate of decrease (indicated by the dashed lines in Figure 6.8) increases with increasing CN. Figure 6.8 shows that the magnitude of κ_L depends not only on the retraction of the LEP from the nucleus of the M atom, but also the coordination environment of the M atom. When the M atom is surrounded by 6 or more chalcogen atoms (octahedral or greater coordination), the LEP assumes a spherical

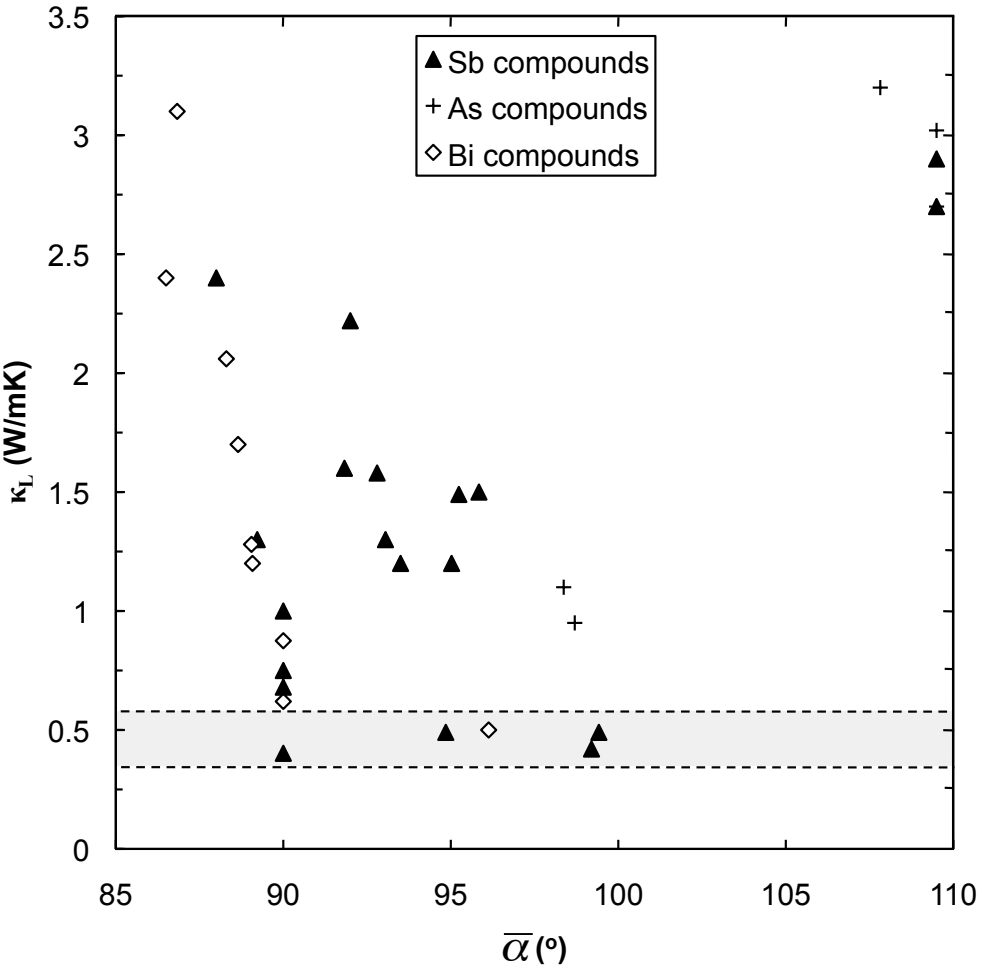

Figure 6.7: Lattice thermal conductivity versus average X-M-X bond angle of the group VA chalcogenides.

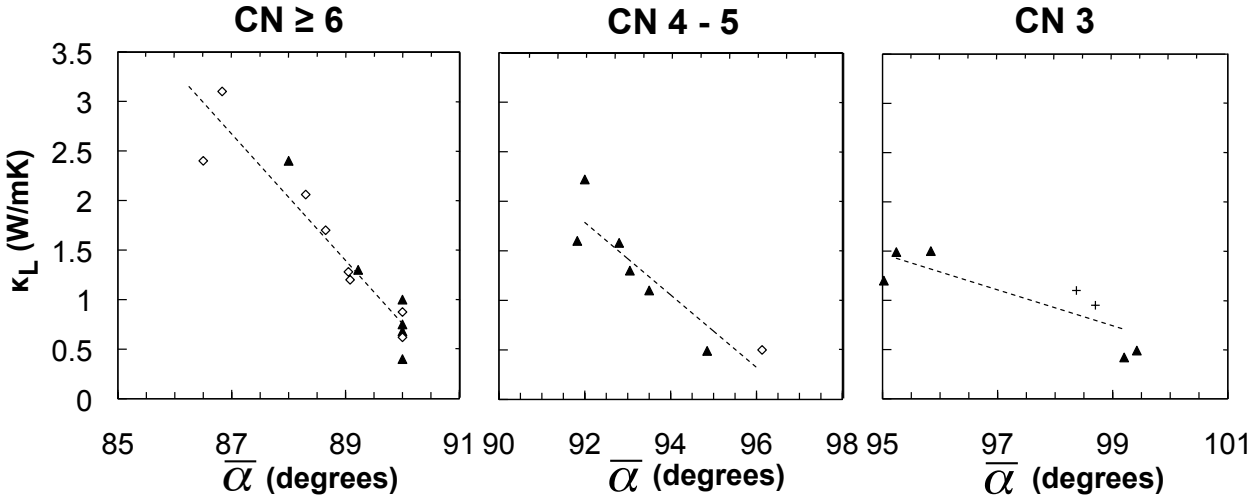

Figure 6.8: Lattice thermal conductivity versus average X-M-X bond angle of the group VA chalcogenides, separated according to the coordination number (CN) of the group V atom.

distribution around the M nucleus and even a small retraction of the LEP away from the M nucleus will result in an interaction with a neighboring chalcogen atom. Thus with increasing $\overline{\alpha_i}$, κ_L decreases rapidly (slope = -0.64) up to $\overline{\alpha_i} = 90^\circ$, which is the largest possible bond angle before the CN≥6 coordination environment becomes unstable. The crowded local environment of the M atom in the CN $\geq$ 6 configuration also explains why the sulfides in this group generally have lower κ_L than the tellurides despite their lower average atomic mass (see, for example, Sb_2S_3 versus Sb_2Te_3 and $AgSbS_2$ versus $AgSbTe_2$). The smaller S atoms lie closer to the central M atom (the average Sb X bond lengths for Sb_2S_3 and Sb_2Te_3 are 2.506 and 3.074 respectively) thus increasing the likelihood of an interaction with the LEP. This effect is also manifested in the κ_L difference between the monoclinic and NaCl-type phases of $AgSbS_2$; the latter has a lower κ_L (0.4 W/m*K) due to the crowded atomic environment of Sb (CN = 6) while the latter has κ_L = 0.49 W/m*K and CN = 5.

For CN = 4 - 5 there is more ”open space” around the M atom due to the loss of 1 - 2 coordinating chalcogen atoms, and thus a larger retraction of the LEP is required before interaction with neighboring atoms occurs. Certain compounds in this series such as $AgSbS_2$ and $CuBiS_2$ have,

strictly speaking, CN = 3 but an assessment of the M X bond lengths reveals three short bonds, two intermediate bonds, and one long bond, and are thus considered here to have CN = 5. In this arrangement, the LEP is stereochemically active and retracted from the M nucleus in the direction of the missing chalcogen atom(s). The absence of a complete octahedron around the M atom results in a more gradual decrease of κ_L with $\overline{\alpha_i}$ (slope = -0.37) due to less interaction between the LEP and surrounding chalcogen atoms.

For CN = 3 the LEP occupies the missing vertex of the tetrahedron and can move far away from the M nucleus without encountering a neighboring atom. The absence of nearby chalcogen atoms in this direction means that strong lattice anharmonicity will not be achieved until the LEP is far removed from the M nucleus, and indeed very low κ_L values are not observed in these compounds until $\overline{\alpha_i} \geq 98^\circ$. Clearly from the gap in $\overline{\alpha_i}$ values in Figure 6.7, the CN = 3 environment becomes unstable around $\overline{\alpha_i} = 100^\circ$. Compounds that have CN = 3 with $\overline{\alpha_i} \geq 100^\circ$will likely have extremely low κ_L, as in the case of Tl_3AsSe_3, which has $\overline{\alpha_i} = 118.7^\circ$and κ_L = 0.35 W/m*K at room temperature [130], [131].

6.7 Summary

It has been demonstrated that lone-pair electrons can produce minimum thermal conductivity behavior in group VA chalcogenides. Both the morphology of the lone-pair electron orbital and the coordination environment of the group VA atom affect the intensity of the anharmonic forces that are produced in the crystal lattice. Based on these results, the propensity of a given group VA chalcogenide compound to exhibit minimum thermal conductivity can be evaluated based solely on crystallographic data. For compounds with CN $\geq$ 6, an X−M−X bond angle close to $\overline{\alpha_i}$=90°is preferred, whereas for CN = 4-5 and 3 $\overline{\alpha_i}$ should be in the range of 95-96°and $\geq 99^\circ$respectively to achieve anomalously low κ_L. These guidelines could prove useful in identifying potential new compounds for thermoelectric applications as well as thermal barrier coatings.

Table 6.2: Properties of group VA chalcogenides taken from the literature (continues on next page)

Compound	Crystal Structure (Space Group)	CN	$\overline{\alpha_i}$ ($^\circ$)	κ_L at 300K (W/m*K)	References
Sb_2S_3	Orthorhombic (*Pnma*)	6	89.22	1.30	[113], [46]
Sb_2Se_3	Orthorhombic (*Pbnm*)	6	90.00	1.00	[109], [46]
Sb_2Te_3	Rhombohedral ($R\bar{3}m$)	6	88.00	2.40	[114], [46]
Bi_2S_3	Orthorhombic (*Pbnm*)	6	88.30	2.06	[115], [46]
Bi_2Se_3	Rhombohedral ($R\bar{3}m$)	6	86.50	2.40	[114], [46]
Bi_2Te_3	Rhombohedral ($R\bar{3}m$)	6	88.65	1.70	[114], [46]
$NaSbS_2$	Triclinic ($P\bar{1}$)	4	92.00	2.22	[109], [116]
$KSbS_2$	Monoclinic (*C2/c*)	4	92.80	1.58	[109], [117]
$KSbSe_2$	Triclinic ($P\bar{1}$)	4	93.05	1.30	[109], [116]
$RbSbS_2$	Triclinic ($P\bar{1}$)	4	91.83	1.60	[118], [116]
$CsSbS_2$	Monoclinic (*C2/c*)	3	95.02	1.20	[119], [116]
$CuAsSe_2$	Rhombohedral ($R\bar{3}m$)	4	107.82	3.2	[120], [46]
$CuSbS_2$	Orthorhombic (*Pnma*)	3	95.84	1.50	[112], [46]
$CuSbSe_2$	Orthorhombic (*Pnma*)	3	95.24	1.49	[112], [121]
$CuBiS_2$	Orthorhombic (*Pnma*)	5	96.13	0.50	[122], [46]
$AgSbS_2$	Monoclinic (*C121*)	5	94.85	0.49	[123], [46]
$AgSbS_2$	Cubic (*Fm3m*)	6	90.00	0.40	[124], [121]
$AgSbSe_2$	Cubic (*Fm3m*)	6	90.00	0.77	[34], [46]
$AgSbTe_2$	Cubic (*Fm3m*)	6	90.00	0.68	[34], [44]
$AgBiSe_2$	Cubic (*Fm3m*)	6	90.00	0.62	[34], [44]
$TlAsS_2$	Monoclinic (*P21/a*)	3	98.7	0.95	[125], [117]
$TlSbS_2$	Triclinic (*P1*)	4	93.50	1.20	[109], [117]
$TlBiS_2$	Rhombohedral ($R\bar{3}m$)	6	90.00	0.875	[126], [117]
Cu_3AsS_3	Orthorhombic (*Pnma*)	3	98.37	1.10	[123], [46]
Cu_3SbSe_3	Orthorhombic (*Pnma*)	3	99.42	0.49	[72], [121]
Tl_3SbS_3	Rhombohedral (*R3m*)	3	99.20	0.42	[127], [46]

Table 6.3: (continued)

Compound	Crystal Structure (Space Group)	CN	$\overline{\alpha_i}$ (°)	κ_L at 300K (W/m*K)	References
$K_2Bi_8Se_{13}$	Triclinic (*P1*)	4	86.83	3.10	[119], [128]
β-$K_2Bi_8Se_{13}$	Monoclinic (*P21/m*)	6	89.05	1.28	[128]
$AgBi_3S_5$	Monoclinic (*C2/m*)	6	89.08	1.2	[129]
Cu_3AsS_4	Orthorhombic (*Pmn21*)	4	109.5	3.02	[96],
Cu_3SbS_4	Tetragonal ($I\bar{4}2m$)	4	109.5	2.70	[96], [121]
Cu_3AsSe_4	Cubic (*Pm3m*)	4	109.5	2.70	[58]
Cu_3SbSe_4	Tetragonal ($I\bar{4}2m$)	4	109.5	2.90	[72], [121]

7 Conclusions and Future Work

The aim of this work was to identify materials with inherently low lattice thermal conductivity, favorable electronic properties, and inexpensive elemental constituents for use in thermoelectric power generation applications. Materials that met these unique criteria were selected using a novel approach in which complex ternary semiconductors were derived from simple binary semiconductors through successive isoelectronic atomic substitutions. The resulting ternary compounds had a larger number of atoms per primitive unit cell, resulting in low lattice thermal conductivity, yet maintain crystal structures closely related to those of their parent binary compounds and are still semiconductors. Using this approach, several different ternary semiconductors composed primarily of Cu and Se were identified and investigated as potential thermoelectric materials.

The first portion of this work was devoted to finding low-cost alternatives to ternary Ag-based rocksalt-like semiconductors. Compounds such as $AgSbTe_2$ are ternary derivatives of PbTe and have excellent thermoelectric properties, but are too costly for large-scale use. Two Cu-based compounds, $CuBiSe_2$ and Cu_3BiSe_3, were previously reported as having the rocksalt-like structure and were investigated as potential replacements for $AgSbTe_2$. It was found that $CuBiSe_2$ is not a

thermodynamically stable phase and Cu_3BiSe_3 exists but not in the rocksalt-like crystal structure. As such, neither of these compounds was investigated further.

The majority of this work focused on Cu-based ternary compounds derived from the zincblende structure II-VI semiconductors. Three and four-fold ternary derivatives of the II-VI semiconductors were chosen as the most promising families of compounds due to their low lattice thermal conductivities and appropriate band gaps for thermoelectric power generation. Compounds of the form I_2-IV-VI_3 and I_3-V-VI_4 where I = Cu, IV = Ge or Sn, V = Sb, and VI = Se or S were synthesized, characterized, and optimized for thermoelectric applications. From the I_2-IV-VI_3 family of compounds, Cu_2SnSe_3 and Cu_2GeSe_3 were prepared as single-phase samples with crystal structures closely related to that of zincblende. Ga and In were found to be effective p-type dopant species in Cu_2SnSe_3 when substituted for Sn and improved the thermoelectric properties of the compound, but sample-to-sample variations in hole concentration prevented further optimization. Cu_2SnSe_3 forms a complete solid solution with both Cu_2GeSe_3 and Cu_2SnS_3; the lattice thermal conductivity is reduced to a much larger extent in the Cu_2SnSe_3- Cu_2SnS_3 solid solution due to the significant atomic mass and size differences between Se and S. The optimum thermoelectric performance was achieved using 30% S substitution on the Se site and 7.5% In doping on the Sn site, resulting in ZT=0.62 at 760K. Above this temperature the sample softened and was physically deformed in the measurement apparatus. It was found that Cu_2GeSe_3 can accommodate excess Ge up to $Cu_2Ge_2Se_3$, which induces a structural transition from orthorhombic to cubic symmetry near $Cu_2Ge_{1.55}Se_3$. The lattice thermal conductivity decreases appreciably with increasing Ge content, presumably due to phonon-impurity scattering, although controlling the hole concentration in these compounds proved to be problematic and doping studies were largely unsuccessful. From these results it is concluded that the I_2-IV-VI_3 compounds are promising potential thermoelectric materials but a better understanding of how to reproducibly control the hole concentration is needed. Future work in this area should include electronic band structure and defect calculations in order to identify possible self-doping mechanisms in these compounds.

From the I_3-V-VI_4 family of compounds Cu_3SbSe_4 was prepared as a single phase with a crystal structure similar to that of zincblende. A quenching and annealing procedure was developed that produced homogeneous samples with reproducible hole concentration. It was found that both Ge and Sn are effective p-type dopant species when substituted on the Sb site, and optimally doped Cu_3SbSe_4 achieved ZT = 0.72 at 630K. The previously unexplored Cu_3SbSe_4- Cu_3SbS_4 system was investigated over the entire compositional range and found to form a complete solid solution. The lattice thermal conductivity was reduced by 40% at high temperature and reached the estimated minimum value for these compounds, 0.5 W/m*K, at 650K. When optimally doped, the $Cu_3SbSe_{4-x}S_x$ compounds can achieve ZT = 0.89 at 650K, rivaling the thermoelectric performance of state of the art p-type materials. These compounds present a distinct advantage over many high performance p-type materials in that they contain no toxic or overly expensive elements. Future work in this area should include an investigation of the mechanical properties of these compounds as well as fine-tuning the doping level and S concentration to increase ZT.

A detailed analysis of the Cu-Sb-Se system revealed three possible ternary compounds: Cu_3SbSe_4, Cu_3SbSe_3, and $CuSbSe_2$. It was found that these compounds have vastly different lattice thermal conductivities despite their similar compositions and crystal structures. A simple valence assessment revealed Sb to be pentavalent (5+) in Cu_3SbSe_4 and trivalent (3+) in Cu_3SbSe_3, and $CuSbSe_2$, meaning that Sb does not donate its 5s valence electrons to the bonding network in the latter two compounds. The displacement of these lone-pair electrons from the Sb nucleus can be evaluated based on the Se-Sb-Se bond angle, which is known from crystallographic analyses. It was found that when the lone-pair is far removed from the Sb nucleus, which correlates to a large Se-Sb-Se bond angle, the lattice thermal conductivity is lower than when the lone-pair is located near to the Sb nucleus, corresponding to a small Se-Sb-Se bond angle, due to repulsive interactions between the lone-pair and neighboring negatively charged Se ions. This effect is illustrated by the three Cu-Sb-Se compounds, and was generalized to all group VA chalcogenides using literature data. The trend of decreasing lattice thermal conductivity with increasing bond angle holds true

for the group VA chalcogenides, and it was established that the coordination number of the group VA atom plays a role in the rate of decrease. This is the first direct evidence in favor of a relationship between lattice thermal conductivity and lone-pair electrons, and could prove useful in the search for new high performance thermoelectric materials. Numerous opportunities for new research exist in this area, including high energy X-ray studies (such as Mossbauer spectroscopy) of these materials to probe the electron density around the group VA nucleus, experimental investigations of candidate materials that meet bond angle criteria for low thermal conductivity, and calculations of the Gruneisen parameters of these materials, which would provide more insight as to the effect of lone-pair electrons on lattice anharmonicity.

REFERENCES

REFERENCES

[1] G.S. Nolas, J. Sharp, H.J. Goldsmid, *Thermoelectrics Basic Principles and New Materials Developments*, Springer-Verlag Berlin Heidelberg New York (2001), pg. 4.

[2] G.L. Bennett, J.L. Lombardo, R.J. Hemler, G. Silverman, C.W. Whitmore, W.R. Amos, E.W. Johnson, A. Schock, R.W. Zocher, T. K. Keenan, J.C. Hagan, R.W. Englehart, "Mission of daring: the general-purpose heat source radioisotope thermoelectric generator", AIAA 2006-4096, 4th International Energy Conversion Engineering Conference and Exhibit (IECEC), 26-29 June 2006.

[3] "Estimated U.S. Energy Use in 2009: 94.6 Quads" Source: LLNL 2010. Data is based on DOE/EIA-0384(2009). Web address: https://flowcharts.llnl.gov/.

[4] F. Stabler, "Automotive Thermoelectric Generator Design Issues" DOE Thermoelectric Applications Workshop.

[5] D. Kraemer, B. Poudel, H.P. Feng, J. C. Caylor, B. Yu, X. Yan, Y. Ma, X. Wang, D. Wang, A. Muto, K. McEnaney, M. Chiesa, Z. Ren, and G. Chen, "High-performance flat-panel solar thermoelectric generators with high thermal concentration", *Nature Materials*, **10**, 532 (2011).

[6] C.B. Vining, "An inconvenient truth about thermoelectrics", *Nature Materials* **8**, 83 (2009).

[7] E.S. Toberer, A.F. May, G.J. Snyder, "Zintl chemistry for designing high efficiency thermoelectric materials", *Chemistry of Materials* **22**, 624 (2010).

[8] A.F. Ioffe, "Heat transfer in semiconductors", *Canadian Journal of Physics* **34**, 1342 (1956).

[9] A.V. Ioffe, A.F. Ioffe, "Thermal conductivity of semiconductor solid Solutions", *Soviet Physics Solid State* **2**, 719 (1960).

[10] B. Abeles, D.S. Beers, G.D. Cody, J.P. Dismukes, "Thermal conductivity of Ge-Si alloys at high temperatures" *Physical Review* **125**, 44 (1962).

[11] I. Kudman, "Lattice thermal conductivities of semiconductor alloys" *Thermal Conductivity Spec. Publ. No. 302*, National Bureau of Standards, Washington, D. C. 20234, 97 (1968).

[12] I.V. Gasenkova, T.E. Svechnikova, "Structural and transport properties of Sn-doped $Bi_2Te_{3-x}Se_x$ single crystals" *Inorganic Materials* **40**, 570 (2004).

[13] M.A. Afromowitz, "Thermal conductivity of $Ga_{1-x}Al_xAs$ alloys" *Journal of Applied Physics* **44**, 1292 (1973).

[14] G.A. Slack, V.G. Tsoukala, "Some properties of semiconducting $IrSb_3$", *Journal of Applied Physics* **76**, 1665 (1994).

[15] D.J. Braun, V. Jeitschko, "Preparation and structural investigations of antimonides with the $LaFe_4P_{12}$ structure" *Journal of the Less Common Metals* **72**, 147 (1980).

[16] D.T. Morelli, G.P. Meisner, "Low temperature properties of the filled skutterudite $CeFe_4Sb_{12}$", *Journal of Applied Physics* **77**, 3777 (1995).

[17] B.C. Sales, D. Mandrus, R.K. Williams, "Filled skutterudite antimonides: a new class of thermoelectric materials", *Science* **31**, 5266, 1325 (1996).

[18] X. Shi, J.R. Salvador, J. Yang, H. Wang, "Thermoelectric properties of n-type multiple-filled skutterudites" *Journal of Electronic Materials* **38**, 930 (2009).

[19] G.S. Nolas, J.L. Cohn, G.A. Slack, S.B. Schujman, "Semiconducting Ge clathrates: Promising candidates for thermoelectric applications" *Applied Physics Letters* **73**, 178 (1998).

[20] Y. Saiga, K. Suekuni, S.K. Deng, T. Yamamoto, Y. Kono, N. Ohya, T. Takabatake, "Optimization of thermoelectric properties of type-VIII clathrate $Ba_8Ga_16Sn_30$ by carrier tuning", *Journal of Alloys and Compounds* **507**, 1 (2010).

[21] J.H. Roudebush, E.S. Toberer, H. Hope, G.J. Snyder, S.M. Kauziarich, "Crystal structure, characterization and thermoelectric properties of the Type-I clathrate $Ba_{8-y}Sr_yAl_{14}Si_{32}$ ($0.6 \leq y \leq 1.3$), prepared by aluminum flux", *Journal of Solid State Chemistry*, **184**, 1176 (2011).

[22] H.J. Goldsmid, A.W. Penn, "Boundary scattering of phonons in solid solutions", *Physics Letters* **27A**, 523 (1968).

[23] D.M. Rowe, V.S. Shukla, "The effect of phonon-grain boundary scattering on the lattice thermal conductivity and thermoelectric conversion efficiency of heavily doped, fine-grained, hot-pressed silicon germanium alloy", *Journal of Applied Physics* **52**, 7421 (1981).

[24] D.H. Kim, T. Mitani, "Thermoelectric properties of fine-grained Bi_2Te_3 alloys" *Journal of Alloys and Compounds* **399** 14 (2005).

[25] W. Xie, X. Tang, Y. Yan, Q. Zhang, T.M. Tritt, "Unique nanostructures and enhanced thermoelectric performance of melt-spun BiSbTe alloys", *Applied Physics Letters* **94**, 102111 (2009).

[26] L.D. Hicks, M.S. Dresselhaus, "Effect of quantum-well structures on the thermoelectric figure of merit" *Physical Review B* **47**, 12727 (1993).

[27] M.S. Dresselhaus, G. Chen, M.Y. Tang, R. Yang, H. Lee, D. Wang, Z. Ren, J.P. Fleurial, P. Gogna, "New directions for low-dimensional thermoelectric materials", *Advanced Materials* **19**, 1043 (2007).

[28] T.C. Harmon, M.P. Walsh, B.E. Laforge, G.W. Turner, "Nanostructured thermoelectric materials", *Journal of Electronic Materials* **34**, L19 (2005).

[29] C. Zhou, J. Sakamoto, D. Morelli, "Thermoelectric properties of $Co_{0.9}Fe_{0.1}Sb_3$-based skutterudite nanocomposites with $FeSb_2$ nanoinclusions", *Journal of Applied Physics* **109**, 063722 (2011).

[30] E.J. Skoug, C. Zhou, Y. Pei, D.T. Morelli, "High thermoelectric power factor in alloys based on CoSi", *Applied Physics Letters* **94**, 022115 (2009).

[31] E.J. Skoug, C. Zhou, Y. Pei, D.T. Morelli, "High thermoelectric power factor near room temperature in full-heusler alloys", *Journal of Electronic Materials* **38**, 1221 (2009).

[32] C.H.L Goodman, R.W. Douglas, "New semiconducting compounds of diamond type structure", *Physica* **20**, 1107 (1954).

[33] J.H. Wernick, K.E. Benson, "New semiconducting ternary compounds", *Journal of Physics and Chemistry of Solids* **3**, 157 (1957).

[34] V.P. Zhuze, V.M. Sergeeva, E.L. Shtrum, "Semiconducting compounds with the general formula ABX_2" *Soviet Physics - Technical Physics* **3**, 1925 (1958).

[35] T. Hirai, K. Kurata, Y. Takeda "Derivation of new semiconducting compounds by cross substitution for group IV semiconductors, and their semiconducting and thermal properties", *Solid-State Electronics* **10**, 975 (1967).

[36] E.F. Hockings, "The thermal conductivity of silver antimony telluride", *Journal of Physics and Chemistry of Solids* **10**, 341 (1959).

[37] A.V. Petrov, E.L. Shtrum, "Heat conductivity and the chemical bond in ABX_2-type compounds", *Soviet Physics - Solid State* **4**, 1061 (1962).

[38] F.D. Rosi, E.F. Hockings, N.E. Lindenblad "Semiconducting materials for thermoelectric power generation", *RCA Review* **22**, 82 (1961).

[39] R.W. Armstrong, J.W. Faust, W.A. Tillier, "Structural study of the compound $AgSbTe_2$", *Journal of Applied Physics* **31**, 1954 (1960).

[40] V. Jovovic, J.P. Heremans, "Measrements of the energy band gap and valence band structure of $AgSbTe_2$", *Physical Review B* **77**, 245204 (2008).

[41] V. Jovovic, J.P. Heremans, "Doping effects on the thermoelectric properties of $AgSbTe_2$" *Journal of Electronic Materials* **38**, 1504 (2009).

[42] K.F. Hsu, S. Loo, F. Guo, W. Chen, J.S. Dyck, C. Uher, T. Hogan, E.K. Polychroniadis, M.G. Kanatzidis, "Cubic $AgPb_mSbTe_{2+m}$: Bulk thermoelectric materials with high figure of merit", *Science* **303**, 818 (2004).

[43] E. Quarez, K.F. Hsu, R. Pcionek, N. Frangis, E.K. Polychroniadis, M.G. Kanatzidis, "Nanostructuring, compositional fluctuations, and atomic ordering in the thermoelectric materials $AgPb_mSbTe_{2+m}$. The myth of solid solutions.", *Journal of the American Chemical Society* **127**, 9177 (2005).

[44] D.T. Morelli, V. Jovovic, J.P. Heremans, "Intrinsically minimal thermal conductivity in cubic I-V-VI_2 semiconductors", *Physical Review Letters* **101**, 035901 (2008).

[45] G.A. Slack, "The thermal conductivity of nonmetallic crystals", *Solid State Physics* **34**, 1 (1979).

[46] D.P. Spitzer "Lattice thermal conductivity of semiconductors: a chemical bond approach" *Journal of Physics and Chemistry of Solids* **31** 19 (1970).

[47] M. Golovei, "Investigation of Cu(Ag, Tl)-B^V-Se systems" (in Russian), *Izvestiya Vysshikh Uchebnykh Zavedenii Khimiya I Khimicheskaya* **28**, 7 (1985).

[48] J.C. Garcia, G. Brun, B. Liautard, J.C. Tedenac, M. Maurin, "Etude des equilibres de phases dans le systeme Cu_2Se - Bi_2Se_3. Caracterisation des composes intermediaires" (in French), *Materials Research Bulletin* **25** 241 (1990).

[49] S. Karup-Moller, "The Cu-Bi-Se phase system at temperatures between 300 degrees and 750 degrees C", *Neues Jahrbuch fur Mineralogie Monatshefte* **12** 556 (2003).

[50] P.I. Pollak, J.B. Conn, E.J. Sheehan, C.J. Barolay, "Structural investigations in thermoelectric materials", *Quarterly Report No. 1*, Merck Sharp & Dohme Research Laboratories (1962).

[51] *Bi-Cu-Se Phase Diagram (1990 Garcia J.C.)*, ASM Alloy Phase Diagrams Center, P. Villars, editor-in-cheif; H. Okamoto and K. Cenzual, section editors; ASM International, Materials Park, OH (2007). Phase diagram reproduced from [48].

[52] E. Makovicky, I. Sotofte, S. Karup-Moller, "The crystal structure of $Cu_{1.78}Bi_{4.73}Se_8$, an N = 3 pavonite homologue with a Cu-for-Bi substitution", *Zeitschrift fur Kristallographie* **221**, 122 (2006).

[53] N. Frangis, C. Manolikas, and S. Amelinckx, "Vacancy-ordered superstructures in Cu_2Se", *Physica Status Solidi (a)* **126**, 9 (1991).

[54] T. Wada, Y. Hashimoto, S. Nishiwaki, T. Satoh, S. Hayashi, T. Negami, H. Miyake, "High-efficiency CIGS solar cells with modified CIGS surface", *Solar Energy Materials and Solar Cells* **67**, 305 (2001).

[55] S.M. Wasim, "Thermal conductivity of ternary compounds", *Physica Status Solidi (a)* **51**, K35 (1979).

[56] D.T. Morelli and G.A. Slack, in *High Thermal Conductivity Materials*, edited by S. Shinde and J. Goela (Springer, New York, 2005), p. 42-47.

[57] J.O. Sofo, G.D. Mahan, "Optimum band gap of a thermoelectric material", *Physical Review B* **49**, 7 (1994).

[58] L.I. Berger, V.D. Prochukhan, *Ternary Diamond-Like Semiconductors*, Translated from Russian by Albin Tybulewicz, Consultants Bureau, New York (1969).

[59] H. Hahn, W. Klingen, P. Ness, H. Schulze, "Ternary Chalcogenides. XVII. Ternary Chalcogenides of silicon, germanium, and tin", *Naturwissenschaften* **53**, 18 (1966).

[60] N.A. Goryunova, G.K. Averkieva, Y.V. Alekseev, "Quaternary Homogeneous Phases with Zinc Blend Structure based on Cu2GeSe3" *Izv. Moldavsk. Filiala Adad. Nauk SSSR*, **3**, 99 (1960).

[61] W. Scott, "Some properties of Cu2SnSe3, Cu2GeSe3, and other A2BC3 compounds", *Journal of Electronic Materials* **3**, 1 (1974).

[62] L.S. Palatnik Y.F. Komnik, E.K. Belova, L.V. Atroshchenko, "Investigation of the Ternary Semiconductor Compounds Containing Copper and Elements of Groups IV and VI" *Kristallografiya* **6**, 960 (1961).

[63] B.B. Sharma, F.R. Chavada, "Variation of lattice parameter with temperature and thermal expansion of the compound Cu_2SnSe_3", *Physica Status Solidi (a)* **14**, 639 (1972).

[64] G. Marcano, C. Ricon, L.M. de Chalbaud, D.B. Bracho, G. Sanchez Perez, "Crystal growth and structure, electrical and optical properties of the semiconductor Cu_2SnSe_3", *Journal of Applied Physics* **90**, 1847 (2001).

[65] G.E. Delgado, A.J. Mora, G. Marcano, C. Rincon, "Crystal structure refinement of the semiconducting compound Cu_2SnSe_3 from x-ray powder diffraction data", *Materials Research Bulletin* **38**, 1949 (2003).

[66] Materials Science International Team MSIT®, and Lebrun, Nathalie, Perrot, Pierre, Tomashik, Vasyl: Cu-Se-Sn (Copper-Selenium-Tin). Effenberg, G., Ilyenko, S. (ed.). SpringerMaterials - The Landolt-Börnstein Database. DOI: 10.1007/10915981_26.

[67] K. Hirono, M. Kono, "On the electrical and thermal properties of the ternary chalcogenides A_2BX_3, ABX_2, A_3BX_4 (A=Cu, B=Ge,Sn, X=S, Se, Te) I. Thermoelectric Properties at Room Temperature", *Japanese Journal of Applied Physics* **7**, 1 (1968).

[68] T. Irie, "Lattice thermal conductivity of disordered alloys of ternary compound semiconductors Cu_2(Sn, Ge)(Se, S)$_3$ (Ag, Pb, Sb)Te_2, and (Ag, Sn, Sb)Te_2" *Japanese Journal of Applied Physics* **5**, 854 (1966).

[69] E. Parthe, J. Garin, "Zinkblende- und Wurtzitüberstrukturen bei ternären Chalkogeniden der Zusammensetzung 12463" *Monatshefte für Chemie* **102** 1197 (1971).

[70] B.B. Sharma, H. Singh, "Stability of the tetrahedral phase in the Cu-Ge-Se system", *Journal of Solid State Chemistry* **11** 285 (1974).

[71] B.B. Sharma, R. Ayyar, H. Singh, "The cubic phase in the Cu2GeSe3-Ge system", *Physica Status Solidi (a)* **29** K17 (1975).

[72] A. Pfitzner, "Crystal Structure of tricopper tetraselenoantimonate (V) Cu_3SbSe_4", *Zeitschrift für Kristallographie* **209**, 685 (1995).

[73] W. Scott, J.R. Kench, "Phase diagram and properties of Cu_3SbSe_4 and other A_3BC_4 compounds", *Materials Research Bulletin* **8**, 1257 (1973).

[74] H. Nakanishi, S. Endo, T. Irie, "On the electrical and thermal properties of the ternary chalcogenides A_2BX_3, ABX_2, A_3BX_4 (A=Cu, B=Ge,Sn, X=S, Se, Te) II. Electrical and Thermal properties of Cu_3SbSe_4", *Japanese Journal of Applied Physcis* **8**, 4 (1969).

[75] S.N. Aliev, G.G. Gadzhiev, Y.B. Magomedov, "Electrical and thermal conductivity of Cu_3AsSe_4 and Cu_3SbSe_4", *Soviet Physics-Semiconductors* **3**, 11 (1970).

[76] J. Rivet, Investigation of some ternary sulphides, selenides and tellurides of copper with elements of IVb groupe (in French), *Ann. Chim. (Paris)*, **10**, 243 (1965).

[77] B.B Sharma, R. Ayyar, H. Singh, "Stability of the tetrahedral phase in the $A^I{}_2B^{IV}C^{VI}{}_3$ group of compounds", *Physica Status Solidi (a)* **40**, 691 (1977).

[78] G. Marcano, C. Rincon, G. Marin, R. Tovar, G. Delgado, "Crystal growth and characterization of the cubic semiconductor Cu_2SnSe_4" *Journal of Applied Physics* **92**, 1811 (2002).

[79] X. Shi, L. Xi, J. Fan, W. Zhang, L. Chen, "Cu-Se bond network and thermoelectric compounds with complex diamondlike structure" *Chemistry of Materials* **22**, 6029 (2010).

[80] X. Y. Shi, F. Q. Huang, M. L. Liu, L. D. Chen, "Thermoelectric properties of tetrahedrally bonded wide-gap stannite compounds $Cu_2ZnSn_{1-x}In_xSe_4$" *Applied Physics Letters* **94**, 122103 (2009).

[81] M. L. Liu, I. W. Chen, F. Q. Huang, L.D. Chen, "Improved thermoelectric properties of Cu-doped quaternary chalcogenides of $Cu_2CdSnSe_4$", *Advanced Materials* **21**, 3808 (2009).

[82] G.K. Averkieva, A.A. Vaipolin, N.A. Goryunova, "Some ternary compounds of the A_2BC_3 type and solid solutions based on them", *Soviet Research in New Semiconducting Materials*, 26 (1965).

[83] E.J. Skoug, J.D. Cain, D.T. Morelli, "Thermoelectric properties of the Cu_2SnSe_3-Cu_2GeSe_3 solid solution" *Journal of Alloys and Compounds* **506**, 18 (2010).

[84] R. Berman, *Thermal Conduction in Solids* Oxford University Press, 1976, pg. 23.

[85] L.I. Berger, *Semiconductor Materials*, CRC Press, Boca Raton, FL, 1997, pg. 260.

[86] N.W. Ashcroft, N.D. Mermin, *Solid State Physics*, Thomson Learning, Inc. 1976, pg. 457.

[87] G.A. Slack, S. Galginaitis, "Thermal conductivity and phonon scattering by magnetic impurities in CdTe" *Physical Review* **133**, A253 (1964).

[88] P.G. Klemens, "The scattering of low-frequency lattice waves by static imperfections" *Proc. R. Soc.* London, Ser. A 68, 1113 (1955).

[89] J. Callaway, H.C. von Baeyer, "Effect of point imperfections on lattice thermal conductivity" *Physical Review* **120**, 1149 (1960).

[90] D.T. Morelli, J.P. Heremans, G.A. Slack, "Estimation of the isotope effect on the lattice thermal conductivity of group IV and group III-V semiconductors", *Physical Review B* **66**, 195304 (2002).

[91] B. Abeles, "Lattice thermal conductivity of disordered semiconductor alloys at high temperatures" *Physical Review* **131**, 1906 (1963).

[92] J. Yang, G.P. Meisner, L. Chen, "Strain field fluctuation effects on lattice thermal conductivity of ZrNiSn-based thermoelectric compounds" *Applied Physics Letters* **85**, 1140 (2004).

[93] B.D. Cullity and S.R. Stock, *Elements of X-ray Diffraction*, Third Edition, Prentice-Hall, Inc., NJ, 2001, pp. 390-395.

[94] A. Smakula, J. Kalnajs, "Precision determination of lattice constants with a Geiger counter x-ray diffractometer" *Physical Review* **99** 1737 (1955).

[95] Y. Gelbstein, Z. Dashevsky, M.P. Dariel "High performance n-type PbTe-based materials for thermoelectric applications", *Physica B: Condensed Matter* **363**, 196 (2005).

[96] A. Pfitzner, T. Bernert, "The system Cu_3AsS_4-Cu_3SbS_4 and investigations on normal tetrahedral structures", *Zeitschrift für Kristallographie* **219**, 20 (2004).

[97] A. Pfitzner, S. Reiser, "Refinement of the crystal structures of Cu_3PS_4 and Cu_3SbS_4 and a comment on normal tetrahedral structures", *Zeitschrift für Kristallographie* **217**, 51 (2002).

[98] Kh. I. Amirkhanov, G.G. Gadzhiev, Ya. B. Magomedov, *Teplofiz. Vys. Temp.* **16**, 1232 (1978).

[99] G.A. Slack, "New materials and performance limits for thermoelectric cooling", *CRC Handbook of Thermoelectrics*, edited by D.M. Rowe, CRC Press, Boca Raton, FL (1995).

[100] V.I. Fistul', *Heavily Doped Semiconductors*, Plenum Press, New York, 1969, p. 155.

[101] Y. Pei, A. LaLonde, S. Iwanaga, and G.J. Snyder, "High thermoelectric figure of merit in heavy hole dominated PbTe" *Energy & Environmental Science* **4**, 2085 (2011).

[102] X. Tang, H. Li, Q. Zhang, M. Niino, and T. Goto, "Synthesis and thermoelectric properties of double-atom-filled skutterudite compounds $Ca_mCe_nFe_xCo_{4-x}Sb_{12}$" *Journal of Applied Physics* **100**, 123702 (2006).

[103] S.H. Yang, T.J. Zhu, T. Sun, J. He, S.N. Zhang, X.B. Zhao, "Nanostructures in high performance thermoelectric materials $(GeTe)_x(AgSbTe_2)_{100-x}$" *Nanotechnology* **19**, 245707 (2008).

[104] 'Zur Theorie der spezifischen Waerme', Annalen der Physik (Leipzig) 39(4), 789 (1912)

[105] M.C. Roufosse, P.G. Klemens, "Lattice thermal conductivity of minerals at high temperatures", *Journal of Geophysical Research* **79**, 703 (1974).

[106] T.N. Polynova, M.A. Porai-Koshits, "Stereochemistry of trivalent antimony compounds" Translated from *Zhurnal Strukturnoi Khimii* **7**, 146 (1966).

[107] I. Lefebvre, M. Lannoo, G. Allan, A. Ibanez, J. Fourcade, J.C. Jumas, "Electronic properties of antimony chalcogenides", *Physical Review Letters* **59**, 2471 (1987).

[108] J. Oliver-Fourcade, A. Ibanez, J.C. Jumas, M. Maurin, I. Lefebvre, P. Lippens, M. Lannoo, G. Allan, "Chemical bonding and electronic properties in antimony chalcogenides", *Journal of Solid State Chemistry* **87**, 366 (1990).

[109] X. Wang and F. Liebau, "Studies on bond and atomic valences. I. Correlation between bond valence and bond angles in Sb^{III} chalcogen compounds: the influence of lone-electron pairs", *Acta Crystallographica* **52**, 7 (1996).

[110] E.J. Skoug, J.D. Cain, D.T. Morelli, "Structural effects on the lattice thermal conductivity of ternary antimony and bismuth-containing chalcogenide semiconductors", *Applied Physics Letters* **96**, 181905 (2010).

[111] A. Pfitzner, "Cu_3SbSe_3: synthese und kristallstruktur", *Zeitschrift für Anorganische und Allegemeine Chemie* **621** 685 (1995).

[112] J. Zhou, G.Q. Bian, Q.Y. Zhu, Y. Zhang, C.Y. Li, J. Dai, "Solvothermal crystal growth of $CuSbQ_2$ (Q = Se, Se) and the correlation between macroscopic morphology and microscopic structure", *Journal of Solid State Chemistry* **182**, 259 (2009).

[113] A. Kyono, M. Kimata, M. Matsuhisa, Y. Miyashita, K. Okamoto, "Low-temperature crystal structures of stibnite implying orbital overlap of Sb $5s^2$ inert pair electrons", *Physical Chemistry of Minerals* **29**, 254 (2002).

[114] Collaboration: Authors and editors of the volumes III/17E-17F-41C: *Antimony telluride (Sb2Te3) crystal structure, chemical bond, lattice parameters (including data for Bi2Se3, Bi2Te3).* O. Madelung, U. Rössler, M. Schulz (ed.). SpringerMaterials - The Landolt-Börnstein Database.

[115] Y. Takeuchi, T. Ozawa, "The structure of $Cu_4Bi_4S_9$ and its relation to the structures of covellite, CuS and bismuthinite, Bi_2S_3", *Zeitschrift für Kristallographie* **141**, 217 (1975).

[116] V.A. Bazakutsa, M.P. Vasileva, "Thermal conductivity of triple semiconductors of $A_1SbC_2^6$ type as a function of chemical composition and structure", *Journal of Engineering Physics and Thermophysics* **34**, 137 (1978).

[117] V.A. Bazakutsa, M.P. Vasileva, V.N. Ustimenko, L.M. Mokhir, "Lattice thermal conductivity and chemical bond in the hypovalent two-cation semiconductors $A_1BC_2^6$ and $TlB^5C_2^6$", *Journal of Engineering Physics and Thermophysics* **37** 1191 (1979).

[118] A.S. Kanishcheva, V.G. Kuznetsov, V.B. Lazarev, T.G. Tarasova, "Crystal Structure of $RbSbS_2$", *Journal of Structural Chemistry* **18**, 849 (1978).

[119] T.J. McCarthy, S.P. Ngeyi, J.H. Liao, D.C. DeGroot, T. Hogan, C.R. Kannewurf, M.G. Kanatzidis, "Molten salt synthesis and properties of three new solid state ternary bismuth chalcogenides, β-$CsBiS_2$, γ-$CsBiS_2$, and $K_2Bi_8Se_{13}$", *Chemistry of Materials* **5**, 331 (1993).

[120] K.S. Liang, A. Bienenstock, C.W. Bates, "Structural studies of glassy $CuAsSe_2$ and $Cu-As_2Se_3$ alloys", *Physical Review B* **10**, 1528 (1974).

[121] Compounds synthesized and measured for the present work.

[122] J.C. Portheine, W. Nowacki, "Refinement of the crystal structure of emplectite, $CuBiS_2$", *Zeitschrift für Kristallographie* **141**, 387 (1975).

[123] Y. Takeuchi, R. Sadanaga "Structural principles and classification of sulfosalts", *Zeitschrift für Kristallographie* **130** 346 (1969).

[124] A. Orliukas, V. Valiukenas, A. Kybartas Kezionis, V. Vilnius, "Peculiarities of phase transitions in α and β-$AgSbS_2$ single crystals" *Ferroelectrics* **38** 897 (1981).

[125] Z.M. Yang, F. Pertlik, "The thallium sulfarsenites Tl_3AsS_3 and $TlAsS_2$ [thallium(I)-thioarsenates(III)]: structural characterization and syntheses", *Journal of Alloys and Compounds* **216**, 155 (1994).

[126] C.L. Teske, W. Bensch, "$TlBiS_2$", *Acta Crystallographica* **E62**, i163 (2006).

[127] A. Olsen, P. Goodman, H.J. Whitfield, "The structure Tl_3SbS_3, Tl_3SbSe_3, $Tl_3SbS_{3-x}Se_x$, and $Tl_3Sb_yAs_{1-y}Se_3$" *Journal of Solid State Chemistry* **60**, 305 (1985).

[128] D.Y. Chung, K.S. Choi, L. Iordanidis, J.L. Schindler, P.W. Brazis, C.R. Kannewurf, B. Chen, S. Hu, C. Uher, M.G. Kanatzidis, "High thermopower and low thermal conductivity in semiconducting ternary K-Bi-Se compounds. Synthesis and properties of β-$K_2Bi_8Se_{13}$ and $K_{2.5}Bi_{8.5}Se_{14}$ and their Sb analogues", *Chemistry of Materials* **9**, 3060 (1997).

[129] J.H. Kim, D.Y. Chung, D. Bilc, S. Loo, J. Short, S.D. Mahanti, T. Hogan, M.G. Kanatzidis, "Crystal growth, thermoelectric properties, and electronic structure of $AgBi_3S_5$ and $AgSb_xBi_{3-x}S_5$ (x=0.3)", *Chemistry of Materials* **17**, 3606 (2005).

[130] H. Y-P. Hong, J.C. Mikkelsen Jr., "Crystal structure of Tl_3AsSe_3", *Materials Research Bulletin* **9**, 365 (1974).

[131] M.D. Ewbank, P.R. Newman, H. Kuwamoto, "Thermal conductivity and specific heat of the chalcogenide salt: Tl_3AsSe_3", *Journal of Applied Physics* **53**, 6450 (1982).